

Analytic treatment of underdamped axionic blue isocurvature perturbations

Daniel J. H. Chung^{*} and Sai Chaitanya Tadepalli[†]

Department of Physics, University of Wisconsin–Madison, Madison, Wisconsin 53706, USA

 (Received 6 November 2021; accepted 10 May 2022; published 14 June 2022)

Previous computations of strongly blue tilted axionic isocurvature spectra were computed in the parametric region in which the lightest time-dependent mass is smaller than the Hubble expansion rate during inflation, leading to an overdamped time evolution. Here we present the strongly blue tilted axionic isocurvature spectrum in an underdamped time evolution parametric regime. Somewhat surprisingly, there exist parametric regions with a strong resonant spectral behavior that leads to a rich isocurvature spectral shape. We focus on computing this resonant spectrum analytically in a large parametric region amenable to such computations. Because the spectrum is sensitive to nonperturbative classical field dynamics, a wide variety of analytic techniques are used including a time-space effective potential obtained by integrating out high-frequency fluctuations.

DOI: [10.1103/PhysRevD.105.123511](https://doi.org/10.1103/PhysRevD.105.123511)

I. INTRODUCTION

Axions are well motivated from the perspective of being a solution to the strong CP problem [1–4] where the experimental bounds (see e.g., [5]) have pushed the Peccei-Quinn (PQ) symmetry-breaking scale f_{PQ} to large values such that the axions are extremely weakly interacting with the Standard Model (SM). The largeness of f_{PQ} at the same time presents an opportunity for axions to be the dominant component of the cosmological dark matter from the perspective of both its interaction strengths and the cosmological energy density [6–15]. Since axions are important from both particle physics as well as cosmological perspectives, several experiments have been devoted to its search [16–30]. A few reviews on direct detection can be found here [31–36] and one can also refer to recent reports [37,38] for a list of various experimental searches and methods.

In most popular axion scenarios where a SM singlet field $\vec{\phi}$ obtains a large vacuum expectation value (VEV) to fix $\langle |\vec{\phi}| \rangle = f_{\text{PQ}}$, the potential for the singlet has a quartic term, which makes the $|\vec{\phi}|$ fast roll to its minimum during inflation if $f_{\text{PQ}} \gg H$, where H is the expansion rate during inflation. In such cases, inflation driven by a different field than $\vec{\phi}$ completes well after $\langle |\vec{\phi}| \rangle$ settles to the minimum of the potential. In these situations where the axions are spectator fields during inflation, the isocurvature spectrum associated with the axion field is nearly scale invariant. The weakness of the axion interactions with the SM fields allow the axion isocurvature perturbations to survive

thermalization to be observable through cosmological observables such as the cosmic microwave background (CMB) and galaxy surveys. Production of spectator axion isocurvature perturbations, its model dependences, and associated observational constraints have been widely studied [39–67].

The work of [39] has pointed out that if the PQ charged SM singlet $\vec{\phi}$ moves along a flat direction lifted only by masses of $O(H)$ that is typical in supersymmetric embeddings of the SM, then because the amplitude of the isocurvature perturbations is proportional to $1/|\vec{\phi}|$ the isocurvature fluctuations of the spectator axion fields can have a strongly blue tilt. Such situations allow the isocurvature to be negligible on large scales probed by the CMB yet become large on short length scales. Unlike the compensated isocurvature perturbations [68–71], which hide the total matter gravitational effects at linear order, the strongly blue isocurvature perturbations can give large gravitational effects at linear order on short length scales. Also, unlike the phenomena explored in works such as [72] where the $O(H)$ mass field mixing effects with the curvature perturbations lead to observables, here we are exploring situations where the $O(H)$ mass field is stable similar to the ideas of [73] and can be observed gravitationally in standard probes such as CMB and large-scale structure. Besides being important for the completion of QCD axion phenomenology, a discovery of a strongly blue tilted isocurvature spectra will generically indicate the existence of a dynamical degree of freedom during inflation which has a time-dependent mass, quite model independently [74]. The transition region from the strongly blue tilted region to the flat region of the isocurvature spectra within the supersymmetric axion model of [39] was

^{*}danielchung@wisc.edu

[†]stadealli@wisc.edu

investigated by [75]. All of the previous computations of the spectrum focused on the overdamped scenarios in which the mass of $\vec{\phi}$ flat direction is smaller than $3H/2$. Even in the fits to data that were done in [76,77], the parameters were restricted to overdamped scenarios because the spectrum was naively expected to be negligible in the underdamped scenarios.

In this paper, we compute the strongly blue axionic isocurvature spectrum in the underdamped case where the mass of the $\vec{\phi}$ flat direction is larger than $3H/2$, focusing on a parametric region where both the spectral shape is interesting and analytic computation is possible. Somewhat surprisingly, the isocurvature spectrum can exhibit a set of rich spectral resonant shapes with a large enhancement in the amplitude that crucially depends on the underdamped nature of the $\vec{\phi}$ dynamics. Because the spectrum in this resonant parametric region depends on nonperturbative classical dynamics of $\vec{\phi}$, a set of nonperturbative mathematical methods is employed to obtain the analytic spectrum. These include piecewise polynomial solutions to differential equations in a couple of time regions and piecewise effective time-space potential (ETSP) modeling after integrating out fast oscillations. This allowed us to compute a transfer matrix solution to the isocurvature mode equations. Because of this lack of perturbativity, the derivation of analytic expressions as well as the results are quite lengthy.¹ Readers interested in just the main results can refer to Eq. (222), where the quantity that is most cumbersome to evaluate is T_c , as explained there.

Intuitively, the isocurvature spectral range that we can give our analytic results is for the wave vector k range where the heavy modes can be decoupled in the axionic model of our interest with multiple degrees of freedom. For the interesting oscillatory part of the spectrum arising from a resonance of background field dynamics, we focus on the parametric region where the velocity of the $\vec{\phi}$ flat direction field is below a particular critical amount to avoid heavy-mode mixing and the background field dynamics becoming chaotic. Due to the already extreme length of the present paper, we defer the discussion of chaotic dynamics and numerical fitting functions that may be useful for data applications to a separate paper. The intuition behind why there is an interesting resonance in the underdamped scenarios while such resonances do not occur in overdamped scenarios is because the overdamped scenarios have field dynamics characterized by exponentials of the form $\exp(-\sqrt{9/4 - c_+}T)$ (where T is a dimensionless time parameter obtained by scaling proper time t with expansion rate H and c_+ is a mass squared parameter for the $\vec{\phi}$ flat direction during the initial period), which turns into

resonant oscillation producing $\exp(-i\sqrt{c_+ - 9/4}T) \ni \cos(\sqrt{c_+ - 9/4}T)$ for the underdamped case. This \cos factor which has a zero will allow the field to reach a dynamically interesting small field region, while the kinetic energy is enhanced by an expansion parameter $(f_{\text{PQ}}/H)^2 \gg 1$, which translates to a factor of at least an $O(10)$ large enhancement in the spectral amplitude over a range of k values when compared to the overdamped scenario. Additionally, the resonance condition has the initial condition-dependent coincidence requirement of interaction induced mixing between two dynamical degrees of freedom being efficient, as will be explained.

Although several of our plots are given with reference to an axion dark matter abundance fraction parameter ω_a^2 where the axion dark matter is fiducially assumed to be a QCD axion, it is written to divide out the effects of the QCD phase transition. Hence, all of our results can easily be used with the axion field interpreted as a general axionlike particle.

The order of presentation will be as follows. After a brief review of the underlying axion model in Sec. II, we explain in Sec. III the decoupling of the heavy modes that can be viewed as the main characterization of the analytic formula presented in this work. Section IV explains one of the technically difficult parts of this work, analytically computing the time T_c when the resonant transition occurs. Section V presents the parametrization of the ETSP that results from integrating out the fast oscillations of the classical background fields (which still exists after decoupling heavy quantum modes). Section VI maps the parameters of the previous section to the underlying axion model parameter space spanned by the dimensionless Lagrangian parameters $\{c_+, c_-, F\}$ and explains the derivation of the isocurvature spectrum without making assumptions about how many large dips there are in the ETSP. Section VII presents a closed form analytic expressions for the isocurvature power spectrum in a certain restricted region of the underlying model space supporting a single large dip in the ETSP. Section VIII explains how the isocurvature spectrum changes as the axion model parameters $\{c_+, c_-, F\}$ are varied. Section IX summarizes this work. An extensive set of appendix sections contain some of the details omitted in the main text.

Appendix A contains an alternative method of computing a critical time T_c required for the isocurvature computations. It serves as an independent check of the computation of T_c presented in Sec. IV. Appendix B describes how the less striking nonresonant situations can be computed within this paper's framework. Appendix C describes a method from [78] of integrating out the fast oscillations to obtain an effective differential equation containing smaller frequencies. Appendix D discusses the dynamics of a composite field object that will be useful in integrating out fast oscillations in the axion model of interest in this paper. Appendix E applies the results of Appendixes C and D to

¹A *Mathematica* package to evaluate the spectrum using the analytic methods is given in <https://pages.physics.wisc.edu/~stadepalli/Blue-Axion-IsoCurvSpec-Underdamped.nb>.

integrate out the fast oscillations in the axion model. Appendix F describes the crucial dynamics associated with the lightest eigenvector rotation that will be helpful in constructing the ETSP of Sec. V as well as the maps to the $\{c_+, c_-, F\}$ space in Sec. VI. Appendix G describes the time dependence of the lightest mass eigenvalue which will be useful in constructing the ETSP as well as the parametric map in Sec. VI. Appendix H describes the form of the ETSP parametrization used in Sec. V. Appendix I discusses the slowly varying part of the lightest mass squared eigenvalue function that governs the physics of one of the parameters of Sec. V. Appendix J explains the details of the effects coming from the heavy modes considered in Sec. III.

II. A BRIEF REVIEW OF BLUE AXIONIC ISOCURVATURE PERTURBATIONS

In [39], a supersymmetric axion model is studied with the following well-known renormalizable superpotential:

$$W = h(\Phi_+\Phi_- - F_a^2)\Phi_0, \quad (1)$$

where the subscripts on Φ indicate $U(1)_{\text{PQ}}$ global PQ charges. Note that this is also the most general renormalizable superpotential transforming under a $U(1)_R$ as

$$\Phi_0 \rightarrow e^{ir}\Phi_0, \quad (2)$$

$$\Phi_+\Phi_- \rightarrow \Phi_+\Phi_-, \quad (3)$$

$$W \rightarrow e^{ir}W. \quad (4)$$

The F-term potential is

$$V_F = h^2|\Phi_+\Phi_- - F_a^2|^2 + h^2(|\Phi_+|^2 + |\Phi_-|^2)|\Phi_0|^2. \quad (5)$$

A special property of this class of potentials is the existence of flat directions: i.e., in this particular model, it is

$$\Phi_+\Phi_- = F_a^2, \quad \Phi_0 = 0. \quad (6)$$

The existence of this flat direction is important because this is the reason why the effective PQ parameters will be rolling with a mass of order H during inflation (instead of being much heavier and having already settled down), taking advantage of the inflationary η -problem: i.e., the Kaehler potential induced scalar potential is

$$V_K = c_+H^2|\Phi_+|^2 + c_-H^2|\Phi_-|^2 + c_0H^2|\Phi_0|^2, \quad (7)$$

where $c_{+,-,0}$ are positive $O(1)$ constants. The parameter c_+ dominantly controls the blue spectral index. This setup implicitly assumes that the inflaton sector can be arranged to have $H \ll F_a$ such that the flat directions are only lifted by the quadratic terms at the renormalizable level.

Looking along the flat direction of Eq. (6), we set $\Phi_0 = 0$. The resulting relevant effective potential during inflation is

$$V \approx h^2|\Phi_+\Phi_- - F_a^2|^2 + c_+H^2|\Phi_+|^2 + c_-H^2|\Phi_-|^2. \quad (8)$$

During inflation, the minimum of V lies at

$$|\Phi_{\pm}^{\text{min}}| = \sqrt{\frac{\sqrt{c_{\mp}}}{\sqrt{c_{\pm}}}F_a^2 - \frac{c_{\mp}}{h^2}H^2} \quad (9)$$

$$\approx \left(\frac{c_{\mp}}{c_{\pm}}\right)^{1/4} F_a. \quad (10)$$

The key initial condition is that Φ_{\pm} starts out away from the minimum with a magnitude much larger than $O(F_a)$ and rolls toward the minimum during inflation. This implies the $U(1)_{\text{PQ}}$ symmetry is broken during inflation. Hence, there will be a linear combination of the phases of Φ_{\pm} which will be the Nambu-Goldstone boson associated with the broken $U(1)_{\text{PQ}}$. In particular, with the parametrization

$$\Phi_{\pm} \equiv \frac{\varphi_{\pm}}{\sqrt{2}} \exp\left(i\frac{a_{\pm}}{\sqrt{2}\varphi_{\pm}}\right), \quad (11)$$

where φ_{\pm} and a_{\pm} are real, the axion is

$$a = \frac{\varphi_+}{\sqrt{\varphi_+^2 + \varphi_-^2}}a_+ - \frac{\varphi_-}{\sqrt{\varphi_+^2 + \varphi_-^2}}a_-, \quad (12)$$

while the heavier combination

$$b = \frac{\varphi_-}{\sqrt{\varphi_+^2 + \varphi_-^2}}a_+ + \frac{\varphi_+}{\sqrt{\varphi_+^2 + \varphi_-^2}}a_- \quad (13)$$

is governed by the potential

$$V_b = -h^2F_a^2\varphi_+\varphi_- \cos\left(\frac{\sqrt{\varphi_+^2 + \varphi_-^2}}{\varphi_+\varphi_-}b\right). \quad (14)$$

Since the b field is heavy [i.e., $(\varphi_+^2 + \varphi_-^2)F_a^2/(\varphi_+\varphi_-) \gg H^2$], it is not dynamically important. Hence, one can gain some intuition for how the axion composition time evolves by setting $b = 0$. When φ_+ is large, the axion is dominantly a_+ and later when φ_+ becomes comparable to φ_- , the axion is a mixture of a_- and a_+ .

According to model [39], the background equations are as follows:

$$\ddot{\Phi}_+(t) + 3H\dot{\Phi}_+(t) + c_+H^2\Phi_+ + h^2(\Phi_+\Phi_- - F_a^2)\Phi_- = 0, \quad (15)$$

$$\ddot{\Phi}_-(t) + 3H\dot{\Phi}_-(t) + c_-H^2\Phi_- + h^2(\Phi_+\Phi_- - F_a^2)\Phi_+ = 0, \quad (16)$$

where Φ_{\pm} has been phase rotated to be real (which is referred to as $\tilde{\Phi}$ in [75]).

The background system can be rescaled as follows:

$$\ddot{\phi}_+(T) + 3\dot{\phi}_+(T) + c_+\phi_+ + \xi(\phi_+, \phi_-)\phi_- = 0, \quad (17)$$

$$\ddot{\phi}_-(T) + 3\dot{\phi}_-(T) + c_-\phi_- + \xi(\phi_+, \phi_-)\phi_+ = 0, \quad (18)$$

where

$$\phi_{\pm} \equiv \Phi_{\pm} \frac{h}{H}, \quad (19)$$

$$F = hF_a/H, \quad (20)$$

$$\xi(\phi_+, \phi_-) \equiv \phi_+\phi_- - F^2, \quad (21)$$

and

$$T \equiv tH. \quad (22)$$

The mode equations can be written in these coordinates as [75]

$$(\partial_T^2 + 3\partial_T)I + \left(\frac{Ka(0)}{a(T)}\right)^2 I + \tilde{M}^2 I = 0, \quad (23)$$

where

$$K \equiv \frac{k}{a(0)H}, \quad (24)$$

$$a(T) = a(0) \exp(T), \quad (25)$$

where $I = (I_+, I_-)$ and the mass matrix can be rewritten as

$$\tilde{M}^2(T) \equiv \begin{pmatrix} c_+ & F^2 \\ F^2 & c_- \end{pmatrix} + \begin{pmatrix} \phi_-^2(T) & 0 \\ 0 & \phi_+^2(T) \end{pmatrix}. \quad (26)$$

Note that we are neglecting the slow roll effects since the ε in models where this scenario is of greatest interest is negligibly small during most of inflation. Note also that as explained in [79], Eq. (23) represents the nonsourced part of the isocurvature modes: i.e., the isocurvature modes. The full $\delta\Phi_{\pm}(x)$ field contains gravitational infall inhomogeneities sourced by the adiabatic inflaton inhomogeneities.

The expression for the isocurvature can be written as

$$\Delta_S^2(t, \vec{k}) \approx 4\omega_a^2 \frac{k^3}{2\pi^2} I^\dagger \begin{pmatrix} r_+^2 & 0 \\ 0 & r_-^2 \end{pmatrix} I, \quad (27)$$

$$r_{\pm} \equiv \sqrt{2} \sqrt{\frac{\phi_{\pm}^2(t)}{(\phi_+^2(t) + \phi_-^2(t))^2 \theta_+^2(t_i)}}, \quad (28)$$

$$\omega_a \equiv \frac{\Omega_a}{\Omega_{\text{cdm}}} \quad (29)$$

$$= W_a \theta_+^2(t_i) \left(\frac{\sqrt{2}(\tilde{\Phi}_+^2(t_f) + \tilde{\Phi}_-^2(t_f))^{1/2}}{10^{12} \text{ GeV}} \right)^{n_{\text{PT}}}, \quad (30)$$

where $W_a \approx 1.5$ and $n_{\text{PT}} \approx 1.19$ [see Eq. (14) in [6]] and t_f is the time just before the QCD phase transition.²

The background field equations (18) control the behavior of isocurvature modes of Eq. (23). Hence, to understand the isocurvature modes, we need to understand the solution space of Eq. (18) in addition to solving Eq. (23). In the parametric region of $c_+ < 9/4$, the background solutions only have a single bump deviation from the time behavior of the lightest mass squared eigenvalue rising with a constant log slope connecting to a plateau region in T space.

ϕ_+ starts from a near Planckian value (but restricted to sub-Planckian to have a good chance of the effective field theory being valid) and moves toward F in the approximate solution

$$\phi_+(T) = \phi_+(0) e^{-3T/2} \left[\cos(\omega T) + \frac{\varepsilon_0 + 3/2}{\omega} \sin(\omega T) \right], \quad (31)$$

where we have labeled the initial time as $T = 0$ and

$$\omega \equiv \sqrt{c_+ - 9/4}, \quad (32)$$

$$\varepsilon_0 \equiv \frac{\dot{\phi}_+(0)}{\phi_+(0)}, \quad (33)$$

while ϕ_- stays near F^2/ϕ_+ , which is the approximate minimum of the potential. Hence, during the initial time period, the background fields ϕ_{\pm} (whose nonzero VEV breaks PQ symmetry) reduce to a single radial degree of freedom. The potentially interesting and nontrivial aspect of this background system's time evolution occurs in two cases: (a) when $\phi_+(T)$ reaches $O(F)$ during the time when $\phi_- \ll F$; (b) T_c when the energy transfer from ϕ_- to ϕ_+ becomes significant (this will be quantified in Sec. IV C). Both of these time periods are dynamically potentially interesting because the mass matrix undergoes transitions such that the mass eigenvalues and the eigenvectors have time variations that are nonadiabatic (change fast compared to timescale of H^{-1}). As we will explain, in most cases, only event (b) leaves significant imprints on the isocurvature spectrum $\Delta_S^2(k)$.

III. DECOUPLING

The dimensionality of the mass matrix indicates that there are two different mass modes. The key de Sitter physics is that at late times, the massive eigenmodes decay

²The fields Φ_{\pm} have settled down long before this.

away while the lighter mode is important. This means that we do not care about the full equations but only the projected equation onto the lightest eigenvector. Let

$$I = \sum_{n=1}^2 y_n(k, T) e_n(T), \quad (34)$$

where $e_n(T)$ are real normalized eigenvectors of \tilde{M}^2 with the $n = 1$ modes being the lighter eigenvalue mode.³ We will call this the instantaneous normalized eigenvector basis. The mode equation (23) becomes

$$\mathcal{O}_1 y_1 = S_{12} y_2, \quad (36)$$

$$\mathcal{O}_2 y_2 = S_{21} y_1, \quad (37)$$

$$\mathcal{O}_n \equiv (\partial_T^2 + 3\partial_T) + \left[-\partial_T e_n \cdot \partial_T e_n + \frac{k^2}{(a(T)H)^2} + m_n^2(T) \right], \quad (38)$$

$$S_{ns}(T) = -e_n \cdot \partial_T^2 e_s - 3\partial_T e_s \cdot e_n - 2e_n \cdot \partial_T e_s \partial_T, \quad (39)$$

where $m_n^2(T)$ are the time-dependent eigenvalues of \tilde{M}^2 . One can solve Eq. (37) formally using the Green's function satisfying

$$\mathcal{O}_n G_n(T, T') = \delta(T - T'). \quad (40)$$

This gives

$$y_2(T) = y_2^h(T) + \int dT' G_2(T, T') S_{21} y_1(T'), \quad (41)$$

where y_2^h is the solution to $\mathcal{O}_2 y_2^h = 0$. Putting this into Eq. (36) gives

$$\mathcal{O}_1 y_1 = S_{12} y_2^h(T) + S_{12} \int dT' G_2(T, T') S_{21}(T') y_1(T'). \quad (42)$$

This is the integro-differential equation that needs to be solved with Bunch-Davies (BD) boundary conditions to compute the isocurvature perturbations.

There are two independent solutions to Eq. (42), both of which are excited to some extent by the quantization with BD boundary conditions. However, the heavy mode is not excited appreciably for the BD boundary conditions, as has

³For example, when $\phi_{\pm}(T)$ have reached the values corresponding to Eq. (9), the lightest eigenvector is

$$e_1 = \frac{(-\sqrt{c_-}, \sqrt{c_+})}{\sqrt{c_- + c_+}}. \quad (35)$$

been checked explicitly. Hence, we focus on the mode with the boundary condition with an initial magnitude of $y_2(T_i) \ll y_1(T_i)$, which means

$$y_2^h(T) = 0. \quad (43)$$

In this case, we see that the right-hand side (rhs) of Eq. (42) can be neglected for the evolution of y_1 as long as

$$\left| \frac{(e_2 \cdot \partial_T^2 e_1)(e_1 \cdot \partial_T^2 e_2)}{m_2^2(m_1^2 + H^2)} \right| \ll 1. \quad (44)$$

Before the two fields transition at T_c when the mass eigenvalues change as a function of time nonadiabatically,⁴ we can estimate $m_2^2 \sim h^2 \phi_{\pm}^2$ and

$$(e_2 \cdot \partial_T^2 e_1)(e_1 \cdot \partial_T^2 e_2) \sim [c_+ F_a^2 H^2 / \phi_{\pm}^2]^2, \quad (45)$$

which means that Eq. (44) is satisfied and y_2 can be neglected. On the other hand, at $T = T_c$, the rhs of Eq. (42) may be important since at that time there is only one scale of F in the system. During this transition time, the time width of the transition is fixed by

$$\Delta T_c \sim \frac{1}{F}. \quad (46)$$

The heavy mixing effect is then quantified in the vicinity of T_c in terms of a new parameter χ_{HM} defined in Appendix J as

$$\chi_{\text{HM}}(l_1^2, l_2^2) \approx \frac{1}{l_2^2 - l_1^2} \left(1 + 2\sqrt{-l_1^2} + \frac{8/3}{\sqrt{-l_1^2}} (-1 + e^{-\sqrt{-l_1^2}} \cos[l_2]) \right), \quad (47)$$

where $l_i^2 = (m_i^2 - \dot{e}_i^2) / \dot{e}_i^2$ and HM stands for heavy mixing. One can then show that as long as (refer to Appendix J)

$$\max(\chi_{\text{HM}}) \lesssim O(r_a), \quad (48)$$

the effect of heavy-mode mixing and the associated rhs of Eq. (42) can be neglected. Close to transition, as \dot{e}_i^2 tends to $O(F^2)$, m_1^2 becomes negative due to nonperturbative effects of $O(F^2)$, while the heavier mass eigenvalue $m_2^2 \sim O(\sqrt{c_+}/c_- F^2)$. The details of the physics and the derivation are discussed in Appendix J. Therefore, we shall work with only those cases that satisfy the condition in Eq. (48). Later we will express these cases more explicitly in terms of the Lagrangian parameters.

⁴The transition is defined in Sec. IV B.

IV. BEHAVIOR OF ϕ_{\pm} NEAR THE FIRST CROSSING OF ϕ_{\pm}

For analytically solvable cases, the details of $\phi_{\pm}(T)$ near the time when

$$\phi_+(T_1) = \phi_-(T_1) \quad (49)$$

for the first time will be important. Hence, in this section, we provide an analytic approximation of this time behavior.

A. Perturbative solution

For $T \ll T_1$, the system can be solved by making the following expansion:

$$\phi_+(T) = \frac{1}{\lambda} \phi_+^{(0)} + O(\lambda^0) + O(\lambda^1) + O(\lambda^2) + \lambda^3 \phi_+^{(1)}, \quad (50)$$

$$\phi_-(T) = \lambda \phi_-^{(0)} + O(\lambda^2) + \lambda^3 \phi_-^{(1)} + O(\lambda^4) + \lambda^5 \phi_-^{(2)}, \quad (51)$$

where the near Planck scale initial conditions for $\phi_+^{(0)}$ gives rise to the prominence of $\phi_+^{(0)}$ justifying λ^{-1} , the near flat direction solution that we seek fixes the λ power for $\phi_-^{(0)}$, and the rest of the λ powers are simply increasing powers where we omit some of them [such as $O(\lambda^0)$ in $\phi_+(T)$ expansion] because they will not contribute (as one can check by introducing them). In other words, one can consider the expansion in λ defined here to be that of smallness of

$$\lambda \leftrightarrow O\left(\sqrt{\frac{\phi_-}{\phi_+}}\right), \quad (52)$$

which is valid over a finite time interval before T_1 .

Putting Eqs. (50) and (51) into Eqs. (17) and (18) and collecting powers of λ , we find the following:

$$\lambda^{-1}: \partial_T^2 \phi_+^{(0)} + 3\partial_T \phi_+^{(0)} + c_+ \phi_+^{(0)} = 0, \quad \phi_+^{(0)} \phi_-^{(0)} - F^2 = 0, \quad (53)$$

$$\lambda^1: \partial_T^2 \phi_-^{(0)} + 3\partial_T \phi_-^{(0)} + (\phi_+^{(0)})^2 \phi_-^{(1)} + c_- \phi_-^{(0)} = 0, \quad (54)$$

$$\lambda^3: \partial_T^2 \phi_+^{(1)} + 3\partial_T \phi_+^{(1)} + c_+ \phi_+^{(1)} + F^2 \phi_-^{(1)} = 0, \quad (55)$$

$$: \partial_T^2 \phi_-^{(1)} + 3\partial_T \phi_-^{(1)} + F^2 \phi_+^{(1)} + \phi_-^{(0)} \phi_+^{(0)2} + c_- \phi_-^{(1)} = 0. \quad (56)$$

The λ^{-1} order has a simple solution ϕ_+ identical to Eq. (31), which can be rewritten as

$$\phi_+(T) \approx \phi_+^{(0)}(T) = \phi_+(0) e^{-\frac{3}{2}T} \sec(\varphi) \cos(\omega T - \varphi), \quad (57)$$

where

$$\tan \varphi \equiv \frac{3/2 + \varepsilon_0}{\omega}. \quad (58)$$

The matching order $\phi_-(T)$ solution is

$$\phi_-(T) \approx \phi_-^{(0)} = \frac{F^2}{\phi_+^{(0)}}. \quad (59)$$

Note that when ϕ_+ initially does not have much kinetic energy (i.e., $\varepsilon_0 \ll 1$), φ takes on values that monotonically decrease from $\pi/2$ to order unity as c_+ increases from 9/4 to 10. The λ^1 order also has a simple, local solution:

$$\phi_-^{(1)} = -\frac{1}{\phi_+^{(0)2}} [\partial_T^2 \phi_-^{(0)} + 3\partial_T \phi_-^{(0)} + c_- \phi_-^{(0)}]. \quad (60)$$

The λ^3 order has a nonlocal solution:

$$[\partial_T^2 \phi_+^{(1)} + 3\partial_T \phi_+^{(1)} + c_+] G_+(T, T') = \delta(T - T'), \quad (61)$$

$$\phi_+^{(1)} = -F^2 \int dT' G_+(T, T') \phi_-^{(1)}(T'), \quad (62)$$

$$\phi_-^{(2)} = \frac{-1}{\phi_+^{(0)2}} [\partial_T^2 \phi_-^{(1)} + 3\partial_T \phi_-^{(1)} + F^2 \phi_+^{(1)} + c_- \phi_-^{(1)}]. \quad (63)$$

Nonetheless, this perturbative expansion by design breaks down near T_1 since the ϕ_-/ϕ_+ hierarchy represented by λ is lost.

Interestingly enough, the correction to

$$\phi_+ \approx \frac{1}{\lambda} \phi_+^{(0)} \quad (64)$$

is $O(\lambda^3)$, which means that the ratio of the next to leading order to the leading order is $O(\lambda^4)$. In contrast, the next to leading order to leading order ratio for ϕ_- is $O(\lambda^2)$. To understand this, note that unlike in the equation of motion for ϕ_- , $\phi_+^{(0)}$ is the *exact* solution to Eq. (17) if $\phi_- = \phi_-^{(0)}$. In contrast, $\phi_-^{(0)}$ is not the exact solution to Eq. (18) with $\phi_+ = \phi_+^{(0)}$. This means that even though the perturbative expansions of Eqs. (50) and (51) for both ϕ_{\pm} break down at T_1 , the approximation for ϕ_- breaks down faster in the region

$$\sqrt{\frac{\phi_-}{\phi_+}} \approx \frac{1}{2}, \quad (65)$$

corresponding to an error of the leading order approximation in this region being

$$\frac{\Delta \phi_+}{\phi_+^{(0)}} \sim O\left(\frac{1}{16}\right), \quad \frac{\Delta \phi_-}{\phi_-^{(0)}} \sim O\left(\frac{1}{4}\right). \quad (66)$$

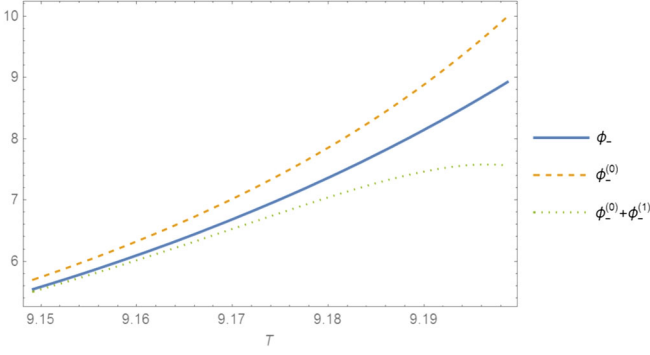


FIG. 1. Numerical background solution compared to the perturbative solution near $T_1 = 9.248$ and $\{c_+ = 2.35, c_- = 0.5, F = 20.2, \varepsilon_0 = 0, \phi_+(0) = 3.32 \times 10^8\}$. For $T \lesssim T_1 - 1/F$, the perturbative solution corrected by $\phi_-^{(1)}$ does much better than the leading order solution $\phi_-^{(0)}$ for $T \lesssim 9.18$. The increasing deviation at T_1 is expected as explained in the text.

As a preliminary check on the perturbative ϕ_{\pm} solution, we can compare the numerical solution to the perturbative solution for ϕ_- for the case of $\{c_+ = 2.35, c_- = 0.5, F = 20.2, \varepsilon_0 = 0, \phi_+(0) = 3.32 \times 10^8\}$ as shown in Fig. 1. The improvement from $\phi_-^{(1)}$ is manifest before the expected breakdown of small $\lambda = O(\sqrt{\phi_-/\phi_+})$ expansion at T_1 defined by Eq. (49).

B. Beyond perturbation theory

Because the background solutions are sensitive to the details of $\phi_-(T_1)$ and the perturbation theory breaks down when $\phi_+(T_1) = \phi_-(T_1)$ [see Eq. (52)], we need a method to solve for the background fields more accurately at T_1 . As we will justify later, because most interesting isocurvature spectral behavior comes from the models in which $\phi_+(T_1)$ is near a zero crossing [i.e., $\phi_+^{(0)}(T_1 + O(1/F)) = 0$], this section will mainly focus on such cases. We will mainly use the method of interpolation using a cubic order polynomial between the time when the perturbation in λ starts to break down and T_1 . We will also check this method in Appendix A using a Taylor expansion approach.

The interpolation polynomial is parametrized as

$$\phi_+(T) = p_0 + p_1(T - T_s) + p_2(T - T_s)^2 + p_3(T - T_s)^3, \quad (67)$$

$$\phi_-(T) = q_0 + q_1(T - T_s) + q_2(T - T_s)^2 + q_3(T - T_s)^3, \quad (68)$$

where we choose T_s to be the time when $\phi_-(T)$ begins to deviate significantly (to be defined) from $\phi_-^{(0)}(T)$. We will then choose the interpolation point T_I taken to be the midpoint between T_s and T_1 based on the idea that such a

choice approximately minimizes set of competing errors.⁵ The coefficients $\{p_n, q_m\}$ will be constrained at T_I through the original differential equations.

In choosing the time T_s to be where the perturbative solution starts to break down, we expect the deviation to come from the neglect of the $\ddot{\phi}_-^{(0)}$ in the zeroth order perturbative solution. Hence, we set T_s to be the time when

$$\ddot{\phi}_-^{(0)} \sim \left(\frac{1}{n}\right) \phi_+^{(0)2} \phi_-^{(0)}, \quad (69)$$

where n parametrizes the $(1/n)$ accuracy we want to achieve in the approximation. For concreteness, we will take $n = 10$ in the analysis below. To solve this equation analytically in a closed form, it is useful to obtain a polynomial form. Hence we expand $\phi_+^{(0)}(T)$ about $\phi_+^{(0)}(T_z)$, where

$$\phi_+^{(0)}(T_z) = 0 \quad (70)$$

or equivalently

$$T_z = \frac{1}{\omega} \left(\frac{\pi}{2} + \varphi \right), \quad (71)$$

where φ is defined by Eq. (58) and assume that $\phi_+^{(0)}(T)$ near T_s is well described by a quadratic expansion of $\phi_+^{(0)}(T)$ about T_z . We will justify this through self-consistency after the analysis.

To simplify the parametric dependence, define a new dimensionless parameter α describing the slope of the zero crossing:

$$\alpha \equiv \frac{|\partial_T \phi_+^{(0)}(T_z)|}{F^2} \quad (72)$$

$$= \omega \frac{\phi_+(0)}{F^2} \sec \varphi e^{-3/2 T_z}. \quad (73)$$

In terms of initial conditions $\phi_+(0)$ and ε_0 , the α parameter can be expressed as

$$\alpha = \frac{\phi_+(0)}{F^2} \sqrt{\omega^2 + (3/2 + \varepsilon_0)^2} e^{-3/2 \left[\frac{1}{\omega} \left(\frac{\pi}{2} + \arctan \frac{3/2 + \varepsilon_0}{\omega} \right) \right]}. \quad (74)$$

Putting Eqs. (57) and (59) into Eq. (69), we obtain

$$T_s = T_z - \frac{(2n)^{\frac{1}{4}}}{\sqrt{\alpha} F} + O\left(\frac{27n}{16\alpha^2 F^4}\right), \quad (75)$$

⁵Since this midpoint choice is an ansatz, we will actually choose the midpoint between T_s and T_z where T_z defined below is close to T_1 .

where the above expansion is valid for $F \gg 1$. We now choose the interpolation point T_I to be the midpoint

$$T_I = \frac{T_s + T_z}{2}, \quad (76)$$

which in most cases will be a point that lies in the interval $[T_s, T_1]$.⁶

We then obtain eight equations to solve for the eight coefficients of Eqs. (67) and (68) using the background differential equations (17) and (18), and the values and the derivatives of the perturbative solutions [Eqs. (57) and (59)]. Solving for these coefficients, we obtain

$$p_3 \approx \frac{(6 + 9\varepsilon + c_- \varepsilon^2 + (\phi_{+(2)}(T_I))^2 \varepsilon^2)(3p_1 + p_2(2 + 6\varepsilon) + \phi_{-(2)}(T_I)\xi_{(2)}(T_I) + c_+ \phi_{+(2)}(T_I))}{\varepsilon D}, \quad (83)$$

$$\frac{(-F^2 + 2\phi_{+(2)}(T_I)\phi_{-(2)}(T_I))(3q_1 + q_2(2 + 6\varepsilon) + \phi_{+(2)}(T_I)\xi_{(2)}(T_I) + c_- \phi_{-(2)}(T_I))}{D/\varepsilon}, \quad (84)$$

$$q_3 \approx p_3(+ \leftrightarrow -, p \leftrightarrow q), \quad (85)$$

where

$$\xi_{(2)} = \xi(\phi_{+(2)}, \phi_{-(2)}), \quad (86)$$

$$D = \varepsilon^4(-F^2 + 2\phi_{+(2)}(T_I)\phi_{-(2)}(T_I))^2 - (6 + 9\varepsilon + c_- \varepsilon^2 + (\phi_{+(2)}(T_I))^2 \varepsilon^2) \times (6 + 9\varepsilon + c_+ \varepsilon^2 + (\phi_{-(2)}(T_I))^2 \varepsilon^2), \quad (87)$$

$$\varepsilon \equiv T_I - T_s, \quad (88)$$

and $\phi_{\pm(2)}$ are defined by Eqs. (67) and (68) with the cubic terms dropped: e.g., $\phi_{+(2)}(T) \equiv p_0 + p_1(T - T_s) + p_2(T - T_s)^2$. Note that since we are using the perturbative solutions $\phi_{\pm}^{(0)}$ [i.e., Eqs. (57) and (59)] for Eqs. (77)–(80), we cannot make n too small (otherwise, the perturbative solutions will be unjustified). To address this and as a general check, we also solve the background system using a Taylor expansion method in Appendix A. We find reasonable agreement with the current method if we take $n \approx 10$.

Now that the background solution is approximately fixed, we can use Eqs. (67) and (68) to solve for the crossing time T_1 and the field value there: i.e., solve for $\phi_+(T_1) = \phi_-(T_1)$. A plot of $\phi_+(T_1)/F$ is given in Fig. 2, showing that for $\alpha \lesssim 1$, the crossing occurs when $\phi_+(T_1) \approx F$. In terms of α and F , we obtain the following

⁶In situations where T_I coincides with T_1 , one can increase the value of n to achieve the desired interpolation.

$$p_0 = \phi_+^{(0)}(T_s), \quad (77)$$

$$q_0 = \phi_-^{(0)}(T_s), \quad (78)$$

$$p_1 = \dot{\phi}_+^{(0)}(T_s), \quad (79)$$

$$q_1 = \dot{\phi}_-^{(0)}(T_s), \quad (80)$$

$$p_2 = -\frac{3}{2}p_1 - c_+ p_0, \quad (81)$$

$$q_2 = -\frac{3}{2}q_1 - c_- q_0, \quad (82)$$

equations for T_1 and $\phi_{\pm}(T_1)$ by fitting to examples obtained from the analytic expressions:

$$T_1 \approx T_z - \frac{0.7}{\alpha F} + O\left(\frac{1}{F^2}\right), \quad (89)$$

$$\phi_{\pm}(T_1) \approx F(1 - 0.2\alpha) + O\left(\frac{1}{F}\right). \quad (90)$$

By the self-consistency of the solution and the method of construction involving Eq. (75), the time T_1 itself is

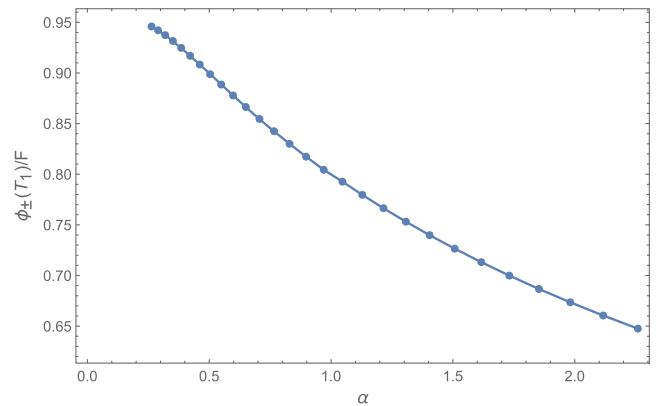


FIG. 2. This plot shows that when $\phi_{\pm}(T)$ cross each other for the first time at T_1 [evaluated by using the highly nontrivial equations (67) and (68)], their values are close to F for the parametric region $\alpha \lesssim 1$ discussed in the text. This curve is insensitive to the choice of $\{c_{\pm}, F, \phi_+(0), \varepsilon_0\}$ except through α given by Eq. (72). We will use this feature to find an analytic approximation to the isocurvature spectrum.

$O((2n)^{\frac{1}{4}}/(\sqrt{\alpha}F))$ away from T_z . Note that as α becomes small, $\varepsilon = (2n)^{\frac{1}{4}}/(\sqrt{\alpha}F)$ increases such that the cubic-polynomial expansion of the background fields in Eqs. (67) and (68) is insufficient and higher order terms become significant. Hence the cubic expansion nonperturbative method utilized here is valid when

$$\frac{p_3(T_I - T_s)^3}{\phi_{+(2)}(T_I)} \lesssim O(r_a), \quad \frac{q_3(T_I - T_s)^3}{\phi_{-(2)}(T_I)} \lesssim O(r_a), \quad (91)$$

where $T_I - T_s = \varepsilon$. Expanding around $\alpha = 0$ yields

$$\frac{3(48 + n)}{432 + 5n + 96\alpha^2(48 + n)} \lesssim O(r_a), \quad (92)$$

which gives us the following lower bound on α :

$$\alpha > \alpha_L \equiv \frac{\sqrt{144 + 3n - 432r_a - 5nr_a}}{4\sqrt{6nr_a + 288r_a}}. \quad (93)$$

For $r_a \sim 0.2$ and $n = 10$ we obtain $\alpha_L \sim 0.25$ serving as a reasonable cutoff for a 20% accurate computation.

In Sec. III, we remarked that as long as $\chi_{\text{HM}} \lesssim O(r_a)$, the decoupling of the lighter and heavier modes is justified. Figure 25 in Appendix J suggests that this is true when α is less than an upper bound given as α_U . Using $r_a \sim 0.2$ we infer that the decoupling is satisfied at the first crossing of the background fields for

$$\alpha \lesssim \alpha_U \equiv 1. \quad (94)$$

Later in Appendix E, we will show that this upper bound is consistent with another analytic procedure where we integrate out the high-frequency UV modes. Thus, the nonperturbative methods and the analytic techniques utilized in this paper are applicable within a specific parametric region defined by the parameter α . Henceforth in this paper, we will limit ourselves to the study of underdamped axionic isocurvature power spectrum applicable to those cases where

$$0.25 \lesssim \alpha \lesssim 1. \quad (95)$$

Interestingly, both the lower and upper bounds are nearly F independent for $F \gg 1$, implying that the parameter α is a suitable parametrization for studying resonant underdamped isocurvature modes. Because we will be interested in resonant cases (to be defined below), α will never be very small in the cases of our main interest. For completeness, the small α cases ($\alpha < \alpha_L$) are discussed in Appendix B.

Additionally, using Eqs. (67) and (68) we note that the flat deviation $|\xi(\phi_+, \phi_-)| \sim O(F^2)$ at the crossing T_1 . This is a unique feature of the underdamped scenario where the flat deviation can tend to $O(F^2)$ if the background fields

cross close to the $\phi_+^{(0)}$ zero crossing ($T_1 \sim T_z - O(1/F)$). Post T_1 , the flat deviation oscillates rapidly with a frequency of $O(F)$ and an $O(F^2)$ amplitude that decays in time with the Hubble friction. These rapid oscillations are identified as resonance. Accordingly, the axion mode function is now characterized by the F scale dynamics till the flat deviation decays or becomes insignificant. This is unlike the overdamped or nonresonant scenarios where the flat deviation is negligible and the mode amplitude dynamics is defined primarily by the H scale throughout.

C. Resonant scenarios

In this work, we focus on initial conditions where the ϕ_+ and ϕ_- initially follow the flat direction of the potential. This corresponds to the initial trajectories approximated by $\phi_{\pm}^{(0)}$ of Eq. (57) for which the flat deviation $\xi(\phi_+^{(0)}, \phi_-^{(0)}) = 0$. For certain parametric cases, there is a significant force on ϕ_+ by ϕ_- through $\xi\phi_-$ when the two fields meet. Such forces cause displacements of ϕ_+ toward the ‘‘steep’’ direction in the potential where ξ is significant. This in turn causes strong⁷ oscillatory behavior of both ϕ_+ and the order unity coupled ϕ_- . We now present a quantitative condition for this class of scenarios which we call *resonant* scenarios.

During each T_{cross} when $\phi_+(T_{\text{cross}}) = \phi_-(T_{\text{cross}})$, the effective coupling force f_+ on ϕ_+ can be expressed as

$$f_+(T_{\text{cross}}) = -\xi\phi_-|_{T_{\text{cross}}}, \quad (96)$$

whose magnitude measures deviation of ϕ_+ from the flat direction trajectory. This deviation is a sufficient condition for the force in the steep direction to be significant. Hence, we define resonant scenarios to be the cases in which

- (1) $\xi\phi_-|_{T=T_c} \gtrsim O(0.1)\dot{\phi}_+(T_c)$,
- (2) $|\phi_+(T_c)| \gtrsim R_c F^2$,

where T_c is the first T_{cross} that satisfies these conditions. The first of the conditions ensures sufficient coupling force f_+ so that ϕ_+ deviates significantly from the perturbed solution $\phi_+^{(0)}$, while the second condition here is required for ϕ_+ to oscillate with an amplitude whose significance is determined by the choice of R_c . For specificity, we will choose $R_c = \alpha_L$.

In summary, we can define T_c to be the time at which

$$\phi_+(T_c) = \phi_-(T_c), \quad (97)$$

for which ϕ_+ has a large kinetic energy and a large deviation from the flat direction. In this paper, we restrict ourselves to only those cases where the fields transition at the first crossing. Therefore $T_c = T_1$ and henceforth we drop the notation T_1 for crossing/transition. While this

⁷The term ‘‘strong oscillatory’’ here refers to the frequency being much larger than that of ω .

choice may seem very restrictive, in principle the model presented in this paper is still applicable to other cases where T_1 does not correspond to T_c (under certain conditions). Such cases will be studied in a separate paper [80].

V. NUMERICALLY MOTIVATED MODEL

After the transition time T_c defined in Eq. (97), the ϕ_+ field takes a large dip toward the negative ϕ_+ direction. During a $O(1/F)$ time period surrounding T_c , the effective mass squared eigenvalues in the instantaneously diagonal mass matrix basis has a large dip of $O(F^2)$. We can capture this behavior in terms of an approximate step function when solving the mode equation in the background of this ϕ_{\pm} system:

$$\partial_T^2 y_1(k, T) + 3\partial_T y_1(k, T) + (K^2 e^{-2T} + [-\dot{e}_1 \cdot \dot{e}_1 + m_1^2(T)]) y_1(k, T) = 0. \quad (98)$$

To model this, define the effective mass squared in instantaneous normalized eigenvector basis shown in Eq. (98) as

$$m_{y_1}^2 \equiv -\dot{e}_1 \cdot \dot{e}_1 + m_1^2, \quad (99)$$

where m_1^2 is the lightest eigenvalue of Eq. (26),

$$m_1^2 = \frac{\tilde{M}_{11}^2 + \tilde{M}_{22}^2}{2} \left(1 - \sqrt{1 + 4 \frac{F^4 - \tilde{M}_{11}^2 \tilde{M}_{22}^2}{(\tilde{M}_{22}^2 + \tilde{M}_{11}^2)^2}} \right), \quad (100)$$

where \tilde{M}_{ij}^2 are the elements of \tilde{M}^2 . Because we will only be interested in the longtime behavior of the zero mode here, we do not need to solve the mode equation with high time resolution. Hence, we use a double perturbative expansion in amplitude and frequency as explained in Appendix C to

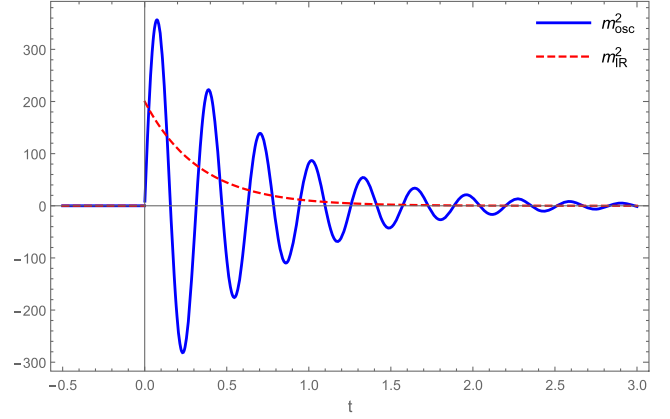


FIG. 3. Shown is an effective IR mass squared (dashed line) obtained from integrating out high-frequency oscillations here illustrated with $m_{\text{osc}}^2 \equiv A e^{-\frac{1}{2}t} \sin[ft]$ (solid line) where t is the dependent variable of this toy function. The effective IR mass squared contribution $m_{\text{IR}}^2 \equiv \frac{1}{2}(A/f)^2 e^{-3t}$ obtained through methods of Appendix C is exponentially decaying with an additional factor of $A/(2f^2)$ coming from the UV propagator. Note that the IR ETSP contribution from the UV modes is positive, consistent with the fact that the UV oscillations are of the decoupling type (i.e., they are not destabilizing).

separate out the low resolution behavior we are interested in. After integrating out the UV modes, we find an effective IR mode mass squared $m^2(T)$ that has only a small number of features. This is illustrated schematically in Fig. 3. In the context of Eq. (100), combined with $m_1^2(T < T_c)$ being c_+ , we see that integrating out the UV modes has generated an effective jump in $m^2(T)$. As one can see in the figure, the effective $m^2(T)$ is significantly simpler than the original $m_{y_1}^2(T)$.

In the step function approximation this can be modeled as

$$m^2 \approx \begin{cases} V_0, & T_0 < T < T_1, \\ -V_1, & T_1 < T < T_2, \\ V_B \text{sqw}(T, T_2, T_B - T_2) + \frac{V_2}{2} e^{-3(T-T_2)} - \sum_{i=3}^n V_i \text{sqw}(T, T_i, \Delta_i), & T_2 < T, \end{cases} \quad (101)$$

where

$$\text{sqw}(T, T_i, \Delta_i) = \begin{cases} 1 & \text{if } T_i \leq T \leq T_i + \Delta_i, \\ 0 & \text{otherwise,} \end{cases} \quad (102)$$

and

$$\text{Pset} \equiv \{V_i, V_B, T_B, T_i, \Delta_i\} \quad (103)$$

are the model parameters for this steplike approximation. In particular, T_1 is defined as the time when IR averaged $m_{y_1}^2$ makes a negative jump, and T_2 is defined as the time after

T_1 when IR averaged $m_{y_1}^2$ makes a positive jump. Later on, we will see that V_B here represents the step approximation of a smooth decaying nonoscillatory nonequilibrium time-dependent axion mass function whose extinction point corresponds to the PQ symmetry-breaking vacuum, where the Goldstone theorem condition is satisfied. The rest of the square well bumps are supposed to be approximations of an oscillatory nonequilibrium time-dependent axion mass function. This in turn means that

$$T_B - T_2 \gg \Delta_i$$

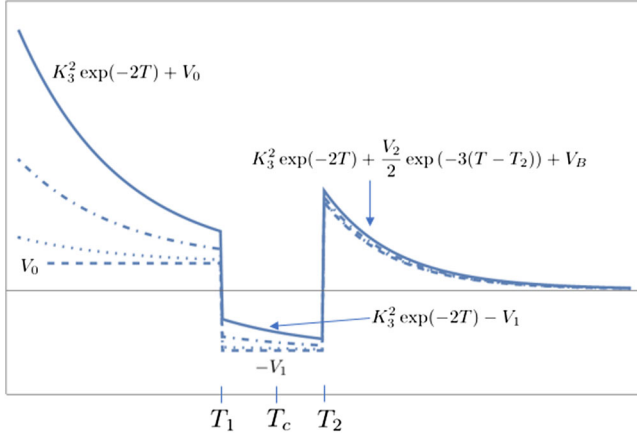


FIG. 4. Schematic diagram of the mass model highlighting key features for a single dip case. The dashed curve represents $m^2(T)$. The dotted and dot-dashed curves have the addition of $K_1^2 \exp(-2T)$ and $K_2^2 \exp(-2T)$, respectively, to $m^2(T)$. The K_n values have the hierarchy of $K_3 > K_2 > K_1$. The constant V_B applicable for the region $T > T_2$ is typically small as suggested implicitly in this schematic figure. Given that this figure is schematic, the K_n here should not be confused with objects such as K_2 in Eq. (180).

in this parametrization. Figure 4 shows a schematic depiction of the mass model highlighting its key features for a single dip case.

Although this model can in principle be parametrized with an arbitrary number of steplike features controlled by $\{V_i, T_i, \Delta_i\}$, we will in practice consider at most two such features (i.e., T_i will have at most $i \in \{0, 1, 2, 3\}$ in this paper where the two dips occur in the intervals $[T_1, T_2]$ and $[T_3, T_3 + \Delta_3]$ with $T_2 = T_1 + \Delta_1$). The second dip (V_3) occurs when $\alpha \gtrsim \alpha_2$, where α_2 is defined in Eq. (150). It corresponds to the situation where the background fields ϕ_{\pm} cross each other again after T_c . Since we choose $c_+ > c_-$ throughout this paper, there will always be an even number of crossings between the two background fields after T_c . Every such crossing corresponds to a dip in the ETSP within the framework of our mass model. By limiting the current analysis to two dips, we consider only those cases where a third dip is less than $O(1)$ in magnitude. This corresponds to all cases where $\alpha \lesssim \alpha_3$ with α_3 defined by Eq. (F13). Other cases can be treated by including additional steplike features as elucidated previously. With an underlying theory such as Eq. (8), the parameters Pset can be computed in terms of $\{c_+, c_-, F\}$. However, here we will first solve this system analytically, then later express the parameters in terms of $\{c_+, c_-, F\}$.

A. Piecewise solution (scattering matrix approach)

In this subsection, we would like to derive an expression for (y_1, \dot{y}_1) at some final time T_N given its value at some initial time T_0 , assuming that we know the approximate forms of the solution in N discrete time regions.

Consider a time region R_j with boundaries $[T_j, T_{j+1}]$. As per this convention, the first region lying between T_0 and T_1 is termed R_0 . The y_1 -mode function within any region can be expressed through superposition of linearly independent basis functions $\psi_{1,2}^{(R_j)}$:

$$y_1(K, T) = \begin{cases} c_1^{(R_0)} \psi_1^{(R_0)} + c_2^{(R_0)} \psi_2^{(R_0)}, & T \in [T_0, T_1], \\ c_1^{(R_1)} \psi_1^{(R_1)} + c_2^{(R_1)} \psi_2^{(R_1)}, & T \in [T_1, T_2], \\ \dots, & \dots, \end{cases} \quad (104)$$

with the Wronskian $W^{(R_j)}(T) = \dot{\psi}_2^{(R_j)} \psi_1^{(R_j)} - \psi_2^{(R_j)} \dot{\psi}_1^{(R_j)}$. We will take different approximate forms of $\psi_{1,2}^{(R_n)}$ in each of the regions R_n and match the value and its derivatives at the boundaries to construct y_1 in the entire domain $\cup_n R_n$ as will be described below.

Let us define the Y , Ψ , and C matrices by rewriting

$$\begin{bmatrix} y_1 \\ \dot{y}_1 \end{bmatrix} = \begin{bmatrix} \psi_1^{(R_j)} & \psi_2^{(R_j)} \\ \dot{\psi}_1^{(R_j)} & \dot{\psi}_2^{(R_j)} \end{bmatrix} \begin{bmatrix} c_1^{(R_j)} \\ c_2^{(R_j)} \end{bmatrix}$$

as

$$Y = \Psi^{(R_j)} C^{(R_j)}, \quad (105)$$

where

$$\Psi^{(R_j)} \equiv \begin{bmatrix} \psi_1^{(R_j)} & \psi_2^{(R_j)} \\ \dot{\psi}_1^{(R_j)} & \dot{\psi}_2^{(R_j)} \end{bmatrix} \quad (106)$$

and $Y \equiv (y_1, \dot{y}_1)$. The coefficients $C^{(R_j)}$ within the region R_j are given by the expression

$$C^{(R_j)} = \Psi^{(R_j)-1}(T_j^+) Y(T_j^-). \quad (107)$$

Here T_j^- indicates the incoming y_1 -mode function from the left-hand side. The solution Y at T_{j+1}^- as the mode exits region R_j is $\Psi^{(R_j)}(T_{j+1}^-) C^{(R_j)}$. The function at $T = T_{j+1}^-$ can be constructed as

$$\begin{aligned} Y(T_{j+1}^-) &= \Psi^{(R_j)}(T_{j+1}^-) C^{(R_j)} \\ &= \Psi^{(R_j)}(T_{j+1}^-) \Psi^{(R_j)-1}(T_j^+) Y(T_j^-) \\ &\equiv S(T_{j+1}, T_j) Y(T_j^-), \end{aligned}$$

where the matrix $S(T_{j+1}, T_j)$ acts as a scattering propagator for the y_1 -mode function from time T_j to T_{j+1} through the

time slice R_j . The mode function at time T_N after passing through N piecewise continuous regions is given as

$$Y(T_N^-) = \prod_{j=0}^{N-1} S(T_{j+1}, T_j) Y(T_0). \quad (108)$$

B. Independent analytic functions in each piecewise region

We shall now give the general linearly independent basis functions $\psi_{1,2}$ for the form of functions that appear within our model. Let us consider the following second order ordinary differential equation (ODE) as a generic case for a y_1 -mode equation,

$$\partial_T^2 y_1(K, T) + 3\partial_T y_1(K, T) + (K^2 e^{-2T} + m^2(T)) y_1(K, T) = 0. \quad (109)$$

In each piecewise region $[[T_j, T_{j+1}]$ in Eq. (101) of our $m^2(T)$ model, its behavior is either a constant or an exponentially decaying function. Let us consider these two situations case by case.

- (1) const $\equiv c$, where c can either be positive or negative. For this case, the above ODE has following linearly independent solutions:

$$\psi_1 = e^{-\frac{3}{2}T} J_{\sqrt{9/4-c}}(K e^{-T}), \quad (110)$$

$$\psi_2 = e^{-\frac{3}{2}T} Y_{\sqrt{9/4-c}}(K e^{-T}). \quad (111)$$

- (2) exponentially decaying $\equiv V e^{-3T}$ for some arbitrary $V > 0$. The effective frequency squared

$$K^2 e^{-2T} + V e^{-3T} \quad (112)$$

now has two different orders of decaying exponentials. A fundamental intuition for these mode function time evolutions is that whenever $K^2 e^{-2T} + m^2(T) > 0$, $|y_1(T)|$ has a tendency to decay while for the opposite sign, $|y_1(T)|$, has a tendency to increase. This can be viewed as the result of the equation with $K^2 e^{-2T} + m^2(T) = 0$ having a constant solution (similar to the usual inflationary adiabatic mode) which makes $K^2 e^{-2T} + m^2(T) = 0$ a ‘‘point’’ of criticality in a family of differential equations represented by Eq. (109). This means that the sign of $m^2(T)$ is fundamental to understanding the mode amplitude evolution as a function of time. Moreover, this behavior of mode functions is a fundamental element of quantum fields in curved spacetime.

To solve Eq. (109) analytically, we define an approximate frequency squared $U(T)$ as explained below and further divide the region of interest into subregions such that the ODE can be approximated as

$$\ddot{y}_1 + 3\dot{y}_1 + U(T)y_1(T) \approx 0. \quad (113)$$

The idea for the approximation is that competing terms of the form

$$A_1 e^{-2T} + A_2 e^{-3T} \quad (114)$$

have only one term dominating except for at most a brief period when the two terms become comparable. During this ‘‘comparable’’ time period, the Taylor expansion of the time dependence is

$$A_1 e^{-2T} + A_2 e^{-3T} \approx 2A_1 e^{-2T_X} \left(1 - \frac{5}{2}(T - T_X)\right) \quad (115)$$

$$\approx 2A_1 e^{-2T_X} \exp\left(-\frac{5}{2}(T - T_X)\right), \quad (116)$$

where we have linearly expanded about the equality time T_X when the A_1 and A_2 terms are equal. Note that the first of Eq. (114) will dominate over the second term in a time period of $\Delta T \sim O(1)$. During this time period about T_X , the fractional error between Eq. (116) and the exact equation (114) is

$$\frac{\text{exact} - \text{approx}}{\text{exact}} = 1 - \frac{1}{\cosh\left(\frac{T - T_X}{2}\right)}, \quad (117)$$

which is about 0.2 for the maximum value of $T - T_X = 2 \ln 2$ that we take below. This lack of sensitivity is an accidental property of the $\cosh(x)$ which has a flat region at $x = 0$.

Now, let us discuss in detail how this approximation is implemented in the model of Eq. (101). At time T_2 , there is a jump in the m^2 of Eq. (101) due to the term V_2 . We will denote the jump amplitude in the effective frequency squared $U(T)$ as V in this generically parametrized analysis here. Because the V term decays faster than the K^2 term, $U(T)$ will need to take into account the K^2 term. We define T_V as the time when V term is equal to the full $U(T)$ that includes the K^2 term. Subsequently, $U(T)$ decays according to the approximate expression of Eq. (116). Eventually, the V term in $U(T)$ will be negligible, and only the K^2 term will need to be kept. Since the K^2 term decays slower than the approximate $U(T)$ in Eq. (116), the expression for $U(T)$ will need to be changed to keeping just the K^2 term when $U(T)$ term equals the K^2 term at T_K .

The previous paragraph can be explicitly expressed in terms of the effective frequency equation as

$$U(T) - c = \begin{cases} V e^{-3T_X} e^{-3(T - T_X)}, & T_2 < T < T_V, \\ (K^2 e^{-2T_X} + V e^{-3T_X}) e^{-\frac{5}{2}(T - T_X)}, & T_V < T < T_K, \\ K^2 e^{-2T_X} e^{-2(T - T_X)}, & T_K < T < T_\infty. \end{cases} \quad (118)$$

Thus, the time interval $[T_2, T_\infty]$ is subdivided into three piecewise regions, where each region is characterized by a distinct exponential decay rate such that the system of the differential equation in Eq. (109) is now analytically solvable in each subregion. We define T_X as when $K^2 e^{-2T}$ and $V e^{-3T}$ are equal,

$$T_X = \ln\left(\frac{V}{K^2}\right), \quad (119)$$

while T_V and T_K are defined as the time boundaries that connect the piecewise regions continuously:

$$T_V = T_X - 2 \ln\left(1 + \frac{K^2 e^{-2T_X}}{V e^{-3T_X}}\right) = T_X - 2 \ln 2 = \ln\left(\frac{V}{4K^2}\right), \quad (120)$$

$$T_K = T_X + 2 \ln 2 = \ln\left(\frac{4V}{K^2}\right). \quad (121)$$

To further improve the accuracy of the above piecewise technique, the amplitude of the exponentials in each subregion is evaluated as an integrated average of $K^2 e^{-2T} + V e^{-3T}$ as follows:

$$\frac{\int dT (K^2 e^{-2T} + V e^{-3T})}{\int dT e^{-nT}}, \quad (122)$$

where $n \in \{3, 5/2, 2\}$ in each subregion. Using the definition of T_X and the amplitude defined above, the expression for $U(T)$ in Eq. (118) simplifies to

$$U(T) - c = \begin{cases} \left(V + K^2 \frac{3/2(e^{T_2} + e^{T_V})}{1 + 2 \cosh(T_2 - T_V)}\right) e^{-3T}, & T_2 < T < T_V, \\ \left(\frac{3125}{1364} K \sqrt{V}\right) e^{-\frac{5}{2}T}, & T_V < T < T_K, \\ \left(K^2 + V \frac{1 + 2 \cosh(T_K - T_\infty)}{3/2(e^{T_K} + e^{T_\infty})}\right) e^{-2T}, & T_K < T < T_\infty. \end{cases} \quad (123)$$

In each subregion now the ODE has a Bessel solution of order $(\sqrt{9/4 - c})/n$ for an ETSP of the form $U(T) = A^2 e^{-nT} + c$:

$$\psi_1 = e^{-\frac{3}{2}T} J_{\frac{\sqrt{9-4c}}{n}}\left(\frac{2}{n} A e^{-\frac{n}{2}T}\right), \quad (124)$$

$$\psi_2 = e^{-\frac{3}{2}T} Y_{\frac{\sqrt{9-4c}}{n}}\left(\frac{2}{n} A e^{-\frac{n}{2}T}\right), \quad (125)$$

such that the general solution is a superposition of $\psi_{1,2}$.

VI. ISOCURVATURE SPECTRUM RELATION TO MODEL PARAMETERS

In this section, we give analytic expressions for the numerically motivated model parameters and provide isocurvature power spectrum results in certain regions of the underlying model space $\{c_+, c_-, F\}$. The parameter region is most efficiently divided by α introduced in Eq. (72). Small α resonance corresponds to the dynamics of the background field with a $\dot{\phi}_+(T_c)$ (where T_c is as defined in Sec. IV C) that is neither too small (in which case the dynamics is not resonant) nor large (in which case, the dynamics becomes difficult to predict due to the large series of nonlinear interactions involved). More precisely, we define this set of resonant cases by Eq. (95):

$$0.25 \lesssim \alpha \lesssim 1. \quad (126)$$

We present below the analytic formula for the isocurvature spectrum in this corner of the parameter space.

A. General map of analytic model parameters to $\{c_+, c_-, F\}$

As defined previously, the mass model has following set of parameters:

$$\text{Pset} \equiv \{V_i, V_B, T_B, T_i, \Delta_i\}. \quad (127)$$

The final y_1 mode amplitude is evaluated in terms of these model parameters. Below we will give a map of these model parameters in terms of $\{c_+, c_-, F\}$ and then provide analytic expressions for their evaluations. We limit ourselves to $i = 3$ that cover up to double dip cases in Eq. (101). With $\alpha \lesssim \min(\alpha_3, \alpha_U)$ the general map is

$$V_0 \approx c_+, \quad (128)$$

$$V_1 \approx |\min(m_1^2 - \dot{e}_1 \cdot \dot{e}_1)|, \quad (129)$$

$$V_2 \approx A^2 \langle \beta^2 \rangle, \quad (130)$$

$$T_0 = 0, \quad (131)$$

$$T_1 \approx T_c - \left(\frac{3.11 - 1.05\alpha}{2F}\right), \quad (132)$$

$$T_2 \approx T_c + \left(\frac{3.11 - 1.05\alpha}{2F}\right), \quad (133)$$

with the additional second dip for $\alpha \gtrsim \alpha_2$ given by the following expressions:

$$V_3 \approx \begin{cases} (\dot{e}_1^2)_{\max} e^{-3(T_3 - T_c)}, & \frac{A e^{-3/2(T_3 - T_c)}}{2F^2} > 0.15, \\ (\dot{e}_1^2)_{\max} \left(\frac{\dot{y}_s(T_3)}{\dot{y}_s(T_c)}\right)^2, & \frac{A e^{-3/2(T_3 - T_c)}}{2F^2} < 0.15, \end{cases} \quad (134)$$

$$\phi_{-s}(T_3) \approx F \quad \text{for } T_3 > T_c, \quad (135)$$

$$\Delta_3 \approx \frac{0.72}{\sqrt{V_3}}. \quad (136)$$

Further, the background mass parameter V_B for single and double dip cases is defined as follows:

$$V_B \approx \begin{cases} c_- + \frac{1}{(T_L - T_2)} \left(\frac{1063}{3072} + \frac{106793c_-}{393216c_+} \right), & \alpha < \alpha_2, \\ V_{B2}(T), & \alpha_2 < \alpha, \end{cases} \quad (137)$$

$$T_B \approx \begin{cases} T_L, & \alpha < \alpha_2, \\ T_3 + \Delta_3 + \frac{2}{\Lambda}, & \alpha_2 < \alpha, \end{cases} \quad (138)$$

$$V_{B2}(T) \equiv \begin{cases} c_-, & T_2 < T < T_3 + \Delta_3, \\ \frac{\Lambda}{2} \int_0^\infty \frac{c_- c_+ (c_+ n^4 - c_-) (-1 + n^4)}{(c_+ n^4 + c_-)^2} dT, & T_3 + \Delta_3 < T < T_B, \\ 0 & \text{otherwise,} \end{cases} \quad (139)$$

where

$$T_L \approx T_2 - \left(\frac{3}{c_-} \right) \ln \left(\frac{2 \sin(\pi n_1) 2^{2-n_1} \Gamma(1-n_1) \phi_{-\min} x^{n_1}}{\pi(3\phi_{-s}(T_2)x \partial_x J_{n_1}(x) + (3\phi_{-s}(T_2) + 2\dot{\phi}_{-s}(T_2))J_{n_1}(x))} \Big|_{x=\frac{\Lambda\sqrt{2}}{3\Omega}} \right) \quad \text{for } c_- \ll 1, \quad (148)$$

$$\Lambda \approx \frac{3}{2} - \sqrt{\frac{9}{4} - \frac{4c_- c_+}{c_- + c_+}}, \quad (149)$$

$$\frac{3}{F} \approx \frac{J_1(\sqrt{2}A/(3\bar{\Omega}))}{\sqrt{2}A/(3\bar{\Omega})} \Big|_{\alpha=\alpha_2}, \quad (150)$$

where $\phi_{-s}(T > T_2)$ is given in Eq. (E10), and $\phi_{-s}(T_2)$ and $\dot{\phi}_{-s}(T_2)$ are given in Eq. (E14), while $\phi_{-\min} = \phi_{-}(T_\infty)$. Quite noticeably, the analysis turns very arduous by the addition of a second dip. Precisely for this reason, in Sec. VII we will give closed form analytic expressions for the axion isocurvature spectrum corresponding to single dip cases only. Although we will sketch the motivation and the details of the derivation in the Appendixes F–I, here we describe the intuition behind this map of the approximation parameters to the underlying model.

The parameter V_0 represents the effective axion mass before T_1 . During this time the mass is nearly constant because the background fields are following a flat direction such that the potential does not change as the fields change. The V_1 dip at $T_1 \approx T_c$ is the type of frame-dependent eigenvalue rotation mass effect seen in Eq. (129). It is

$$T_c \approx T_z - \frac{0.7}{\alpha F}, \quad (140)$$

$$-A \equiv \min(\xi), \quad (141)$$

$$\langle \beta^2 \rangle \approx F^{-2} \left(0.138 + \frac{.14}{1.1 + \exp(11(\alpha - 0.72))} \right), \quad (142)$$

$$g_s(T \gtrsim T_2) \approx \phi_{-s}^2 - \frac{F^4}{\phi_{-s}^2}, \quad (143)$$

$$\bar{\Omega} \approx 2.05F + \frac{0.133F + 0.045F^2}{1 + \exp(7.86(\alpha - 0.744 + 0.0008F))}, \quad (144)$$

$$n \equiv n(T) \approx 1 - \frac{1}{3} \exp(-\Lambda T), \quad (145)$$

$$n_1 = \sqrt{1 - 4c_-/9}, \quad (146)$$

$$n_2 = \sqrt{1 - 8c_-/9}, \quad (147)$$

characterized by the superposition of the $-(\dot{e}_1)^2$ and m_1^2 dipoles close to T_c with a phase separation μ between the lighter eigenvalue and the corresponding eigenvector rotation gradient effects. The phase separation is α dependent. Fields with small α tend to have an almost coincident superpositioning of the dipoles and thus correspond to a small μ . This α dependence can be understood by referring to the location of the two dipoles and their subsequent superposition. From Eq. (157) and Appendix F, we infer that the location of the first $-(\dot{e}_1)^2$ dip corresponds to the time when the ϕ_+ field tends to F . Meanwhile Fig. 2 suggests that fields with small α transition close to F and the m_1^2 dip reaches a minimum soon after transition. Therefore, as α increases, the background fields transition farther from F such that the separation between the two dipoles widens, resulting in an increased phase separation μ . For smaller α , the two dipoles are almost coincident, resulting in a smaller phase separation.

After the V_1 dip, at time T_2 , there is a jump in the effective mass squared due to the strong nonlinear interactions through $\xi\phi_\pm$ Eq. (21). The jump amplitude is approximately V_2 , and after the jump, there is an exponential decay (see Fig. 3) which captures the results of the UV modes that have been integrated out. This UV mode averaging has the effect of multiplying the

ETSP $A \sim O(F^2)$ by the amplitude of the UV mode A divided by the propagator $1/k^2 \sim 1/F^2$, resulting in

$$\frac{A^2}{F^2} \sim O(F^2). \quad (151)$$

V_3 represents the next $(\dot{e}_1 \cdot \dot{e}_1)$ dip, whose physics is similar to the first $(\dot{e}_1 \cdot \dot{e}_1)$ dip modified by the Hubble friction. Meanwhile, the parameter V_B for $\alpha < \alpha_2$ is a constant of $O(c_-)$ that represents the average mass squared function m_B^2 over the time interval from $[T_2, T_B]$, as detailed in Appendix I. The dynamics of the m_B^2 function is controlled by the slow-varying IR components of the background fields. For $\alpha \lesssim \alpha_2$ it is effectively positive and leads to the decay of the mode amplitude, whereas for $\alpha > \alpha_2$ it is negative and results in mode amplification.

The width of each dip can be evaluated analytically by taking the ratio of the net area under the peak to its maximum amplitude. In principle, the width of a $(\dot{e}_1 \cdot \dot{e}_1)$ dip increases for larger i as the amplitude of each dip decreases. This can be qualitatively understood by the fact that the velocity of the fields governing the dip widths are proportional to the amplitude of the fields which is proportional to the square root of

$$\dot{e}_1 \cdot \dot{e}_1 \sim \sum_{nm} d_{nm}(\phi_+, \phi_-) \frac{\dot{\phi}_n \dot{\phi}_m}{F^2}. \quad (152)$$

Hence, as shown in Appendix F, the dip width can be parametrized as

$$\Delta_{(\dot{e}_1)^2} \approx \frac{0.72}{\sqrt{\dot{e}_1 \cdot \dot{e}_1}}. \quad (153)$$

The fact that the 0.72 appears in the above expression approximately independently of other parameters is due to the fact that we are focusing on the parametric region where the maximum field excursion parametric dependences are canceled (see Appendix F). Using the analytically obtained polynomial fit for $(\dot{e}_1 \cdot \dot{e}_1)_{\max}$ from Appendix F, the width Δ of the first $(\dot{e}_1 \cdot \dot{e}_1)$ dip can be expressed in terms of α as

$$\Delta_{(\dot{e}_1)^2_{\max}} \approx \frac{(2.93 - 1.86\alpha)}{F} \quad \forall 0.25 \lesssim \alpha \lesssim 1, \quad (154)$$

which highlights that the dip width reduces with an increasing α or with the incoming velocity of the ϕ_+ field.

A similar expression for the width $T_2 - T_1$ of the V_1 dip is given below:

$$T_2 - T_1 \approx \frac{(3.11 - 1.05\alpha)}{F} \quad \forall 0.25 \lesssim \alpha \lesssim 1. \quad (155)$$

By rewriting the width $T_2 - T_1$ in terms of $\Delta_{(\dot{e}_1)^2_{\max}}$, we obtain the following relation:

$$T_2 - T_1 \approx \Delta_{(\dot{e}_1)^2_{\max}} + \frac{\alpha}{F}. \quad (156)$$

As expected the width of the V_1 dip is broader than the width of the first $(\dot{e}_1 \cdot \dot{e}_1)$ dip. For small $\alpha \sim O(0.1)$ scenarios, the width of the V_1 dip is nearly equivalent to that of the $(\dot{e}_1 \cdot \dot{e}_1)$. This situation corresponds to a small phase separation μ such that the $-(\dot{e}_1 \cdot \dot{e}_1)$ and m_1^2 dips almost coincide.

Next within our model, the logarithmic functional dependence of $T_3 - T_1$ comes from the exponentially decaying frequency of $\dot{e}_1 \cdot \dot{e}_1$ oscillations, as explained in Appendix F.

From the above parameter assignments, we shall now give expressions for $(\dot{e}_1 \cdot \dot{e}_1)_{\max}$ and A . These are defined as follows:

$$(\dot{e}_1 \cdot \dot{e}_1)_{\max} \approx \left(\frac{\dot{g}}{5F^2} \right)^2 \left(1 + \frac{4}{5} \left(\frac{g + F^2}{F^2} \right) + \frac{2}{25} \left(\frac{g + F^2}{F^2} \right)^2 - \frac{28}{125} \left(\frac{g + F^2}{F^2} \right)^3 \right) \Big|_{\phi_+ \rightarrow F}, \quad (157)$$

$$g = \tilde{M}_{11}^2 - \tilde{M}_{22}^2, \quad (158)$$

$$\tilde{M}_{11}^2 \equiv c_+ + \phi_-^2, \quad (159)$$

$$\tilde{M}_{22}^2 \equiv c_- + \phi_+^2, \quad (160)$$

$$\dot{g} = 2\dot{\phi}_- \phi_- - 2\dot{\phi}_+ \phi_+, \quad (161)$$

where the ϕ_{\pm} fields are as defined in Eqs. (67) and (68). By $\phi_+ \rightarrow F$, we are denoting that functions such as $\phi_-(T)$ are to be evaluated at the specific time T_F when $|\phi_+(T_F)| = F$.

Next we estimate the amplitude A of the flat deviation $\xi(\phi_+, \phi_-)$. As shown in Appendix D, ξ can be approximately represented via sinusoidal oscillations that drive the resonant exchange of energy between the ϕ_+ and ϕ_- fields. For $T > T_c$, we can express ξ as

$$\xi(\phi_+, \phi_-) \approx -A e^{-\frac{3}{2}(T-T_m)} \cos \left(\int_{T_m}^T \Omega(t) dt \right), \quad (162)$$

where $T_m \approx T_c + O(1/F)$ and $\Omega \sim O(F)$ is an approximate frequency of oscillations. In order to determine A , we solve for the ϕ fields post transition using another set of cubic polynomials with primed coefficients

$$\text{parameters for } T > T_c: p'_i, q'_i, \quad (163)$$

where the primed coefficients are used to distinguish between the nonprimed ones in Eqs. (67) and (68). The eight coefficients are evaluated using similar expressions as in Sec. IV B, where the initial conditions must now be evaluated at the resonant transition time $T_1 = T_c$ (instead of T_s) and choose instead the interpolation point

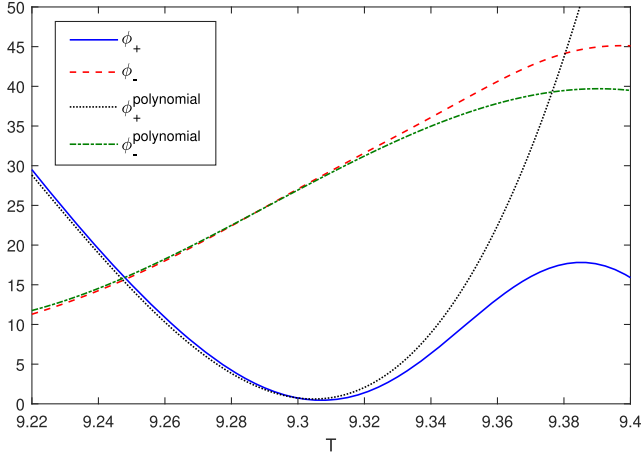


FIG. 5. Shown are the polynomial background $\phi_{\pm}(T)$ solutions given in Eqs. (67) and (68) with parameters changed to those of Eq. (163). These solutions accurately track the numerical solutions over the interval $[T_c, T_m]$, where T_m is the time at which the minimum of the $\phi_+(T)$ occurs. Shown in the figure for comparison is the numerical solution with $c_+ = 2.35$ and a standard fiducial set P_A of parameters that we will use throughout this paper: $P_A \equiv \{F = 20.2, c_- = 0.5, \varepsilon_0 = 0, \phi_+(0) = 0.1M_p/H\}$.

$T_l = T_c + \varepsilon$ [where ε is defined in Eq. (88)]. Finally we evaluate A as

$$-A \equiv \min(\xi) \quad (164)$$

$$= \min(\phi_+(T)\phi_-(T) - F^2). \quad (165)$$

For $\alpha \lesssim 1$ cases where the minima of ξ roughly corresponds to the first minima of ϕ_+ , we can estimate A by evaluating the location T_m where $\dot{\phi}_+(T_m) = 0$,

$$T_m = T_c + \delta T_m. \quad (166)$$

$$\delta T_m \equiv \frac{-p'_2 + \sqrt{p_2'^2 - 3p_1'p_3'}}{3p_3'}, \quad (167)$$

which gives us

$$-A \approx \xi(T_m) = \frac{\ddot{\phi}_+}{\phi_-} \Big|_{T=T_m} \quad (168)$$

$$\approx -\frac{2p'_2 + 6p'_3\delta T_m}{q'_0 + q'_1\delta T_m + q'_2\delta T_m^2 + q'_3\delta T_m^3}. \quad (169)$$

The coefficients turn out to be

$$q'_0 \sim p'_0 \sim O(F), \quad (170)$$

$$q'_1 \sim p'_1 \sim q'_2 \sim p'_2 \sim O(F^2), \quad (171)$$

$$q'_3 \sim p'_3 \sim O(F^3), \quad (172)$$

and the actual parametric dependence of q'_3 and p'_3 with c_{\pm} is extremely complicated, as can be seen in Sec. IV B. We show comparisons with the numerical results for $c_+ = 2.35$ in Figs. 5 and 6.

Remarkably, despite the complicated parametric dependence of Eq. (172) in terms of c_+ , the parametric dependence of A in terms of α is very simple, as can be seen in Fig. 6. For $\alpha \lesssim 2$, we can give a third order polynomial fit for the amplitude A ,

$$A(\alpha, c_+ = 0.5) \approx F^2(-0.089 + 0.479\alpha + 0.599\alpha^2 - 0.170\alpha^3), \quad 0.25 \leq \alpha \lesssim 2, \quad (173)$$

where all the c_+ dependence is contained in $\alpha(c_+)$ through Eq. (74). In this expression, α is not bounded from above by $\alpha_U \sim 1$ because the determination of A or $(\dot{e}_1)_{\max}^2$ is independent of mode decoupling or ETSP evaluation.

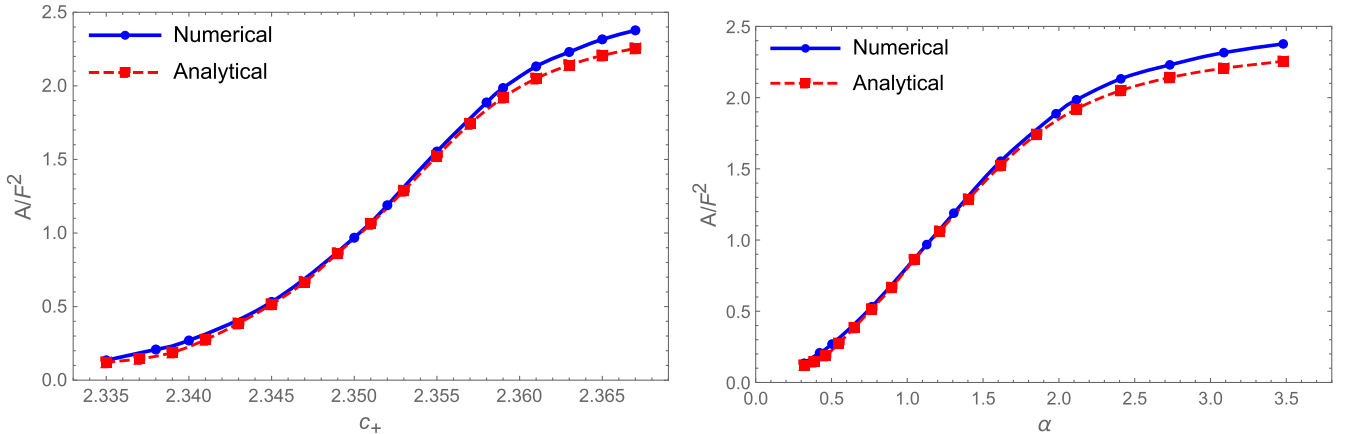


FIG. 6. Equation (169) using an analytic cubic order polynomial expansion is compared with the value of A obtained by putting the numerically solved ϕ_{\pm} into Eq. (165). Fiducial parameter set P_A of Fig. 5 is used.

Instead the above evaluation is valid as long as the ϕ fields can be successfully expressed via a cubic expansion. As α gets close to 2, the $|\phi_+|$ field becomes much larger than F after crossing zero. Correspondingly the ϕ_- field undergoes rapid oscillations due to the heavy mass coming from $|\phi_+| > F$. These rapid ϕ_- oscillations cannot be captured by the cubic polynomial in T and the analytic method described above breaks down. Consequently, the analytic estimation of the minima of ξ soon after T_c is lower than the one obtained numerically, as shown in Fig. 6.

Note that α depends only on c_+ in Eq. (74) because by definition we are neglecting the backreaction from ϕ_- in considering the initial velocity condition of $\dot{\phi}_+$. This type of parametrization is natural since $\dot{\phi}_+$ is very large [$O(F^2)$] in the resonant scenario where we are giving our analytic results. Nonetheless, given that the analytic results are formulaically (as opposed to numerically) fitting the actual background field solutions to polynomials before and after T_c that contain c_- , our analytic results fully capture the c_- dependence in the resonant cases considered here.

We remark that the presence of the V_3 dip is implicitly dependent upon the strength of the flat-deviation amplitude A . The V_3 dip is associated with a second $\dot{e}_1 \cdot \dot{e}_1$ dip which occurs when the two background fields cross each other again after transition at T_c . This second crossing after T_c is controlled by the condition given in Eq. (F11) that is dependent upon A and F . Including the expression for the amplitude A from above, we find that the second dip occurs for $\alpha \gtrsim \alpha_2$.

Although the interpolation method used in this analytic result seems somewhat *ad hoc*, the results are consistent with a more systematic expansion around T_c , as described in Appendix A.

B. The isocurvature spectrum

The axion isocurvature spectrum is given in Eq. (27). We note that

$$\lim_{T \rightarrow T_\infty} I_- = -rI_+, \quad (174)$$

where we define $r = \sqrt{c_+/c_-}$ and simplify Eq. (27) further in terms of the y_1 -mode function,

$$\Delta_s^2(k) \approx \omega_a^2 \frac{4K^3}{\pi^2} |y_1(K, T_\infty)|^2 \frac{r(1+r^4)}{(1+r^2)^3} \frac{1}{\theta_+^2 F^2}. \quad (175)$$

The $y_1(K, T_\infty)$ is solved using the model of Eq. (101), the approximations of Sec. VB, and its associated model parameters in Sec. VIA. Let us now sketch the steps involved in a bit more detail.

First, we set up the approximate BD equivalent leading adiabatic order boundary condition for the $y_1(K, T)$ -mode equation at time T_0 for K modes that satisfy $K^2 \tau_0^2 \gg c_+ - 2$:

$$y_1(K, T_0) = \frac{1}{a(T_0)\sqrt{2K}} e^{-iK\tau_0},$$

$$\partial_T y_1(K, T_0) = \frac{(iK - a(T_0))}{(a(T_0))^2 \sqrt{2K}} e^{-iK\tau_0}, \quad (176)$$

where

$$\tau \equiv -\frac{1}{a(T)H} \quad (177)$$

is the conformal time with the scale factor $a(T) = e^T$, and evaluate the first scattering matrix $S(T_1, T_0)$ of Eq. (108) using the solutions of Sec. VB evaluated with Eqs. (110) and (111). Using the solution from $S(T_1, T_0)$ for the region $[T_0, T_1]$ we obtain the initial conditions for $y_1(K, T)$ at $T = T_1$, when the nonadiabatic rotation of the mass eigenvector becomes strong. Next until T_2 when the mass squared jumps, the solutions used to evaluate $S(T_2, T_1)$ are again Eqs. (110) and (111), but with a tachyonic constant mass squared. Afterward, until time T_3 when the rotation of the mass eigenvector becomes strong again, the effective frequency squared is

$$V_2 e^{-3(T-T_2)}/2 \quad (178)$$

(this is what we will call the jump ETSP, which is obtained after integrating out the UV modes). The solution in this region to be used in $S(T_3, T_2)$ of Eq. (108) is governed by the superposition of Eqs. (124) and (125) via the approximations of the $U(T)$ in Eq. (118). The initial conditions at T_2 should be modified due to the UV integration (highlighted in Appendix C). This is primarily done by scaling the $y_1(T_2)$ and its derivative by a Q matrix as follows:

$$Q = \begin{pmatrix} 1 & 0 \\ -\sqrt{V_2} & 1 \end{pmatrix}. \quad (179)$$

The region (T_2, T_3) is subdivided into time intervals whose boundaries are dependent on K and the amplitude of the jump ETSP through Eq. (119). The gentle time-dependent changes in $U(T)$ exponents are most critical for the intermediate modes that satisfy the condition $Ke^{-T} < 1$ slightly after the transition time T_1 while the jump ETSP is still significant. Starting at time T_3 , the cycle repeats with the eigenvector rotation becoming strong, although with a smaller magnitude than at T_1 . The final $y_1(K, T_\infty)$ is obtained via Eq. (108), where we select $T_N = T_\infty$. In our calculations we set $T_0 = 0$ and $T_\infty = 35$, after which the background fields oscillations are negligible.

Next we remark that this model has been constructed using only the lightest mass eigenmodes to keep it analytically tractable. Even then, we see that the analytic results are complicated and borders on ‘‘intractable.’’ Hence, this model is applicable up to a maximum K mode

before the coupling from the heavier y_2 mode becomes significant: i.e., $K \lesssim K_2$,

$$K_2 \equiv m_2 \frac{a(T_c)}{a(0)} \quad (180)$$

[where $m_2 \sim O(F)$]. However, if K becomes sufficiently large far beyond this heavy-mode coupling values, the dynamics eventually becomes identical to the usual massless axion dynamics. This usual plateau isocurvature spectrum exists for $K \gtrsim K_P$, where

$$K_P \approx \begin{cases} \frac{a(T_2)}{a(0)} \exp(T_L - T_2) \left(\frac{1}{3r_a}\right)^{\frac{1}{\Lambda}}, & \alpha < \alpha_2, \\ \frac{a(T_2)}{a(0)} \exp(2(T_4 - T_2)) \left(\frac{1}{3r_a}\right)^{\frac{1}{\Lambda}}, & \alpha_2 < \alpha < \alpha_3, \end{cases} \quad (181)$$

$$\Lambda \approx \frac{3}{2} - \sqrt{9/4 - \frac{4c_- c_+}{c_- + c_+}}, \quad (182)$$

corresponding to the wave vector modes that leave the horizon after the background fields have settled to a $(1 - r_a)$ fraction of their respective minima. Therefore, the only part of the spectrum that we do not have a prediction for (in this small α case) is the K range $[K_2, K_P]$.

In Fig. 7, we give plots of the axion isocurvature spectrum generated by the above mass model for c_+ values 2.285, 2.348, and 2.35 with distinct initial conditions corresponding to increasing values of α of 0.52, 0.97, and 1.13 respectively.⁸ For comparison, numerically obtained spectrum is also included. From the plots we infer that the mass model is successful in generating the isocurvature spectrum within the parametric region of applicability. The model generates a blue power spectrum for small K modes with an approximate spectral index $n_l - 1 \approx 3$. The spectrum peaks at the first bump and subsequently undergoes oscillations that quickly die away. As we shall see later the location of the first bump and the frequency of subsequent spectral oscillations (bumps) is related to the transition time T_c . The discrepancies between the numerical and analytic computations are noticeable for K modes beyond the first bump because during the time these modes exit the horizon, the axion mass is oscillating with a large amplitude in the resonant scenarios. As an example, consider in Fig. 7 the case of $c_+ = 2.35$ for which the discrepancy is the largest for the K region $[5 \times 10^4, 10^5]$.

These discrepancies can be explained through the limitations of ξ modeling and the integrating out approximation. More specifically, we noted in Sec. VB that the

⁸The $c_+ = 2.35$ case has a corresponding $\alpha = 1.128$ which is slightly larger than α_U defined in Eq. (94), but since this is only at the cusp of the approximations breaking down, the agreement with the numerical results are reasonable.

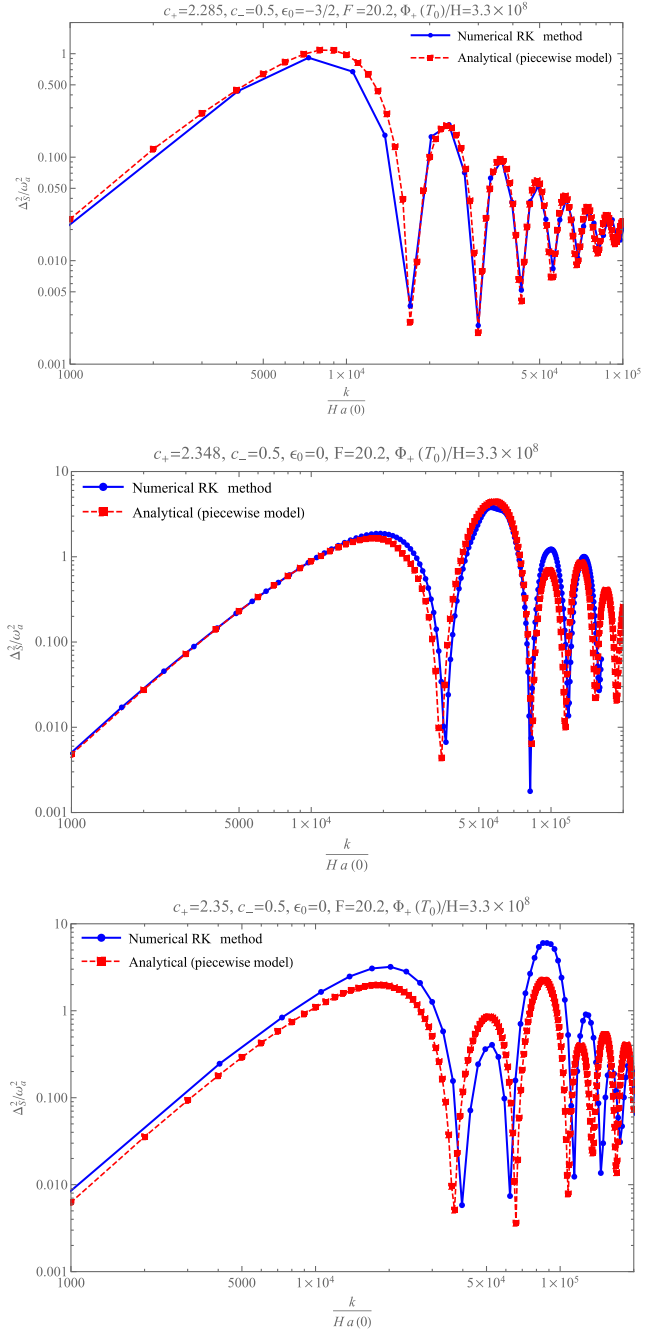


FIG. 7. These plots illustrate the analytic spectrum computed using Eq. (108) for the parameter set P_A used in Fig. 5 except with ε_0 also varied [recall $\varepsilon_0 = -3/2$ corresponds to a dynamically reasonable initial velocity situation of $\dot{\phi}_+(0) = -3\phi_+(0)/2$] as denoted in the title of each plot. They are compared with the Runge-Kutta solution to the mode equation (23). The interesting feature of the second and the third peaks being higher than the first peak will be explained in Sec. VII.

analytic approximation of the ETSP $U(T)$ in Eq. (118) to solve the y_1 -mode function is most critical for these intermediate K modes as long as the modes leave the horizon while the jump ETSP is still significant. The jump

ETSP $V_2 e^{-3(T-T_2)}/2$ is obtained after the UV modes have been integrated out, as shown previously in Fig. 3 and detailed in Appendix H. In the UV integration procedure, we have made the assumption that the flat deviation ξ is purely sinusoidal with a constant amplitude and a slow-varying time-dependent frequency $O(F)$. Post UV integration, we averaged out the remaining slow-varying prefactors to obtain a constant amplitude jump ETSP V_2 (see Appendix H for details). These assumptions along with a pure harmonic approximation can be insufficient to accurately map the sensitivity of the spectrum to subtle variations of the mass eigenvalue for the intermediate modes that leave the horizon around the same time.

One then concludes that background fields with weaker resonance $O(\xi) < \frac{F^2}{2}$ (since that situation will be less sensitive to the limitations of ξ modeling in general) will show a far smaller discrepancy between numerical and analytical spectra for these intermediate modes, as observed for $c_+ = 2.285$. Nonetheless, note that the mass model successfully generates the distinct feature of a larger second bump and a larger third bump than the first for $c_+ = 2.348$ and $c_+ = 2.35$, respectively. We will discuss this more in the next section.

VII. EXPLANATION OF THE FEATURES OF ISOCURVATURE SPECTRUM

We will now give analytic expressions for $y_1(K, T)$ mode functions for a specific class of simplified mass model. This will allow us to explain the parametric dependence of the isocurvature spectrum at different scales and provide closed form analytic expressions for the isocurvature power spectrum in a certain restricted region of the underlying model space.

For the following discussion, we will restrict ourselves to single dip cases corresponding to $\alpha < \alpha_2$. Under this condition, our time-dependent piecewise mass model in Eq. (101) simplifies to the following form:

$$m^2 \approx \begin{cases} V_0, & T_0 < T < T_1, \\ -V_1, & T_1 < T < T_2, \\ V_B \text{sqw}(T, T_2, T_B - T_2) + \frac{V_2}{2} e^{-3(T-T_2)}, & T_2 < T < T_\infty, \end{cases} \quad (183)$$

where the mass model is now limited to a single dip $-V_1$, an exponentially decaying jump ETSP V_2 , and an $O(c_-)$ mass squared term V_B . As explained in Sec. VB, the above mass model is used within the corresponding y_1 differential equation of Eq. (109).

Furthermore, as discussed in Sec. VB, the above differential equation is analytically intractable for certain K modes where the following two terms are of similar orders of magnitude at T_2

$$K^2 e^{-2T_2} e^{-2(T-T_2)}, \quad \frac{V_2}{2} e^{-3(T-T_2)}.$$

To solve this system analytically, we subdivided the time region $[T_2, T_\infty]$ into regions where either one of the aforementioned two terms is dominant over the other.

Hence, in order to obtain a simplified closed form analytic expression for the isocurvature spectrum for $\alpha < \alpha_2$ cases, we will utilize the following approach. As a first step, we will evaluate the isocurvature power spectrum with the V_2 term neglected. This is clearly applicable to all resonance cases where $V_2 < O(c_-)$. This assumption immensely simplifies our model and consequently allows us to obtain tractable analytic expressions. Subsequently, the effect of the V_2 jump ETSP is added in the form of a correction factor $f_{\text{correction}}$. Through this two-step procedure, we give an approximate analytic expression for the isocurvature power spectrum which will allow us to discover some important generic features. If one is only interested in the results, we refer the reader to Eqs. (222) and (223). We will now give details regarding the aforementioned approach.

A. Step 1: $V_2 < O(c_-)$

When $V_2 < O(c_-)$, the mass model simplifies to

$$m^2 \approx \begin{cases} V_0, & T_0 < T < T_1, \\ -V_1, & T_1 < T < T_2, \\ V_B \text{sqw}(T, T_2, T_B - T_2), & T_2 < T < T_\infty. \end{cases} \quad (184)$$

Defining u as

$$y_1 = e^{-\frac{3}{2}T} u, \quad (185)$$

Eq. (109) becomes

$$\partial_T^2 u + (K^2 e^{-2T} + m^2 - 9/4)u = 0, \quad (186)$$

which has an incoming BD normalized solution

$$u(K, T < T_1) \approx \frac{\sqrt{\pi}}{2\sqrt{2}} e^{i(\frac{i\omega\pi}{2} + \frac{\pi}{4})} H_{i\omega}^1(Ke^{-T}) \quad \forall Ke^{-T_0} \gg |\omega|, \quad (187)$$

with $\omega = \sqrt{c_+ - 9/4}$ for $V_0 = c_+$.

For the rest of our discussion, we will use the following asymptotic forms of the Hankel function $H_{i\omega}^1(z)$ for a real argument z :

$$H_{i\omega}^1(z) \approx \begin{cases} \frac{1+i\cot(i\omega\pi)}{\Gamma(i\omega+1)} \left(\frac{z}{2}\right)^{i\omega} - i \frac{\Gamma(i\omega)}{\pi} \left(\frac{z}{2}\right)^{-i\omega}, & 0 < z \ll \sqrt{1+i\omega}, \\ \sqrt{\frac{2}{\pi z}} e^{i(z - \frac{i\omega\pi}{2} - \frac{\pi}{4})}, & z \gg \left| -\omega^2 - \frac{1}{4} \right|. \end{cases} \quad (188)$$

Next we solve within $T_1 < T < T_2$ for a single dip $-V_1$ and express the solution at $T = T_2$ as

$$\begin{aligned} \begin{bmatrix} u \\ \partial_T u \end{bmatrix}_{T=T_2} &= \cosh[-b\Delta T] \begin{bmatrix} 1 & -\frac{\tanh[-b\Delta T]}{b} \\ -b \tanh[-b\Delta T] & 1 \end{bmatrix} \\ &\times \begin{bmatrix} u \\ \partial_T u \end{bmatrix}_{T=T_1}, \end{aligned} \quad (189)$$

with $\Delta T = T_2 - T_1$ and

$$b^2 \equiv V_1 + 9/4 - K^2 e^{-(T_2+T_1)}. \quad (190)$$

Note that Eq. (189) is the simplified result coming from the average value for the $K^2 e^{-2T}$ term within the short interval ΔT , while V_1 containing the initial kinetic energy information generically satisfies

$$V_1 \sim O(F^2) \gg O(10). \quad (191)$$

Next we solve within $[T_2, T_\infty]$. To further simplify our evaluations, we consider that for $V_B \ll 9/4$, the effect of the model parameter V_B can be factored in through the exponential decay of the final mode amplitude. Equivalently, consider the differential equation

$$\partial_T^2 u + (K^2 e^{-2T} + V_B - 9/4)u = 0. \quad (192)$$

Then the mode function $u(T)$ has the following asymptotic solution:

$$\lim_{T \rightarrow T_\infty} u(T, V_B \neq 0) \approx \lim_{T \rightarrow T_\infty} e^{(-\frac{3}{2} + \sqrt{\frac{9}{4} - V_B})(T - \tilde{T})} u(T, V_B = 0), \quad (193)$$

where $u(T, V_B \neq 0)$ is the solution of Eq. (192) with $V_B \neq 0$, while $u(T, V_B = 0)$ is the solution with the V_B term equal to zero. Hence, if we neglect the V_B term and solve for u in terms of Bessel functions of order $3/2$ (similar to a massless axion), we obtain the final mode function as follows:

$$\begin{aligned} \lim_{T_3 \rightarrow T_\infty} \begin{bmatrix} y_1 \\ \partial_T y_1 \end{bmatrix}_{T=T_3} &= \mathfrak{D} \frac{\cosh[-b\Delta T]}{K^{\frac{3}{2}} \sqrt{-K\tau_2}} \begin{bmatrix} \frac{3 \cos[-K\tau_2]}{2} - \left(\frac{3/2}{-K\tau_2} + K\tau_2 \right) \sin[-K\tau_2] & -\cos[-K\tau_2] + \frac{\sin[-K\tau_2]}{-K\tau_2} \\ 0 & 0 \end{bmatrix} \\ &\times \begin{bmatrix} 1 & -\frac{\tanh[-b\Delta T]}{b} \\ -b \tanh[-b\Delta T] & 1 \end{bmatrix} \begin{bmatrix} u \\ \partial_T u \end{bmatrix}_{T=T_1}, \end{aligned} \quad (194)$$

where τ_2 is the conformal time corresponding to the time T_2 [see Eq. (177)] and the factor

$$\mathfrak{D} \equiv e^{(-\frac{3}{2} + \sqrt{\frac{9}{4} - V_B})(T_\infty - \tilde{T})} \quad (195)$$

accounts for the mode amplitude decay (amplification) through a positive (negative) V_B parameter as explained previously. Using the simplified expression in Eq. (194), we examine the axion isocurvature spectrum for our model for different K ranges.

1. Modes that leave the horizon early: $-K\tau_2 \ll 1$

Starting with the above equation, we simplify in terms of $-K\tau_2 \ll 1$,

$$\begin{aligned} \lim_{T_3 \rightarrow T_\infty} \begin{bmatrix} y_1 \\ \partial_T y_1 \end{bmatrix}_{T=T_3} &\approx \mathfrak{D} \frac{\cosh[-b\Delta T]}{K^{\frac{3}{2}} \sqrt{K} e^{-T_2}} \begin{bmatrix} \frac{(K e^{-T_2})^2}{2} & \frac{(K e^{-T_2})^2}{3} \\ 0 & 0 \end{bmatrix} \begin{bmatrix} 1 & -\frac{\tanh[-b\Delta T]}{b} \\ -b \tanh[-b\Delta T] & 1 \end{bmatrix} \begin{bmatrix} u \\ \partial_T u \end{bmatrix}_{T=T_1} \\ &\approx \mathfrak{D} \cosh[-b\Delta T] e^{-\frac{3}{2}T_2} \begin{bmatrix} \frac{1}{2} & \frac{1}{3} \\ 0 & 0 \end{bmatrix} \begin{bmatrix} 1 & -\frac{\tanh[-b\Delta T]}{b} \\ -b \tanh[-b\Delta T] & 1 \end{bmatrix} \begin{bmatrix} u \\ \partial_T u \end{bmatrix}_{T=T_1}, \end{aligned} \quad (196)$$

$$\begin{aligned} \lim_{T \rightarrow T_\infty} y_1(K, T) &\approx e^{-\frac{3}{2}T_2} \mathfrak{D} \cosh[b\Delta T] \frac{\sqrt{\pi}}{2\sqrt{2}} e^{i(\frac{i\omega\pi}{2} + \frac{\pi}{4})} \left[\left(\frac{1}{2} - \frac{b}{3} \tanh[-b\Delta T] \right) H_{i\omega}^1(K e^{-T_1}) \right. \\ &\quad \left. + \left(\frac{1}{3} - \frac{\tanh[-b\Delta T]}{2b} \right) \partial_T H_{i\omega}^1(K e^{-T_1}) \right]. \end{aligned} \quad (197)$$

Since $b^2 \sim V_1 \gg 1$ [(see Eq. (191)], the mode amplitude is dominated by $H_{i\omega}^1(K e^{-T_1})$ rather than its derivative,

$$\lim_{T \rightarrow T_\infty} y_1(K, T) \approx e^{-\frac{3}{2}T_2} \mathfrak{D} \cosh[b\Delta T] \frac{\sqrt{\pi}}{2\sqrt{2}} e^{i(\frac{i\omega\pi}{2} + \frac{\pi}{4})} \left[\left(\frac{1}{2} - \frac{b}{3} \tanh[-b\Delta T] \right) H_{i\omega}^1(K e^{-T_1}) \right], \quad (198)$$

where $\Delta T = T_2 - T_1$. Observe that the mode amplitude is dependent upon the freeze-out Hankel function at $T = T_1$ such that $Ke^{-T_1} \ll 1$. At the outset, the isocurvature spectrum appears to have a blue spectral index $n_I \approx 4$ for these scales. However for $\omega < 1$, the Hankel function has K dependence as given in Eq. (188). We apply this to the Hankel function in our case where $Ke^{-T_1} \ll 1 \leq \sqrt{1+i\omega}$ to yield the following K dependence for the power spectrum:

$$\Delta_s^2(K) \propto K^3 \left| 1 - i \frac{\Gamma(i\omega)\Gamma(i\omega+1)}{\pi(1+i\cot(i\omega\pi))} e^{-2i\omega \ln(\frac{Ke^{-T_1}}{2})} \right|^2. \quad (199)$$

For $\omega < 1$, the term $\frac{\Gamma(i\omega)\Gamma(i\omega+1)}{\pi(1+i\cot(i\omega\pi))} \sim O(1)$, such that the power spectrum has oscillations in the long wavelength region with a log- K dependence. Therefore, one observes deviation of the spectral index from 4 which is sinusoidal in log- K . These deviations decay as $e^{-\pi\sqrt{c_+-9/4}}$ and become insignificant for large c_+ fields or when $\omega > 1$.

2. Scales near the first bump ($-K\tau_1 \rightarrow 1$)

Next we consider K modes that approach $-1/\tau_2$ such that the modes leave the horizon after the axion effective frequency squared undergoes oscillations. We start with Eq. (194) giving us the mode amplitude $y_1(K, T)$:

$$\begin{aligned} \lim_{T \rightarrow T_\infty} y_1(K, T) \approx \Im \frac{\cosh[-b\Delta T]}{K^{\frac{3}{2}}\sqrt{Ke^{-T_2}}} \left[\left(\frac{3}{2} \cos[-K\tau_2] - \left(\frac{3/2}{Ke^{-T_2}} - Ke^{-T_2} \right) \sin[-K\tau_2] \right) \left(u - \frac{\tanh[-b\Delta T]}{b} \partial_T u \right) \right. \\ \left. + \left(-\cos[-K\tau_2] + \frac{1}{Ke^{-T_2}} \sin[-K\tau_2] \right) (-b \tanh[-b\Delta T] u + \partial_T u) \right]. \end{aligned} \quad (200)$$

Since $b^2 \sim V_1 \gg 1$ [Eq. (191)], the mode amplitude simplifies as

$$\begin{aligned} \lim_{T \rightarrow T_\infty} y_1(K, T) \approx \Im \frac{\cosh[b\Delta T]}{K^{\frac{3}{2}}\sqrt{Ke^{-T_2}}} \frac{\sqrt{\pi}}{2\sqrt{2}} e^{i(\frac{i\omega\pi}{2} + \frac{\pi}{4})} \left[\left(\frac{3}{2} + b \tanh[-b\Delta T] \right) \cos[-K\tau_2] \right. \\ \left. - \frac{1}{Ke^{-T_2}} \left(\frac{3}{2} + b \tanh[-b\Delta T] - (Ke^{-T_2})^2 \right) \sin[-K\tau_2] \right] H_{i\omega}^1(Ke^{-T_1}). \end{aligned} \quad (201)$$

Putting this into Eq. (175), we find the isocurvature amplitude to be proportional to

$$\sqrt{\Delta_s^2(K)} \propto \frac{|e^{i(\frac{i\omega\pi}{2} + \frac{\pi}{4})} H_{i\omega}^1(Ke^{-T_1})|}{\sqrt{Ke^{-T_2}}} \left[\left(\frac{3}{2} + b \tanh[-b\Delta T] \right) \cos[-K\tau_2] - \frac{1}{Ke^{-T_2}} \left(\frac{3}{2} + b \tanh[-b\Delta T] - (Ke^{-T_2})^2 \right) \sin[-K\tau_2] \right]. \quad (202)$$

The location of the first bump $K_{\text{first-bump}}$ is determined by solving

$$\frac{d}{dK} \sqrt{\Delta_s^2(K_{\text{first-bump}})} = 0 \quad (203)$$

since one can show that there are no small oscillatory features in the rising part of the spectrum in the region $-K\tau_1 < 1$. To solve for the peak $K_{\text{first-bump}}$, we approximate $T_2 \approx T_1$ since $T_2 - T_1 = \Delta T \sim O(1/F) \ll 1$ to obtain the following transcendental equation for the small $c_+ - 2$ limiting case $Ke^{-T_1} \sim 1 \gg |\omega^2 - \frac{1}{4}|$:

$$\left(1 - \frac{B}{z^2} \right) \cot(z) = \frac{B(z^2 - 2)}{2z^3}, \quad (204)$$

$$\cot z = \frac{2 - z^2}{2z}, \quad (205)$$

where $B = 3/2 + b \tanh[-b\Delta T]$ and $z = Ke^{-T_2}$. Since $B \gg 1$, the solution to the above expression is nearly independent of B or more explicitly the properties such as the amplitude and velocity of the field oscillations after T_c . We obtain the solution of

$$K_{\text{first-bump}} e^{-T_2} = \frac{\pi + \sqrt{\pi^2 - 8}}{2} + O(B^{-1}) \approx 2 \quad (206)$$

analytically by expanding in the limit $B \gg 1$.

Calculations in large $c_+ - 2$ limiting case $Ke^{-T_1} \sim 1 \ll |\sqrt{1+i\omega}|$ yield similar results by solving an analog of Eq. (204):

$$\cot(z) \approx \left(\frac{1}{z} - \frac{2z}{3}\right) + O\left(\frac{1}{B}\right) \quad (207)$$

leading to

$$K_{\text{first-bump}} e^{-T_2} = \frac{1}{16} \left(9\pi - 6 + \sqrt{81\pi^2 - 108\pi - 156}\right) \approx 2.48. \quad (208)$$

Thus, we have shown that the isocurvature power has the first large bump at approximately

$$K_{\text{first-bump}} = \frac{k}{a(0)H} \approx 2e^{T_2} \quad (209)$$

with 25% accuracy. Equation (209) shows that the location of the first bump is the scale that leaves the horizon at time T_2 near the resonant transition time T_c . Since the transition T_c is dependent upon the mass c_+ and the initial conditions

$\phi_+(0)$ and ϵ_0 [see Eq. (74)], background fields with smaller α tend to transition later such that they have a larger T_c . Under these circumstances the corresponding first-bump location $K_{\text{first-bump}}$ will be pushed to even smaller scales and become unobservable due to limitations in the experimental sensitivity of short length scales. This is qualitatively the same as the situation in which $c_+ < 9/4$, which was the subject of previous work on this topic [75].

3. Scales that lie within oscillating spectrum:

$$3 \lesssim -K\tau_2 < K_2$$

Next we consider K modes satisfying $3 \lesssim -K\tau_2 < K_2$ that leave the horizon after the axion effective frequency squared undergoes oscillations. The upper limit for these K modes is set by the heavy-mode coupling as elucidated in Eq. (180). Meanwhile, Eq. (194) gives the mode amplitude $y_1(K, T)$ in the limit $Ke^{-T_1} \gg |\omega^2 - 1/4|$ to be

$$y_1(K, T_\infty) \approx \mathfrak{D} \frac{e^{-iK\tau_1}}{2K^{3/2}} \left[\cosh[-b\Delta T] \left(\left(-ie^{\Delta T/2} - \frac{3e^{-\Delta T/2}}{-2K\tau_2} \right) \cos[-K\tau_2] + \left(-e^{-\Delta T/2} + \frac{ie^{\Delta T/2}}{-K\tau_2} \right) \sin[-K\tau_2] \right) \right. \\ \left. + \sinh[-b\Delta T] \left(\left(\frac{i3e^{\Delta T/2}}{2b} + \frac{be^{-\Delta T/2}}{-K\tau_2} \right) \cos[-K\tau_2] + \left(\frac{-ie^{\Delta T/2}K\tau_2}{b} - \frac{be^{-\Delta T/2}}{K^2\tau_2^2} \right) \sin[-K\tau_2] \right) \right]. \quad (210)$$

Considering that $\Delta T \sim O(1/F) \ll 1$, we can rewrite this expression as

$$\lim_{T \rightarrow T_\infty} y_1(K, T) \approx \mathfrak{D} \frac{e^{-iK\tau_1}}{2K^{3/2}} \left[\cosh[-b\Delta T] (-ie^{iK\tau_2}) + \sinh[-b\Delta T] \left(\left(\frac{b}{-K\tau_2} \right) \cos[-K\tau_2] + \left(i \frac{-K\tau_2}{b} \right) \sin[-K\tau_2] \right) \right]. \quad (211)$$

We notice from the above expression that the spectrum oscillates via the $\cos[-K\tau_2]$ term for the intermediate K modes (scales) about a background with an initial decay envelope proportional to $1/K^2$. The amplitude of these oscillations is controlled by the dip amplitude V_1 operating for a short time interval ΔT [see Eq. (129)], which is largely controlled by the mass squared eigenvalue and eigenvector rotation. Meanwhile, the K spacing of these oscillations is approximately

$$\Delta k \equiv \Delta K a(0)H \approx \pi a(T_2)H \quad (212)$$

$$\approx K_{\text{first-bump}} a(0)H. \quad (213)$$

Therefore, the location of the first bump and the frequency of the first few spectral oscillations is directly related to the transition time T_c of the background fields. This can be understood through the following discussion.

For our simplified model, as the background fields transition, the mass squared m^2 dips to a negative ETSP $-V_1$ for a time period $\Delta T = T_2 - T_1$. For all K modes that are still subhorizon at transition, the incoming mode amplitude picks up a phase that is dependent upon the momentum K of the mode sampled at the transition where

$T_c \approx (T_2 + T_1)/2$. Later when these modes exit the horizon the resulting mode amplitude is oscillatory in K space with a K spacing that is dependent upon the transition time T_c . As a result, the power spectrum for these scales oscillates while the imaginary part of the phase controls the amplitude of these oscillations. In Fig. 8 we plot the isocurvature power spectrum for a representative example highlighting the spectral oscillations.

4. Scales leave the horizon late: $K > K_P$

As remarked near Eq. (181), for the plateau part of the spectrum ($K > K_P$), the isocurvature perturbation modes return to the usual massless form. In this case, it is better to work in the final massless axion basis. Because the axion field a in Eq. (12) is not normalized canonically, the canonically normalized axion is $A = a/\sqrt{2}$. This allows us to write the plateau part of the spectrum as

$$\frac{\Delta_S^2(K)}{\omega_a^2} = 4 \left(\frac{H(t_K)}{2\pi A(t_K)} \right)^2 \quad (214)$$

$$= \frac{2}{\left(\frac{c_-}{c_+}\right)^{1/2} + \left(\frac{c_+}{c_-}\right)^{1/2}} \left(\frac{h}{2\pi\theta_+(0)F} \right)^2, \quad (215)$$

where $K > K_p$ and we have approximated $H(t_K)$ to be constant [neglecting corrections of slow roll parameters $O(\epsilon)$ which are typically negligible in the physical scenarios of interest in this scenario]. The appearance of h in Eq. (215) is merely dividing out the scaling of F_a in Eq. (20). This flat part of the spectrum has also been numerically confirmed.

B. Step 2: Adding correction for the V_2 term

Equation (194) gives the final mode amplitude for axionic isocurvature perturbation for $\alpha < \alpha_2$ cases consisting of a $-V_1$ single dip and a negligible V_2 jump ETSP where the effect of the V_B parameter (average of m_B^2) is included through the exponential decay factor \mathfrak{D}^2 in Eq. (195). Using the expression for V_2 under Eq. (129) and the expression for A from Eq. (173), we infer that for F scales greater than $O(20)$, the amplitude of the resonant UV oscillations is larger than $O(c_-)$ such that the $V_2/2$ term

cannot be neglected. Below we will briefly discuss the corrections coming from V_2 .

Since V_2 is positive, its inclusion in Eq. (101) for the y_1 -mode function leads to a decay of all the modes that are superhorizon at T_2 [see the discussion below Eq. (112)]. Consequently, a significant V_2 leads to a reduction in the isocurvature power spectrum for a range of small K modes. On the other hand, for all modes that are subhorizon at T_2 , the effect is significantly diminished since the ETSP decays exponentially with a decay factor of 3. Another way to understand this correction is to note that a large resonant UV oscillations of the background fields imply a significant interaction energy compared to the mass energy at transition. This increases the effective mass for the perturbation modes, thereby reducing their amplitudes.

We now give approximate analytic expressions to include the effect of the jump ETSP V_2 to the previously derived isocurvature perturbation mode amplitude. The effect of V_2 ETSP is included as

$$f_{\text{correction}}(K) \approx \frac{1+l(K)}{2} + \frac{1-l(K)}{2} \left(\frac{\left(Ke^{-T_2} - \sqrt{\frac{V_2}{2}}\right)}{\sqrt{1 + \left(Ke^{-T_2} - \sqrt{\frac{V_2}{2}}\right)^2}} \right), \quad (216)$$

where

$$l(K) = \left[\left(a_1 + \frac{a_2}{3} + c_- \frac{3a_1 + 2a_2}{27} \right) \frac{2 \sin(\pi n_1) \Gamma(1 - n_1) V_2^{n_1/2} 2^{-n_1/2} 3^{-n_1}}{\pi \left(a_1 \frac{\sqrt{2V_2}}{3} \partial_x J_{n_1}(x) \Big|_{x=\frac{\sqrt{2V_2}}{3}} + (a_1 + 2a_2/3) J_{n_1}\left(\frac{\sqrt{2V_2}}{3}\right) \right)} \right]^{-1}, \quad (217)$$

with $a_{1,2,3}$ defined as

$$a_1 \approx y_1(K, T_2), \quad (218)$$

$$a_2 \approx \partial_T y_1(K, T_2), \quad (219)$$

$$a_3 \approx -a_1 \sqrt{V_2} + a_2. \quad (220)$$

Note that the expression $l(K)$ is primarily derived for all superhorizon modes $Ke^{-T_2} \ll \sqrt{\frac{V_2}{2}}$. Since $l(K)$ must tend to 1 for modes that satisfy $Ke^{-T_2} \gg \sqrt{\frac{V_2}{2}}$, we have constructed $f_{\text{correction}}(K)$ as a smooth function connecting these two asymptotic values of $l(K)$. Hence, the above correction factor is an interpolated approximation for the intermediate modes lying between the two asymptotic scales. An important consequence of this interpolation is that it does not show a gradual shift in the location of the first bump toward smaller K values due to an increasing V_2 jump ETSP, as can be observed in Fig. 9. To accurately

model this gradual shift of the first bump, one needs to evaluate an improved correction factor for the intermediate modes by solving the scattering matrices of Sec. VA with the V_2 jump ETSP included explicitly. Furthermore, we remark that $l(K)$ is nearly a constant since Eqs. (189) and (190) suggest that

$$\frac{\partial_T y_1(K, T_2)}{y_1(K, T_2)} \approx -b \tanh[-b(T_2 - T_1)], \quad (221)$$

which is independent of K for all modes with $Ke^{-T_2} \ll \sqrt{V_1}$ at T_2 .

C. Isocurvature power spectrum

In summary, the isocurvature power spectrum for background fields with $\alpha_L \lesssim \alpha \lesssim \alpha_2$ [where α_L and α_2 are given in Eqs. (93) and (150) respectively] corresponding to a single $-V_1$ dip can be expressed [where α is defined in Eq. (74)] as follows:

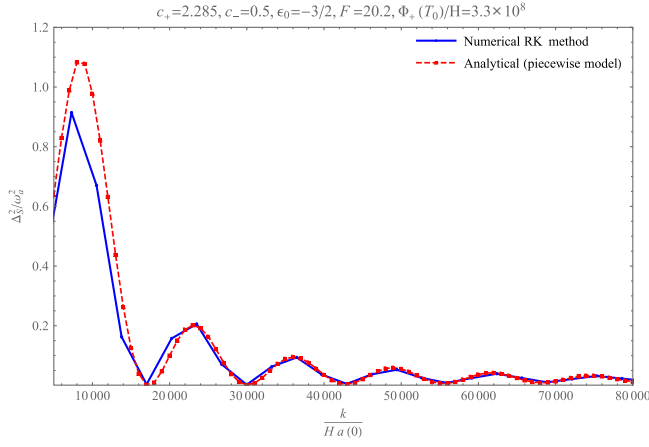


FIG. 8. Plot of the spectra made using Eq. (108) highlighting the analytic form of the spectral oscillations on a linear amplitude scale for k modes for $k/(a(T_c)H) > 2$ (i.e., modes which become superhorizon after the nonadiabatic transition) where $a(T_c)/a(0) = O(10^4)$. The first peak/bump occurs around $k \sim 2a(T_2)H$, where $a(T_2) \approx a(T_c)$. The spectrum oscillates with a k period $\pi e^{T_2}a(0)H$ and the initial decay behavior of the envelope is approximately proportional to k^{-2} . For $k \gtrsim e^{T_2}a(0)H\sqrt{V_1}$ the envelope decay then transitions to k^{-1} behavior, oscillating about a background spectral amplitude of $O(F^{-2})$. Shown are the results with the same parameters set as Fig. 5, except with $\varepsilon_0 = -3/2$ (sizable initial velocity). Note that the height of the first bump is $\sim O(10)$ larger than the height of the final massless axion plateau, which on a linear scale is negligible.

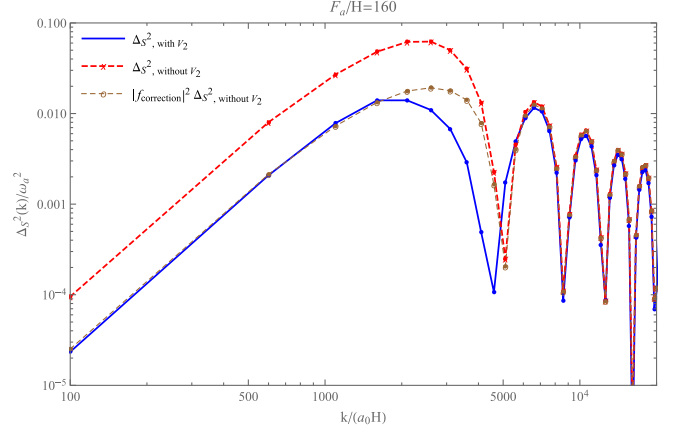


FIG. 9. This figure highlights the effect of jump ETSP V_2 on isocurvature power spectrum derived using the scattering matrices of Eq. (108). The thick (blue) curve corresponds to the actual power spectrum, where modification due to the V_2 parameter has been accounted for. The thick dashed (red) curve neglects the effect due to the V_2 jump ETSP. The thin dashed (brown) curve adds the correction factor in Eq. (216) to the spectrum without the V_2 jump ETSP. A positive jump ETSP V_2 leads to a decay of all modes superhorizon at T_2 . This can result in significant attenuation of spectral power for these modes, as shown in the plots. The above plots are constructed using the following parameter set $\{F = 161.6, c_+ = 2.415, c_- = 0.5, \varepsilon_0 = 0, \phi_+(0) = 0.1M_p/H\}$.

$$\Delta_S^2(K) \approx |f_{\text{correction}}(K)|^2 \times \begin{cases} C_1 K^3 \left| 1 - i \frac{\Gamma(i\omega)\Gamma(i\omega+1)}{\pi(1+i \cot(i\omega\pi))} e^{-2i\omega \ln(\frac{-K\tau_1}{-2})} \right|^2, & -K\tau_c \ll 1, \\ C_2 \mathfrak{D}^2 |H_{i\omega}^1(-K\tau_1)|^2 (-K\tau_2) \left(\sin(-K\tau_2) \right. \\ \left. + (3/2 + b \tanh[-b\Delta T]) \left(\frac{\cos[-K\tau_2]}{-K\tau_2} - \frac{\sin[-K\tau_2]}{(-K\tau_2)^2} \right) \right)^2, & 0.5 \lesssim -K\tau_c < 3, \\ C_3 \mathfrak{D}^2 \cosh^2[b\Delta T] \times \\ \left| (-ie^{iK\tau_2}) + \tanh[-b\Delta T] \times \right. \\ \left. \left(\left(\frac{b}{-K\tau_2} \right) \cos[-K\tau_2] + \left(i \frac{-K\tau_2}{b} \right) \sin[-K\tau_2] \right) \right|^2, & 3 \lesssim -K\tau_c < K_2, \\ C_4 \times 1, & K > K_P, \end{cases} \quad (222)$$

with coefficients $C_{1,2,3,4}$ given as

$$\begin{aligned} C_1 &\approx C \mathfrak{D}^2 \frac{\pi}{8} e^{-\omega\pi} \cosh^2[b\Delta T] \frac{e^{-3T_2}}{3} \left(\frac{3}{2} - b \tanh[-b\Delta T] \right)^2 \left| \frac{1 + i \cot(i\omega\pi)}{\Gamma(i\omega + 1)} \right|^2, \\ C_2 &\approx C \frac{\pi}{8} e^{-\omega\pi} \cosh^2[b\Delta T], \end{aligned} \quad (223)$$

$$C_3 \approx C \frac{1}{4},$$

$$C_4 \approx \omega_a^2 \frac{h^2}{2\pi^2 \theta_+^2 F^2} \left(\frac{r}{1+r^2} \right), \quad (224)$$

where

$$C = \omega_a^2 \frac{4}{\pi^2} \frac{r(1+r^4)}{(1+r^2)^3} \frac{h^2}{\theta_+^2 F^2} \quad (225)$$

for $r = \sqrt{c_+/c_-}$, and

$$\mathfrak{D} \approx \exp\left(\left(-\frac{3}{2} + \sqrt{\frac{9}{4} - V_B}\right)(T_B - \tilde{T})\right), \quad (226)$$

which accounts for the mode amplitude decay through the V_B parameter:

$$V_B \approx c_- + \frac{1}{(T_L - T_2)} \left(\frac{1063}{3072} + \frac{106793c_-}{393216c_+}\right)$$

for parameters \tilde{T} ,

$$\tilde{T} = \max\{T_2, \ln(2K/3)\}, \quad (227)$$

and $T_B = T_L$ given in Eq. (I23) which for $c_- \ll 1$ reduces to

$$T_L \approx T_2 - \left(\frac{3}{c_-}\right) \ln\left(\frac{2 \sin(\pi n_1) 2^{2-n_1} \Gamma(1-n_1) \phi_{-\min}(\frac{A\sqrt{2}}{3\Omega})^{n_1}}{\pi(3\phi_{-s}(T_2) \frac{A\sqrt{2}}{3\Omega} \partial_x J_{n_1}(x)|_{x=\frac{A\sqrt{2}}{3\Omega}} + (3\phi_{-s}(T_2) + 2\dot{\phi}_{-s}(T_2)) J_{n_1}(\frac{A\sqrt{2}}{3\Omega}))}\right), \quad (228)$$

where ϕ_{-s} and its derivative in Eq. (I23) for T_L are given in Eq. (E14), $\bar{\Omega}$ is given in Eq. (E16), and $n_1 = \sqrt{1 - 4c_-/9}$. As noted near Eq. (I81), there is a gap in the analytic spectrum in the region $[K_2, K_p]$. The correction factor $f_{\text{correction}}(K)$ is defined in Eq. (I216).

The coefficients C_n have been defined such as to be approximately scale independent. Since $V_1 \gg 1$, the term $b = \sqrt{V_1 + 9/4 - K^2 e^{2T_c}}$ in $C_{1,2}$ is approximately K independent. Similarly, \mathfrak{D}^2 is independent of K for long wavelengths and hence it is absorbed into C_1 . Meanwhile $-K\tau_c \sim 2$ gives us the approximate location of the first bump. If V_2 is neglected, the \mathfrak{D}^2 term has the following approximate form for $A\sqrt{2}/(3\Omega) \lesssim 1$,

$$\mathfrak{D}^2 \approx e^{\frac{3}{2}(c_-(\tilde{T}-T_2)-\frac{1063}{3072})} \frac{1}{F^2} 16 \sqrt{\frac{c_+}{c_-}} (1 - 4c_-/9) \times \left(\frac{1}{\alpha/2 + 1/5 + 4/F}\right)^2, \quad K \lesssim K_2, \quad (229)$$

where we remark that \mathfrak{D}^2 eventually tends to 1 for extremely small scales that correspond to the massless axion. To evaluate the expressions given in Eqs. (I222) and (I223) into a numerical amplitude, the parameters $\{T_1, T_2, T_c, V_1, \Delta T = T_2 - T_1\}$ can be computed through

$$T_1 \approx T_c - \left(\frac{3.11 - 1.05\alpha}{2F}\right), \quad (230)$$

$$T_2 \approx T_c + \left(\frac{3.11 - 1.05\alpha}{2F}\right), \quad (231)$$

$$T_c \approx T_z - \frac{0.7}{\alpha F}, \quad (232)$$

$$V_1 = |\min(m_1^2 - \dot{e}_1 \cdot \dot{e}_1)|, \quad (233)$$

obtained from Sec. VI A. The definition of T_z can be found in Eq. (I71), and the variables $\tau_{1,2,c}$ are the conformal times corresponding to $T_{1,2,c}$ obtained through Eq. (I177). In turn, to evaluate α in Eq. (I230), use Eqs. (I73) and (I75). To evaluate V_1 of Eq. (I233), put Eqs. (I67) and (I68) into Eqs. (I61) and (I63) and minimize by varying time T .

For cases with $\alpha > \alpha_2$ where a second dip is also significant, the shape of the isocurvature spectrum is modified as the parameter C_3 becomes a K -dependent function. The modes now carry additional phases that are dependent upon the dynamics of the V_3 dip. This situation is similar to the explanation provided in Sec. VI B. These cases are solved using the scattering matrices of Eq. (I108) with the full set of model parameters. Equation (I222) and the more general computational procedure presented in Sec. VI are the main results of this paper.

D. Discussion

By substituting Eqs. (I223) and (I229) into Eq. (I222) we obtain an approximate order of magnitude estimate for the amplitude of the first bump corresponding to $-K_{\text{first-bump}}\tau_2 \sim 2$ for $c_- \ll 1$:

$$\frac{\Delta_S^{2(c_+ > 9/4)}(K_{\text{first-bump}})}{C} \sim O(1)\pi(e^{-\omega\pi}|H_{i\omega}^1(2)|^2)(1 - 4c_-/9) \times \sqrt{\frac{c_+}{c_-}} \frac{V_1}{F^2} \left(\frac{.5}{1/F + .12}\right)^2, \quad (234)$$

where

$$e^{-\omega\pi}|H_{i\omega}^1(2)|^2 \approx 0.31 + O(\omega^2) \quad (235)$$

near $\omega \rightarrow 0^+$ and varies slowly (fractional power of ω) for $\omega \sim O(1)$. The above expression is an approximation

and higher order corrections such as the presence of additional dips (for instance the $-V_3$ dip due to the second crossing after T_c) can lead to a further increase in the amplitude.

Next, we compare the above expression to a corresponding one for the overdamped scenario. In a previous work [77], numerical fitting functions were developed to estimate the isocurvature power spectrum for overdamped cases. It was found that the bump amplitude was maximally approximately a factor of 3 compared to the massless axion plateau. However, those fitting functions were evaluated in a corner of parametric region with $0.5 < c_- < 1$ such that they were largely independent of c_- up to the required accuracy. In order to include the c_- parametric dependence, we note that within the framework of our mass model, the overdamped scenario can be studied by considering a single dip followed by the V_B parameter in Eq. (184). Using the cubic-polynomial expressions in Eqs. (67) and (68), it is easy to show that for the overdamped scenario $V_1 \approx 1.5 \sim O(1)$ and

$\Delta T \sim O(1)$. Using these estimates, we evaluate the amplitude at first bump as

$$\frac{\Delta_S^{2(c_+ < 9/4)}(K_{\text{first-bump}})}{C} \sim O(0.08)\pi \left(\frac{c_+}{c_-}\right)^{0.5}, \quad (236)$$

where it is worth noting that the residual $(c_+/c_-)^{0.5}$ dependence is obtained by fitting the mode amplification due to the slow-varying m_B^2 function. To understand this, note that for the overdamped scenario, the background fields settle to their respective minima along a trajectory where $\phi_{-s} < \phi_{\text{min}}$. Hence, the associated m_B^2 function is negative and can lead to amplification of the mode function (see Appendix I for further details). Also, note that unlike the underdamped scenario, there is no large kinetic energy at transition and thus the absence of any $O(F)$ amplitude enhancing corrections for the overdamped case.

We now compare the isocurvature spectral amplitude between the two cases and obtain

$$\frac{\Delta_S^{2(c_+ > 9/4)}(K_{\text{first-bump}})}{\Delta_S^{2(c_+ < 9/4)}(K_{\text{first-bump}})} \sim O(10)(e^{-\omega\pi}|H_{i\omega}^1(2)|^2)(1 - 4c_-/9) \left(\frac{.5}{1/F + .12}\right)^2 \frac{V_1}{F^2}. \quad (237)$$

For $V_1 > O(10)$, the α dependence is

$$\frac{V_1}{F^2} \sim 0.67\alpha - 0.05 + \frac{1}{F} \quad \forall \alpha \gtrsim 0.1, \quad (238)$$

which is an approximate numerical value [$O(10\%)$ accurate] resulting from evaluating V_1 as explained below Eq. (233). Thus, the ratio of the isocurvature power spectrum between the overdamped ($c_+ < 9/4$) and underdamped ($c_+ > 9/4$) scenarios is approximately

$$\left. \frac{\Delta_S^{2(c_+ > 9/4)}(K)}{\Delta_S^{2(c_+ < 9/4)}(K)} \right|_{K_{\text{first-bump}}} \sim O(10)e^{-\omega\pi}|H_{i\omega}^1(2)|^2 \left(\frac{0.5}{1/F + 0.12}\right)^2 \left(0.67\alpha - 0.05 + \frac{1}{F}\right) \quad \forall \alpha \gtrsim 0.1. \quad (239)$$

At $\alpha \sim 0.1$, the above ratio is approximately $\gtrsim 1$ and hence as $c_+ \rightarrow 9/4$ and $V_1 \rightarrow O(1)$, Eq. (239) tends to unity, giving us a check of the formulas based on the consistency with the results of [77]. Also, Eq. (239) becomes F independent for large F .

Furthermore, the ratio of the amplitude of first bump to the massless axion plateau is

$$\frac{\Delta_S^{2(c_+ > 9/4)}(K_{\text{first-bump}})}{\Delta_S^2(K > K_p)} \approx 8 \frac{r(1+r^4)}{(1+r^2)^2} O(1)\pi e^{-\omega\pi}|H_{i\omega}^1(2)|^2 \frac{V_1}{F^2} \left(\frac{1}{2/F + 0.24}\right)^2. \quad (240)$$

Note that as $c_+ \gg O(10)$, $(e^{-\omega\pi}|H_{i\omega}^1(2)|^2) \sim 1/\omega \sim 1/\sqrt{c_+}$, canceling the r enhancement factor. Therefore the ratio of the bump amplitudes saturates to a constant for large c_+ values. For $c_+ \sim O(1)$ in the resonant case of our interest, Eq. (233) can be approximated as

$$\frac{\Delta_S^{2(c_+ > 9/4)}(K_{\text{first-bump}})}{\Delta_S^2(K > K_p)} \approx O(30)\alpha \left(\frac{4/3}{8/F + 1}\right)^2, \quad (241)$$

which shows how the underdamped scenarios enhance the bump amplitude. This large $O(30)$ number ultimately can be traced to the combination of two coincident effects: (a) enhancement of the kinetic energy due to a time phase accident in the context of oscillatory background solutions which exists only in the underdamped cases, and (b) ξ -involving interaction energy dominating the mass energy. For instance, consider the ratio of the kinetic energy (KE) to the net potential energy (mass + interaction energy

$ME + IE$) at transition for the two cases. Using Eq. (89), we can approximate this ratio for $\alpha > \alpha_L$ for the resonant underdamped case as follows:

$$\left(\frac{KE}{ME + IE}\right)_{c_+ > 9/4} = \frac{\dot{\phi}_+^2 + \dot{\phi}_-^2}{\xi^2 + c_+ \phi_+^2 + c_- \phi_-^2} \quad (242)$$

$$\sim \frac{\alpha^2 F^4}{F^4((1-0.2\alpha)^2 - 1)^2 + O(F^2)} \quad (243)$$

$$\sim O(8), \quad (244)$$

where we note that for underdamped resonant cases, the interaction energy ξ^2 is $O(F^4)$. Remarkably, the parametric dependences have canceled out in Eq. (244).

A similar evaluation for the overdamped situation where the interaction energy ξ^2 is $O(1)$ yields

$$\left(\frac{KE}{IE + ME}\right)_{c_+ \lesssim 9/4} = \frac{\dot{\phi}_+^2 + \dot{\phi}_-^2}{\xi^2 + c_+ \phi_+^2 + c_- \phi_-^2} \quad (245)$$

$$\sim \frac{F^2}{9/4F^2} \quad (246)$$

$$\sim O(0.5), \quad (247)$$

where we note ξ being insignificant in both the numerator and the denominator. Thus, we observe an approximate $O(10)$ enhancement in the spectral power for the underdamped cases compared to those of the overdamped. Since, the first bump in overdamped cases is maximally approximately a factor of 3 compared to the massless axion plateau, we obtain an effective enhancement factor of $O(30)$ for the underdamped scenario as observed in Eq. (241).

As highlighted previously in Sec. VII B, a large V_2 jump ETSP leads to an attenuation of spectral power for all modes superhorizon at T_2 while having a decreasingly small effect on the subhorizon modes. An interesting consequence of this is that for large enough V_2 , the amplitude of a subsequent bump (second or higher) can appear much greater than the first bump. This can be understood as follows. From Eq. (222), we infer that the amplitude of the spectral bumps (oscillations) in the absence of the V_2 jump ETSP can be expressed as

$$\Delta_{S, V_2=0}^2(K) \approx \mathcal{A}_0 \left(\frac{K_{\text{first-bump}}}{K}\right)^2 \quad \forall K_{\text{first-bump}} \leq K \lesssim \tau_c^{-1} \sqrt{V_1}, \quad (248)$$

where \mathcal{A}_0 is the amplitude of the first bump and is independent of V_2 .

With the inclusion of V_2 , the spectral power for all superhorizon modes at T_2 is attenuated due to a V_2 -dependent correction factor $|f_{\text{correction}}| < 1$ as shown in

Sec. VII B. For $V_2 \gg 1$, the corrected spectral amplitude of the first bump can be written as

$$\Delta_{S, V_2 \gg 1}^2(K_{\text{first-bump}}) \approx |f_{\text{correction}}(K_{\text{first-bump}})|^2 \mathcal{A}_0, \quad (249)$$

where the K dependence of $f_{\text{correction}}$ is approximately a constant for all superhorizon modes. On the other hand, the spectral power in Eq. (222) for the subhorizon modes have the property $|f_{\text{correction}}(K)| \sim 1$:

$$\Delta_{S, V_2 \gg 1}^2(K) \approx |f_{\text{correction}}(K)|^2 \mathcal{A}_0 \left(\frac{K_{\text{first-bump}}}{K}\right)^2 \quad \forall K_V \lesssim K \lesssim \tau_c^{-1} \sqrt{V_1}, \quad (250)$$

where $K_V \equiv \tau_c^{-1} \sqrt{V_2}$ and defines the mode when the $|f_{\text{correction}}(K)| \sim 1$. The $|f_{\text{correction}}(K)|$ smoothly interpolates between 1 and $|f_{\text{correction}}(K_{\text{first-bump}})|$ in the spectral region $[K_{\text{first-bump}}, K_V]$.

Comparing Eqs. (249) and (250), we conclude that it is possible for certain high K modes to have a larger spectral power than the first bump. Quantitatively, this is true for the following approximate range of K modes

$$K_V \lesssim K \lesssim \left| \frac{K_{\text{first-bump}}}{f_{\text{correction}}(K_{\text{first-bump}})} \right| \equiv K_f. \quad (251)$$

This is generically observed as a larger second or third bump than the first [see Eq. (222)]. The amount of this relative enhancement can be evaluated as

$$\frac{\Delta_S^2(K)}{\Delta_S^2(K_{\text{first-bump}})} \sim O(V_2^{1/2}) \left(\frac{K_V}{K}\right)^2 \quad \forall K_V \lesssim K \lesssim K_f, \quad (252)$$

where the factor of $V_2^{-3/2}$ comes from $|f_{\text{correction}}(K)|^2 \approx |l(K)|^2$ in Eq. (217) for $V_2 \gg 1$. Hence, the enhancement is approximately proportional to $\sqrt{V_2}$ and increases with the F scale. Thus, we remark that large $O(F^2)$ resonant effects, together with any additional dips ($-V_i$ for $i \geq 3$) corresponding to higher order corrections, can result in spectral power enhancement by a factor greater than the $O(30)$ as derived previously for the resonant underdamped cases. Unlike the $O(30)$ factor whose origin was discussed in Eq. (244), this high K mode enhancement is dependent on the parameter F .

VIII. PARAMETRIC DEPENDENCES OF THE ISOCURVATURE SPECTRUM

One qualitative predictability difference between the overdamped and underdamped axionic scenarios where the PQ symmetry is broken before the end of inflation stems from the fact that there is an attractor solution for the background fields as well as for the linear perturbations in

the overdamped scenarios. This means that given a Lagrangian in overdamped scenarios, the cosmological predictions have less dependence on the initial conditions. As an analogy, in the case of slow roll single field inflation, one only needs to specify the initial field value and not its time derivative to specify a prediction for the observables. For the usual cosmological axion scenarios, the radial field associated with PQ symmetry breaking is considered to be sitting at the minimum of its potential. This means that the only initial condition dependence of the axion isocurvature during inflation is θ_{if_a} . In the case of the current underdamped scenario of interest, there is an additional phase space dependence of the PQ symmetry-breaking radial field directions as well. Because of the nonattractor behavior for the underdamped dynamics along the flat direction, the dominant additional phase space degree of freedom is the initial field $\phi_+(0)$ value and the kinetic energy of the radial field along the flat direction parametrized by ϵ_0 .

In this section we will study the dependence of the axion isocurvature spectrum on the model parameters $\{c_+, c_-, F\}$ and the initial conditions $\{\epsilon_0, \phi_+(0)\}$. The effect of each parameter variation is discussed keeping all of the others fixed.

A. c_+

The numerical model presented in this paper and the associated axion isocurvature spectrum have been derived for background fields within the parametric region given by $\alpha_L \lesssim \alpha \lesssim \min(\alpha_3, \alpha_U)$. Above the upper bound α_U , the analytic methods utilized in this paper break down due to the significant heavy-mode mixing from Eq. (48) at T_c , and at around the same upper bound, the adiabatic approximation technique also breaks down.⁹ For α less than the lower bound, the cubic-polynomial expansion of the background fields is insufficient and higher order terms become significant. The parameter α can be computed as a function of underlying Lagrangian model parameters and the initial conditions from Eq. (73).

In Fig. 10 we plot the c_+ dependence of α within the range of Eq. (95) close to $c_+ = 9/4$ corresponding to the range of c_+ values where T_c is close to (but before) the first zero crossing of the $\phi_+^{(0)}$ field.¹⁰ The monotonic increase in α is captured through the following expression:

⁹Beyond $\alpha > \alpha_3$, the background fields will cross at least twice after transition. For large F , these crossings can occur close enough such that effective heavy mixing from the superposition of each crossing becomes significant. Moreover, as $\alpha \rightarrow 1$, the background field dynamics turns highly chaotic after transition and a closed form prediction of the mode amplitude in terms of α is not feasible. Field configurations with large c_+ tend to fall under this category. These configurations associated with $\alpha \gtrsim 1$ and the accompanying isocurvature spectrum are a subject of interest and will be explored in a separate companion paper [80].

¹⁰Recall $\phi_+(T)$ is approximately equal to $\phi_+^{(0)}(T)$ before T_c .

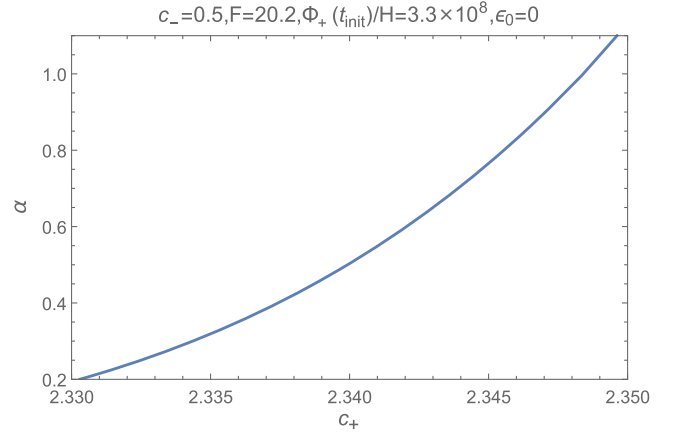


FIG. 10. Plot Eq. (74) showing regions of c_+ with corresponding value of α within the range of Eq. (95). The other parameters are set to the fiducial set P_A of Fig. 5.

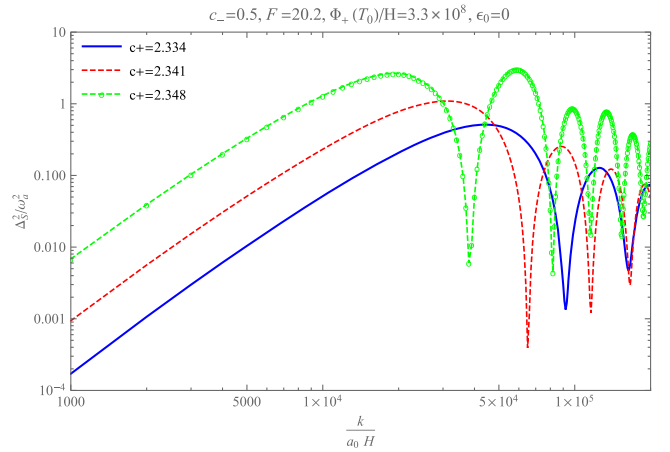


FIG. 11. Plot of spectra made using Eq. (108) for increasing values of c_+ at transition. Note that other parameters are set at the fiducial parameter set P_A used in Fig. 5.

$$\alpha \propto \exp\left(-\frac{3}{2} \left[\frac{\pi}{\sqrt{c_+ - 9/4}} \right]\right). \quad (253)$$

Next, in Fig. 11, we present isocurvature spectra for three different c_+ values. We remark that as c_+ is increased, the $\phi_+^{(0)}$ field rolls down faster¹¹ owing to the frequency $\omega = \sqrt{c_+ - 9/4}$. Consequently, the first zero crossing of the $\phi_+^{(0)}$ field occurs earlier with an increasing c_+ [see Eq. (71)]. This in turn increases the $\exp(-3T_c/2)$ factor controlling ϕ_+ leading to a larger kinetic energy at T_c . The larger kinetic energy is later converted into the interaction

¹¹The exact dependence of the velocity on ω is dependent on whether the system is in the resonant, nonresonant, overdamped, underdamped situations. Here, we will here be focusing only on the resonant cases, which is the main focus of our work.

energy at transition whose larger value is responsible for the growth of the isocurvature amplitude through the resonant effects. Hence, increasing c_+ results in an amplification of first bump in the isocurvature spectrum¹². Moreover, an increasing height of the isocurvature spectrum is accompanied by a receding location of the first bump $K_{\text{first-bump}}$ toward lower values. This is again explained by decreasing T_c as c_+ is increased because Eq. (209) implies

$$K_{\text{first-bump}} \approx O(1)e^{T_c}. \quad (254)$$

When one compares the first-bump amplitude to the plateau amplitude in the $c_+ = 2.348$ case of Fig. 11, one sees that the ratio can be about 30. This is already explained in Eq. (241) of Sec. VII D, where we evaluated an enhancement factor of

$$O(30)\alpha \left(\frac{4/3}{8/F + 1} \right)^2 \quad (255)$$

for modes lying within the range $0.5 \lesssim -K\tau_c < 3$ compared to the modes in the massless axion plateau region of the spectrum ($K > K_p$).

To understand this qualitatively, one first notes that there is the possibility in the underdamped scenarios of a large kinetic energy in the falling ϕ_+ when the ϕ_- interaction with ϕ_+ becomes strong. This large kinetic energy leads to nonadiabatic effects post T_c such that the axion mode amplitude obtains an $O(10)$ enhancement compared to an overdamped scenario.

Note in Fig. 11 that the frequency of the K -space oscillations also increase with c_+ . This has already been explained quantitatively in Eq. (213). To understand this another way qualitatively, note that the temporarily negative lightest mass squared eigenvalue and the nonadiabatic rotation of the lightest eigenvector pump the mode amplitude thereby increasing its magnitude [See Eq. (26)]. Therefore, the k -space oscillation frequency is reflective of the non-adiabaticity producing mode dynamics at time $\sim T_c$, where the modes have the characteristic phase $\exp(-ik \exp(-T_c))$, giving a k -space oscillation period of $O(\exp(T_c))$, as can be seen explicitly in Eq. (213).

The examples presented in this paper are limited to a range of c_+ values where the transition occurs close to the first zero crossing. One might then worry that the mass model is no longer applicable for higher c_+ values because according to Fig. 10, the α value naively seems to increase to violate the approximation methods used. However, as we will discuss in a separate paper [80], α is a discontinuous function of c_+ . As we will show there, the present mass model is still applicable for a range of larger c_+ values (although the c_+ regions where the model is applicable are not continuously connected).

¹²See below regarding how much one can increase c_+ .

B. F

The F dependence of the isocurvature spectrum is multifaceted. The C term in Eq. (225), which is mostly about the normalization of the axion field, suggests a $1/F^2$ proportionality of the power spectrum. This is an expected result since the time-dependent massive axion isocurvature spectrum has a $1/\phi_+^2$ dependence within the long wavelength region (as well as in both the plateau regions). Thus, the variation of the power spectrum in the massless plateau region has a $1/F^2$ proportionality similar to the overdamped scenario.

For scales that lie within the oscillating part of the spectrum, additional F dependences arise from the \mathfrak{D}^2 and b^2 terms of Eq. (222). As shown in Sec. VII D, the spectrum in this region has the following proportionality:

$$\frac{\Delta_S^2(K)}{C} \propto \frac{V_1}{F^2} \left(\frac{.5}{1/F + .12} \right)^2. \quad (256)$$

Using the analytic expressions derived previously, the ratio V_1/F^2 has the following polynomial form within the parametric region given by Eq. (95),

$$\frac{V_1}{F^2} \approx c_1 + c_2\alpha, \quad (257)$$

where $c_1 \sim O(0.1)$ and $c_2 \sim O(1)$. With all other parameters fixed, we have the relationship $\alpha \propto 1/F^2$. Including the C term, the power spectrum has the following effective F dependence in the oscillating region:

$$\frac{\Delta_S^2(K)}{\omega_a^2} \sim \left(\frac{c_1}{F^2} + \frac{c_3}{F^4} \right) \left(\frac{.5F}{1 + .12F} \right)^2, \quad (258)$$

where

$$c_3 = \omega\phi_+(0) \sec \varphi e^{-3/2T_c} \gg c_1. \quad (259)$$

As F becomes large, the power spectrum tends to the expected $1/F^2$ proportionality. One can understand this by noting that for all other parameters fixed, an increase in F results in a rapid reduction in α such that $c_2\alpha$ can subsequently become smaller than c_1 . This is an interesting behavior which can be explained more clearly by noting that for resonant underdamped fields, T_c occurs close to the $\phi_+^{(0)}$ zero crossing:

$$\dot{\phi}_+(T_c) \approx \dot{\phi}_+^{(0)}(T_c) - \int_{T_s}^{T_c} dT \xi \phi_-. \quad (260)$$

At T_c , the ϕ_- field is $O(F)$ and the strong coupling force $\xi\phi_- < 0$ and $\dot{\phi}_+(T_c) < 0$ resulting in $|\dot{\phi}_+(T_c)| < |\dot{\phi}_+(T_s)|$. Using Eq. (72) and $V_1 \sim |\dot{\phi}_+(T_c)|$, we deduce that the c_2 parameter in Eq. (257) is associated with $|\dot{\phi}_+^{(0)}(T_c)| = \alpha F^2$,

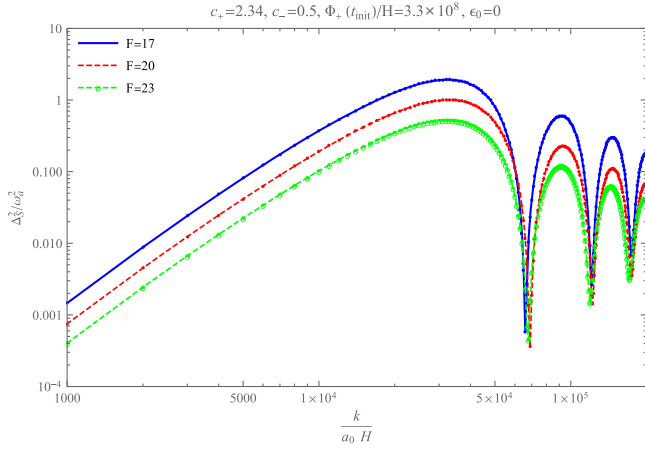


FIG. 12. Illustrated is how the spectra [made using Eq. (108)] varies as F increases. The other parameters are fixed at approximately the set P_A as in Fig. 5. The value of α in this plot varies as $\{0.38, 0.51, 0.71\}$ as F is reduced.

whereas c_1 is related to the integral of the coupling term $\xi\phi_-$. Figure 12 shows plots of power spectra for a fixed c_+ value with different F scales highlighting a $\sim 1/F^n$ reduction of the power spectrum for $n \sim 3 - 4$.

C. c_-

Next we consider the c_- dependence of the power spectrum. We will consider two situations here. In the first, we discuss fields with $\alpha \lesssim \alpha_2$ such that the fields evolve after the transition without any crossings. This situation gives rise to a slowly varying $m_B^2 > 0$. The second case is where the fields have large resonant amplitude such that the fields cross each other at least once after T_c . As explained in Appendix I, such a crossing results in a situation where the ϕ_- field settles to its minimum from below ($\phi_- < \phi_{-\min}$). Due to this unique alignment, the m_B^2 function now becomes negative as the fields settle to their minima asymptotically. In both cases we shall see that the spectrum increases for smaller c_- values with the essential dynamics dictated by the settling of m_B^2 during different temporal phases. The discussion is limited to $c_- < 9/4$.

Let us now consider the first case. The m_B^2 function results in an approximate exponential decay of the mode amplitude through the

$$y_1(T_\infty) \propto \exp\left(-\frac{1}{3} \int_{\bar{T}}^{T_\infty} m_B^2 dT\right) \quad (261)$$

factor where the integral is evaluated through Eq. (I30). The integral can be divided into two temporal phases. During the first phase, the dominant ϕ_- field rolls down from its peak amplitude with a decay constant equal to $c_-/3$. Later as the fields get closer to their minima during the second phase, the decay constant increases by nearly a factor of 4 to $\approx 4c_-c_+/(c_- + c_+)$. Since m_B^2 starts out close to c_- and

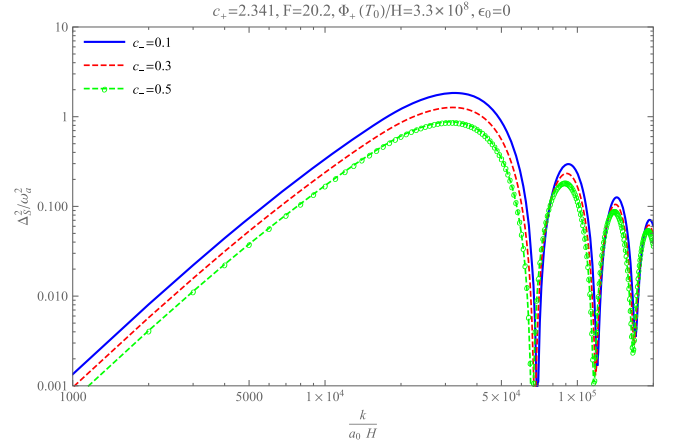


FIG. 13. This plot shows the c_- dependence of the spectra. The other parameters are fixed at approximately the set P_A as in Fig. 5.

eventually settles to zero, the integral is dominated by the first phase. In this first phase, m_B^2 behaves as the flat direction mass which decreases with a decrease in c_- , resulting in $y_1(T_\infty) \propto (c_+/c_-)^{1/4}$: i.e., a smaller c_- results in a larger effective mode amplitude.

In the second case, the ϕ_- field approaches its minimum from below. Unlike the previous case, the first temporal phase is insignificant due to the oscillating IR fields and a dominant V_2 ETSP. Hence, the effective mode amplification due to the negative m_B^2 is brought about during the second phase through Eq. (261). As c_- decreases, m_B^2 decreases much more slowly due to the $\sim 4c_-/3$ exponential decay rate of ϕ_- . Moreover, a smaller c_- results in a larger value of $|m_B^2|$. As a result of these two effects, we see from Eq. (261) that the mode function undergoes larger amplification. This is shown in Fig. 13.

D. ϵ_0 and $\phi_+(0)$

Here we discuss the parameters ϵ_0 and $\phi_+(0)$ that define the initial conditions for the underdamped rolling fields. Varying these initial conditions directly alters T_c and the value of α . Hence, the effect of these two parameters is best understood by studying the α expression from Eq. (74). We consider the minimal case with $\epsilon_0 = 0$ and expand α to quadratic order in ϵ_0 in Eq. (74):

$$\alpha \approx \frac{\phi_+(0)}{F^2} \sqrt{c_+} e^{-\frac{3}{2} \left[\frac{1}{\sqrt{c_+ - 9/4}} \left(\frac{\pi}{2} + \arctan \frac{3/2}{\sqrt{c_+ - 9/4}} \right) \right]} \left(1 + \frac{\epsilon_0^2}{2c_+} \right) + O(\epsilon_0^3). \quad (262)$$

We discover that α has a local minimum at $\epsilon_0 = 0$ evinced by the absence of the linear term in ϵ_0 . This is expected since an increase in the initial kinetic energy leads to a larger $\dot{\phi}_+$ at the zero crossing. As seen in Fig. 14, the dependence of α on ϵ_0 in Eq. (74) is nonlinear beyond the

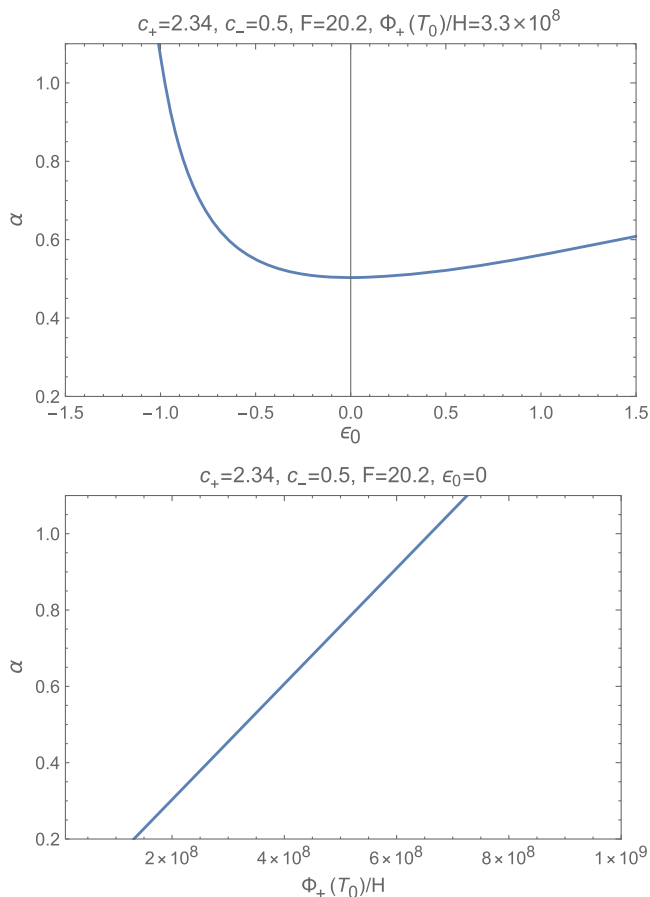


FIG. 14. Plots highlighting the dependence of α on the initial conditions [see Eq. (74)]. Keeping all other parameters fixed, a larger initial energy density results in a larger isocurvature amplitude of the initial bump.

quadratic nonlinearities in Eq. (262). As seen in Eq. (262), the parameter $\phi_+(0)$ leads to a monotonic increase in the value of α within the range of Eq. (95) with the intuition that the initial energy is increased as in the intuition for the ϵ_0 increase. A representative set of α values as a function of $\phi_+(0)$ is shown in Fig. 14.

As $|\epsilon_0|$ is continually increased, T_c becomes nearer to the next higher $\phi_+^{(0)}(T)$ zero-crossing time, thereby reducing the overall spectral power. Similarly, if $\phi_+(0)$ is continually increased then the transition time T_c moves to the next higher zero-crossing time. The subsequent height of the power spectrum can be analyzed by evaluating the value of α at the new transition. Due to the length of this paper and the natural parametric scope of small c_+ in this paper, we discuss the isocurvature spectra reflecting the higher zero crossing of $\phi_+^{(0)}$ in a separate companion paper [80].

IX. SUMMARY

In this paper, we provided an analytic expression for the blue axionic isocurvature spectrum in the underdamped

nonequilibrium axion scenarios for a particular parametric region corresponding to a mild amplitude ($\alpha \in [\alpha_L, \alpha_2]$) of resonantly oscillating PQ symmetry-breaking radial fields. The main expression given by Eq. (222) exhibits an amplitude of Eq. (223) and an oscillating spectrum whose k -space oscillation period is of the order the value of the first k -break location $K_{\text{first-bump}}$ in the spectrum [Eq. (209)]. Remarkably, the first-bump amplitude of the spectrum is enhanced by a factor of $O(30)$ compared to the plateau amplitude of the spectrum associated with the massless axions as explained near Eq. (244). Furthermore, in some cases with large $O(F^2)$ resonant effects, the spectral power can receive larger than the $O(30)$ enhancement of the first peak as explained near Eq. (252).¹³ In contrast, for the overdamped nonequilibrium axion scenarios (see [75]), the relative amplitude ratio is only a factor of a few (maximally approximately a factor of 3). The k -oscillation spacing is reflective of the mode amplitude-setting dynamics at time $\sim T_c$ whose phase is $\exp(-ik \exp(-T_c))$, giving a k -space oscillation period of $O(\exp(T_c))$.

Technically, the computation was carried out using a combination of a parametric restriction where the heavy modes are decoupled (Appendix J), perturbation theory (Sec. IV A), analytic fitting to polynomials in the non-perturbative region (Sec. IV B), piecewise ETSP modeling [Eq. (101)], and the technique of integrating out fast oscillations (Appendix C). This allowed us to compute a transfer matrix solution to the isocurvature mode equations [Eq. (108)]. Overall, based on comparisons to sample numerical calculations, the accuracy of the computation is about 20%–50%, with r_a set to 0.2. Most of the uncertainty is coming from the technique of integrating out the fast oscillations (for example, estimation of V_2) and the approximations made regarding the IR components of the ϕ_{\pm} fields after the transition at T_c . Even though the analytic formula is complicated, compared to the pure numerical solver, the speedup factor¹⁴ is about $O(100)$.

In this paper, we focused on presenting analytic spectral results in the resonant oscillatory k range for moderate α values, where α characterizes the velocity of the falling ϕ_+ field near the transition time T_c [see Eq. (72)]. This would be helpful even if a purely numerical approach to the problem were to be used in data fitting since this will serve as a solvable check on the system. In a companion paper [80], we will present results for larger α situations in the high c_+ limit to complete the understanding of the possibly observable blue isocurvature spectra. In such cases, there are no purely analytic results, but there will appear a novel stochastic model that parametrizes the small k range

¹³Here we have scaled the PQ symmetry-breaking parameter F_a as $F \equiv hF_a/H$, where h is a quartic coupling and H is the Hubble expansion rate during inflation.

¹⁴A *Mathematica* package to evaluate the spectrum using the analytic methods can be accessed from <https://pages.physics.wisc.edu/~stadepalli/Blue-Axion-IsoCurvSpec-Underdamped.nb>.

amplitude variation with α . In that paper, we will also exploit various symmetries to obtain relationships between parameters, which is useful more as a transferable technique than quantitative predictions. Finally, we will also defer to that paper a discussion of general fitting functions for this underdamped blue axionic isocurvature class of models that do not refer to underlying Lagrangian parameters $\{c_{\pm}, F\}$.

There are many interesting possible follow-up topics to be investigated. Recent Planck results [76] show that axionlike curvaton models with an uncorrelated blue-tilted spectrum is the most favored of the isocurvature models. The fits also indicate a possibility of measuring a spectral index of $1.55 < n_I < 3.67$ at 95% C.L. consistently with the recent findings of [77]. It would be interesting to study whether there are hints of resonant isocurvature spectra presented in this paper in the existing and future data. Another possible usage of this enhanced oscillatory peaks presented in this paper would be to investigate the formation of primordial black holes similar to the investigation of the curvaton models in [6,81–89]. Similarly it is equally appealing to study second order gravitational waves and non-Gaussianities through either a QCD axion or a curvaton isocurvature mode as in [58,73,81,82,85,90–94].

ACKNOWLEDGMENTS

This work was supported in part by the Ray MacDonald Fund at University of Wisconsin–Madison. We also thank Amol Upadhye for preliminary investigations into this problem.

APPENDIX A: TAYLOR EXPANSION CONSISTENCY CHECK

In Sec. IV B, we gave a solution to T_1 using an analytic fit to the cubic polynomial, utilizing the information from the differential equation and perturbative solution. In this

section, as a check, we give an alternate derivation of T_1 assuming $T_1 = T_c$, where T_c satisfies

$$\phi_+(T_c) = \phi_-(T_c) = rF, \quad (\text{A1})$$

where

$$0.1 \ll r < 1. \quad (\text{A2})$$

We restrict ourselves to solving the case of the resonant case (see Sec. IV C) in which

$$\cos[\omega T_c - \varphi] \ll 1 \quad (\text{A3})$$

[see Eq. (58) for the definition of φ and Eq. (31) for the initial conditions on ϕ_{\pm}]. The reason why we dwell on the accuracy of the value of T_c is because the numerical results in the resonant situations are very sensitive to the value of T_c due to the large $\dot{\phi}_+(T_c) \sim O(F^2) \gg H\phi_+(T_c) \sim HF$ and the fact that the complex mode amplitude is sensitive to the time phase of the real background field $\phi_+(T)$. The solution method presented here involves a combination of perturbation theory, Taylor expansion, and successive linearization approximations. The most difficult aspect of the computation is in estimating the errors associated with the approximation, and it is this feature that the present section's approach is an advantage over that of Sec. IV B. However, the formalism here is cumbersome compared to that of Sec. IV B, and the differential equation solution for $\xi = (\phi_+\phi_- - F^2)$ used below has limited parametric applicability. The results nonetheless serve as a check on Sec. IV B and provides an error estimate.

Since the computation is long, we first give the results:

$$T_c = T_z - \Upsilon F^{-1}, \quad (\text{A4})$$

$$\Upsilon \approx \Upsilon_1 + \Upsilon_2 \lesssim 1, \quad (\text{A5})$$

$$\Upsilon_1 \equiv -\frac{j_1 \times (3 \frac{F^4}{\phi_+(0)^2} e^{3T_z} (8F^2 + 8Fj_1 + 3j_1^2) \cos^2(\varphi) + j_1^4 \omega^2 (4\omega^2 - 9) e^{\frac{3j_1}{F}})}{j_1^2 \omega^2 e^{\frac{3j_1}{F}} (-8F^2 + 12Fj_1 + j_1^2 (4\omega^2 - 9)) - \frac{1}{\phi_+(0)^2} \Upsilon_{212}}, \quad (\text{A6})$$

$$\Upsilon_2 \equiv \frac{\Upsilon_{21} - \frac{\Upsilon_{221}(\Upsilon_{2221} + \Upsilon_{2222} + \Upsilon_{2223})}{\Upsilon_{223}}}{\frac{\Upsilon_{231}(\Upsilon_{2321} + \Upsilon_{2322} + \Upsilon_{2323})}{\Upsilon_{233}} + \Upsilon_{24}}, \quad (\text{A7})$$

$$\Upsilon_{21} \equiv -\frac{3e^{\frac{3j_1}{F}} F j_1 \omega \Upsilon_{211} \phi_+(0) \cos(\varphi)}{4(\Upsilon_{212} + e^{\frac{3j_1}{F}} j_1^2 \phi_+^2(0) \omega^2 (8F^2 - 12j_1 F + j_1^2 (9 - 4\omega^2)))}, \quad (\text{A8})$$

$$\Upsilon_{211} \equiv (32F^4 - 16j_1 F^3 + 24j_1^2 (3 - 2\omega^2) F^2 - 8j_1^3 (5\omega^2 - 9) F + 3j_1^4 (9 - 4\omega^2)), \quad (\text{A9})$$

$$\Upsilon_{212} \equiv 3e^{3T_z} (16F^2 + 12j_1 F + 3j_1^2) \cos^2(\varphi) F^4, \quad (\text{A10})$$

$$\Upsilon_{221} \equiv \cos(\varphi) \left(\Upsilon_{2211} + e^{\frac{3j_1}{F}} j_1^2 \phi_+^2(0) \omega^2 (8F^2 - 12j_1 F + j_1^2 (9 - 4\omega^2)) \right), \quad (\text{A11})$$

$$\Upsilon_{2211} \equiv 3e^{3T_z} (16F^2 + 12j_1 F + 3j_1^2) \cos^2(\varphi) F^4, \quad (\text{A12})$$

$$\Upsilon_{2221} \equiv 9e^{6T_z} (8F^2 + 8j_1 F + 3j_1^2)^2 (38F^2 + 30j_1 F + 9j_1^2) \cos^4(\varphi) F^6, \quad (\text{A13})$$

$$\begin{aligned} \Upsilon_{2222} \equiv & 6e^{3(\frac{j_1}{F} + T_z)} j_1^2 \phi_+^2(0) \omega^2 \cos^2(\varphi) F^3 (960F^5 + 384j_1 F^4 - 16j_1^2 (14\omega^2 + 45) F^3 \\ & - 8j_1^3 (40\omega^2 + 117) F^2 - 24j_1^4 (7\omega^2 + 18) F - 9j_1^5 (4\omega^2 + 9)), \end{aligned} \quad (\text{A14})$$

$$\Upsilon_{2223} \equiv 2e^{\frac{6j_1}{F}} j_1^4 \phi_+^4(0) \omega^4 (192F^4 - 384j_1 F^3 - 48j_1^2 (2\omega^2 - 3) F^2 + 96j_1^3 \omega^2 F + j_1^4 (16\omega^4 + 81)), \quad (\text{A15})$$

$$\Upsilon_{223} \equiv 16j_1 \omega \phi_+(0) (-3e^{3T_z} (12F^2 + 10j_1 F + 3j_1^2) \cos^2(\varphi) F^3 - 2e^{\frac{3j_1}{F}} j_1^2 (2F - 3j_1) \phi_+^2(0) \omega^2)^3, \quad (\text{A16})$$

$$\Upsilon_{231} \equiv \cos(\varphi) \left(\Upsilon_{212} + e^{\frac{3j_1}{F}} j_1^2 \phi_+^2(0) \omega^2 (8F^2 - 12j_1 F + j_1^2 (9 - 4\omega^2)) \right)^2, \quad (\text{A17})$$

$$\Upsilon_{2321} \equiv 9e^{6T_z} (4224F^6 + 10688j_1 F^5 + 12272j_1^2 F^4 + 8112j_1^3 F^3 + 3258j_1^4 F^2 + 756j_1^5 F + 81j_1^6) \cos^4(\varphi) F^6, \quad (\text{A18})$$

$$\begin{aligned} \Upsilon_{2322} \equiv & 12e^{3(\frac{j_1}{F} + T_z)} j_1^2 \phi_+^2(0) \omega^2 \cos^2(\varphi) F^3 (896F^5 + 128j_1 F^4 - 48j_1^2 (6\omega^2 + 11) F^3 \\ & - 8j_1^3 (46\omega^2 + 45) F^2 - 9j_1^4 (20\omega^2 + 9) F - 36j_1^5 \omega^2), \end{aligned} \quad (\text{A19})$$

$$\begin{aligned} \Upsilon_{2323} \equiv & 2e^{\frac{6j_1}{F}} j_1^4 \phi_+^4(0) \omega^4 (384F^4 - 864j_1 F^3 - 8j_1^2 (32\omega^2 - 81) F^2 + 72j_1^3 (4\omega^2 - 3) F + 3j_1^4 (16\omega^4 - 24\omega^2 + 27)), \\ & \end{aligned} \quad (\text{A20})$$

$$\Upsilon_{233} \equiv 32F j_1^2 \omega \phi_+(0) (3e^{3T_z} (12F^2 + 10j_1 F + 3j_1^2) \cos^2(\varphi) F^3 + 2e^{\frac{3j_1}{F}} j_1^2 (2F - 3j_1) \phi_+^2(0) \omega^2)^4, \quad (\text{A21})$$

$$\Upsilon_{24} \equiv \frac{e^{\frac{3j_1}{F} - 3T_z} \phi_+(0) \omega (8F^2 - 12j_1 F + j_1^2 (9 - 4\omega^2)) \sec(\varphi)}{8F^3}, \quad (\text{A22})$$

where T_z is given by Eq. (71) and

$$j_1 \approx 2. \quad (\text{A23})$$

This j_1 is very insensitive to the parametric details because of the 1/6 power in

$$j_1 \approx \left(\frac{4\Upsilon^3 R_1}{\frac{4(3\Upsilon-2)F}{\Upsilon(\Upsilon+2)^3} + \frac{18(\Upsilon-2)}{(\Upsilon+2)^3}} \right)^{1/6}, \quad (\text{A24})$$

where

$$\begin{aligned} R_1 \equiv & \frac{\mathcal{A}_1 F}{2} + \frac{3}{2} \mathcal{A}_2 + \frac{1}{4F} \mathcal{A}_3 + \frac{81(4c_- + 27)j_1^2}{32F^3} \\ & + \frac{9j_1(3(4c_- + 45)j_1 \tau(j_1) + 4c_- - 4\omega^2 + 27)}{8F^2} \end{aligned} \quad (\text{A25})$$

and \mathcal{A}_n are functions of j_1 themselves given in Eqs. (A56), (A57), and (A58). With the fiducial value of $j_1 = 2$ without solving for j_1 self-consistently, the estimated error on j_1 is around 30% for an $O(2)$ variation in c_+ around 2.35. Note that j_1 here is the analog of the $(2n)^{1/4}/\sqrt{\alpha}$ in Eq. (75), and $j_1 = 2$ for $c_+ = 2.35$ is consistent with taking $n = 10$. This is one of the main consistency checks of this Appendix on Sec. IV. The c_+ parametric dependences of T_c values of this appendix section for c_+ near 2.35 agree with the presentation of Sec. IV providing another independent consistency check. If one wants better accuracy, it is straightforward (but tedious) to iterate using Eqs. (A5), (A81), (A79), and (A72). One of the most interesting aspects of this is Eq. (A100), which shows that $j_1 \approx 2$ and shows $0.5 \lesssim \Upsilon \lesssim 1$ to be a generic prediction in the resonant case. These results can also be viewed as an alternate method of computing T_c that can be combined with Eq. (222) to evaluate the isocurvature spectrum.

The improvement in the $\phi_-(T_c)$ solution can be seen by comparing the solid line and the long-dashed line in Fig. 16. In the parametric case of

$$\{c_+ = 2.35, c_- = 0.5, F = 20.2, \varepsilon_0 = 0, \phi_+(0) = 3.32 \times 10^8\} \quad (\text{A26})$$

the agreement with numerics is about 6% in $\Upsilon \approx 0.6$ [or equivalently about $0.06 \times (0.6/F)/T_c \approx 0.02\%$ in $T_c \approx 9.248$, which illustrates that a very high precision in T_c is required to get the $\phi_-(T_c)$ to be accurate to 6%]. For the more general case, we estimate an error for Υ of less than about 35% assuming that the error in the prediction for ϕ_- dominates. The Υ_1/Υ_2 ratio for this case of Eq. (A26) is about 5. The reason why the $\phi_-(T_c)$ computation is very sensitive to T_c is because small changes in ΔT_c lead to large changes in $\Delta \phi_-(T_c)$ since Eq. (A1) implies

$$\Delta \phi_-(T_c) \approx [\partial_T \phi_+(T_c) - \partial_T \phi_-(T_c)] \Delta T_c, \quad (\text{A27})$$

where $\partial_T \phi_+(T_c) \gg \phi_-$.

In the rest of this section, we derive these results. Readers not interested in the details can skip most of the rest of this section.

1. ϕ_{\pm} behavior in resonant scenarios

Here, we construct the ϕ_{\pm} solution in the region near T_c , where the perturbative expansion equations (50) and (51) break down. The tools we will use to construct this solution are (1) different derivative approximations $\partial_T^n \phi_{\pm}(T) \approx \partial_T^n \phi_{\pm}^{(0)}(T)$ for different n break down at different times T ; (2) an expansion of a different differential equation of composite operators that restricts the functional space of ϕ_{\pm} about a special point where $\dot{\phi}_+ = 0$. Note that the Taylor expansion method of (1) is nonperturbative although very limited in its time-range extension of analytic computation. For sudden transitions that are being studied here, even this limited method yields nearly an order of magnitude improvement in accuracy in the estimate.

a. Region $[T_c - j_1/F, T_c]$

As noted when discussing $\phi_-^{(1)}$ in Eq. (60), the $\phi_-^{(0)}$ solution becomes a bad solution exponentially fast near $T = T_c$. Hence, we will define below a time period $[T_c - j_1/F, T_c]$ just before T_c to match the known equation (59) to a finite order polynomial in this time region. The reason why the finite order polynomial will turn out to be a better approximation than the original perturbative

solutions will be due to the fact that different Taylor expansion derivative approximation $\partial_T^n \phi_{\pm}(T_c - j_1/F) \approx \partial_T^n \phi_{\pm}^{(0)}(T_c - j_1/F)$ for different n break down at different times T . We will choose j_1 from the condition that the finite order polynomial and $\partial_T^n \phi_{\pm}(T_c - j_1/F) \approx \partial_T^n \phi_{\pm}^{(0)}(T_c - j_1/F)$ be a good approximation at the same time.

Start with a quadratic Taylor expansion of $\phi_-(T)$ about $T = T_c$,

$$\begin{aligned} \phi_-(T) = & \phi_-\left(T_c - \frac{j_1}{F}\right) + \dot{\phi}_-\left(T_c - \frac{j_1}{F}\right) \left(T - T_c + \frac{j_1}{F}\right) \\ & + \frac{1}{2} \ddot{\phi}_-\left(T_c - \frac{j_1}{F}\right) \left(T - T_c + \frac{j_1}{F}\right)^2 + \dots \end{aligned} \quad (\text{A28})$$

We truncate this at the quadratic order and replace the coefficients with the leading perturbative solution:

$$\begin{aligned} \phi_-(T) \approx & \phi_-^{(0)}\left(T_c - \frac{j_1}{F}\right) + \dot{\phi}_-^{(0)}\left(T_c - \frac{j_1}{F}\right) \left(T - T_c + \frac{j_1}{F}\right) \\ & + \frac{1}{2} \ddot{\phi}_-^{(0)}\left(T_c - \frac{j_1}{F}\right) \left(T - T_c + \frac{j_1}{F}\right)^2 \\ & + \mathcal{E}_1(T) + \mathcal{E}_2(T), \end{aligned} \quad (\text{A29})$$

where the error estimate \mathcal{E}_1 is for the error incurred in matching the Taylor expansion coefficients to $\phi_-^{(0)}$ derivatives and \mathcal{E}_2 is the error incurred for the quadratic Taylor expansion truncation to the exact solution. It is important to keep in mind that the left-hand side of Eq. (A29) is not the approximate $\phi_-^{(0)}(T)$ but meant to be the *exact solution* that is valid even at T_c . If one forgets that, then this equation seems like an approximation of $\phi_-^{(0)}(T)$ as a quadratic function instead of the exact solution *in a small neighborhood*.

How can a Taylor expansion of $\phi_-^{(0)}$ do better than keeping the original $\phi_-^{(0)}$ itself? After all, why stop at just quadratic order in a $\phi_-^{(0)}$ Taylor expansion if one can get higher derivatives using $\phi_-^{(0)}$? The answer is that each successive derivative Taylor expansion coefficient evaluated at $T_c - j_1/F$ becomes an increasingly poor approximation of the exact solution's derivative $\partial_T^n \phi_- \neq \partial_T^n \phi_-^{(0)}$. We will demonstrate this explicitly.

In matching the exact solution to $\phi_-^{(0)}$ at $T = T_c - j_1/F$, the error incurred for the zeroth order Taylor expansion can be estimated using the perturbative solution equation (60) since at $T_c - j_1/F$, the λ perturbation of Eq. (60) is still valid,

$$\mathcal{E}_{10} = \left| \frac{\phi_-^{(1)}}{\phi_-^{(0)}} \right|_{T=T_c - \frac{j_1}{F}} \quad (\text{A30})$$

$$= \left\{ \frac{\frac{27}{4} + c_- + \omega^2 \sec^2[\omega T - \varphi] + \omega \tan[\omega T - \varphi](6 + \omega \tan[\omega T - \varphi])}{[\phi_+^{(0)}(T)]^2} \right\}_{T=T_c - \frac{j_1}{F}}, \quad (\text{A31})$$

$$\mathcal{E}_{11} = \left| \frac{\partial_T \phi_-^{(1)}}{\partial_T \phi_-^{(0)}} \right|_{T=T_c - \frac{j_1}{F}} \quad (\text{A32})$$

$$= \left\{ \frac{81 + 12c_- + 4\omega(10\omega \sec^2[\omega T - \varphi] + 18 \tan[\omega T - \varphi] - 3\omega)}{4[\phi_+^{(0)}(T)]^2} \right\}_{T=T_c - \frac{j_1}{F}}, \quad (\text{A33})$$

$$\mathcal{E}_{12} = \left| \frac{\partial_T^2 \phi_-^{(1)}}{\partial_T^2 \phi_-^{(0)}} \right|_{T=T_c - \frac{j_1}{F}} \quad (\text{A34})$$

$$= \left\{ \frac{1}{4[\phi_+^{(0)}(T)]^2} \left[\frac{112\omega^4 \sec^4(\omega T - \varphi) + 4\mathcal{T}_1(T) + 4\mathcal{T}_2(T)}{4\omega^2 \sec^2(\omega T - \varphi) + (3 + 2\omega \tan(\omega T - \varphi))^2} \right] \right\}_{T=T_c - \frac{j_1}{F}}, \quad (\text{A35})$$

$$\mathcal{T}_1(T) \equiv 9[3 + 2\omega \tan(\omega T - \varphi)]^2 \left[\frac{27}{4} + c_- + (6 + \omega \tan(\omega T - \varphi))\omega \tan(\omega T - \varphi) \right], \quad (\text{A36})$$

$$\mathcal{T}_2(T) \equiv 2\omega^2 \sec^2(\omega T - \varphi)[189 + 6c_- + 2\omega \tan(\omega T - \varphi)(129 + 44\omega \tan(\omega T - \varphi))], \quad (\text{A37})$$

where

$$\phi_-\left(T_c - \frac{j_1}{F}\right) = \phi_-^{(0)}\left(T_c - \frac{j_1}{F}\right)(1 + \mathcal{E}_{10}), \quad (\text{A38})$$

$$\partial_T \phi_-\left(T_c - \frac{j_1}{F}\right) = \partial_T \phi_-^{(0)}\left(T_c - \frac{j_1}{F}\right)(1 + \mathcal{E}_{11}), \quad (\text{A39})$$

$$\partial_T^2 \phi_-\left(T_c - \frac{j_1}{F}\right) = \partial_T^2 \phi_-^{(0)}\left(T_c - \frac{j_1}{F}\right)(1 + \mathcal{E}_{12}). \quad (\text{A40})$$

In the resonant cases in which j_1/F is not large enough to destroy the small cosine approximation $\cos(\omega T_c - \varphi) \approx \cos(\omega(T_z - T_c))$, we can use the following relationship:

$$\cos^2\left(\omega\left(T_c - \frac{j_1}{F}\right) - \varphi\right) \approx \omega^2 \left(\frac{j_1 + \Upsilon}{F}\right)^2 \ll 1, \quad (\text{A41})$$

where we have defined

$$\Upsilon \equiv (T_z - T_c)F. \quad (\text{A42})$$

This can be used to rewrite these errors as

$$\mathcal{E}_{10} = \frac{e^{-3j_1/F}}{r_1^2(j_1 \Upsilon^{-1} + 1)^2} \left[\frac{\frac{27}{4} + c_-}{F^2} + \frac{1}{(j_1 + \Upsilon)^2} + \frac{\sqrt{1 - \omega^2 \left(\frac{j_1 + \Upsilon}{F}\right)^2}}{j_1 + \Upsilon} \left(\frac{6}{F} + \frac{\sqrt{1 - \omega^2 \left(\frac{j_1 + \Upsilon}{F}\right)^2}}{j_1 + \Upsilon} \right) \right], \quad (\text{A43})$$

where

$$r_1 F \equiv \phi_+(0) e^{-3T_c/2} \sec(\varphi) \omega \Upsilon / F \quad (\text{A44})$$

has been defined to suggest the appropriate scale to understand this expression in the resonant case. Note that although it looks dimensionally wrong, it is actually consistent since we have divided out the H scale here. Our final value of computed Υ will determine r_1 . Similarly, the errors for the higher derivative coefficients are

$$\mathcal{E}_{11} = \frac{e^{-3j_1/F}}{r_1^2(j_1\Upsilon^{-1} + 1)^2} \left[\frac{\frac{81}{4} + 3c_-}{F^2} + \frac{10}{(j_1 + \Upsilon)^2} + \frac{18}{F} \frac{\sqrt{1 - \omega^2(\frac{j_1 + \Upsilon}{F})^2}}{j_1 + \Upsilon} - \frac{3\omega^2}{F^2} \right], \quad (\text{A45})$$

$$\mathcal{E}_{12} = \frac{e^{-3j_1/F}}{r_1^2(j_1\Upsilon^{-1} + 1)^2} \left[\frac{\frac{7}{(j_1 + \Upsilon)^2} + (j_1 + \Upsilon)^2 \frac{\mathcal{T}_1(T_c - \frac{j_1}{F}) + \mathcal{T}_2(T_c - \frac{j_1}{F})}{4F^4}}{1 + \frac{(j_1 + \Upsilon)^2}{4F^2} \left(3 + 2F \frac{\sqrt{1 - \omega^2(\frac{j_1 + \Upsilon}{F})^2}}{j_1 + \Upsilon} \right)^2} \right], \quad (\text{A46})$$

$$\mathcal{T}_1\left(T_c - \frac{j_1}{F}\right) \approx 9 \left[3 + 2 \frac{\sqrt{1 - \omega^2(\frac{j_1 + \Upsilon}{F})^2}}{(\frac{j_1 + \Upsilon}{F})} \right]^2 \left[\frac{27}{4} + c_- + \frac{\sqrt{1 - \omega^2(\frac{j_1 + \Upsilon}{F})^2}}{(\frac{j_1 + \Upsilon}{F})} \left(6 + \frac{\sqrt{1 - \omega^2(\frac{j_1 + \Upsilon}{F})^2}}{(\frac{j_1 + \Upsilon}{F})} \right) \right], \quad (\text{A47})$$

$$\mathcal{T}_2\left(T_c - \frac{j_1}{F}\right) \approx 2 \frac{1}{(\frac{j_1 + \Upsilon}{F})^2} \left[189 + 6c_- + 2 \frac{\sqrt{1 - \omega^2(\frac{j_1 + \Upsilon}{F})^2}}{(\frac{j_1 + \Upsilon}{F})} \left(129 + 44 \frac{\sqrt{1 - \omega^2(\frac{j_1 + \Upsilon}{F})^2}}{(\frac{j_1 + \Upsilon}{F})} \right) \right]. \quad (\text{A48})$$

One can see from Fig. 15 (in which we plot \mathcal{E}_{10} , \mathcal{E}_{11} , \mathcal{E}_{12}) how the higher order Taylor expansion coefficients become more uncertain earlier before reaching T_c . In this numerical example case, we see that to keep the second order Taylor expansion coefficient accurate to about 20%, we need to Taylor expand at about $T_c - 2/F \approx 9.15$. The actual error \mathcal{E}_1 at T_c can be better than 20% depending on which Taylor expansion term contributes the most.

Hence, we conclude based on coefficient errors alone

$$\mathcal{E}_1(T_c) \approx \left| \phi_-^{(1)}\left(T_c - \frac{j_1}{F}\right) + \dot{\phi}_-^{(1)}\left(T_c - \frac{j_1}{F}\right) \frac{j_1}{F} + \frac{1}{2} \ddot{\phi}_-^{(1)}\left(T_c - \frac{j_1}{F}\right) \left(\frac{j_1}{F}\right)^2 \right|, \quad (\text{A49})$$

$$\phi_-^{(1)}\left(T_c - \frac{j_1}{F}\right) = \frac{e^{\frac{3}{2}T_c} F^2 \cos^3 \varphi \sec^3(\omega T - \varphi)}{\phi_+^3(0)} \left[\frac{27}{4} + c_- + \omega^2 \sec^2[\omega T - \varphi] + \omega \tan[\omega T - \varphi] (6 + \omega \tan[\omega T - \varphi]) \right]_{T_c - \frac{j_1}{F}}, \quad (\text{A50})$$

$$\begin{aligned} \dot{\phi}_-^{(1)}\left(T_c - \frac{j_1}{F}\right) &= \frac{e^{\frac{3}{2}T_c} F^2 \cos^3 \varphi \sec^3(\omega T - \varphi)}{\phi_+^3(0)} \left(\frac{3}{2} + \omega \tan[\omega T - \varphi] \right) \\ &\quad \times \left[\frac{81}{4} + 3c_- + \omega(10\omega \sec^2[\omega T - \varphi] + 18 \tan[\omega T - \varphi] - 3\omega) \right]_{T_c - \frac{j_1}{F}}, \end{aligned} \quad (\text{A51})$$

$$\ddot{\phi}_-^{(1)}\left(T_c - \frac{j_1}{F}\right) = \frac{e^{\frac{3}{2}T_c} F^2 \cos^3 \varphi \sec^3(\omega T - \varphi)}{\phi_+^3(0)} [7\omega^4 \sec^4(\omega T - \varphi) + \tilde{\mathcal{T}}_1 + \tilde{\mathcal{T}}_2]_{T_c - \frac{j_1}{F}}, \quad (\text{A52})$$

$$\tilde{\mathcal{T}}_1 = \frac{\omega^2}{2} \sec^2(\omega T - \varphi) [189 + 6c_- + 2\omega \tan(\omega T - \varphi) (129 + 44\omega \tan(\omega T - \varphi))]_{T_c - \frac{j_1}{F}}, \quad (\text{A53})$$

$$\tilde{\mathcal{T}}_2 = \frac{9}{4} [3 + 2\omega \tan(\omega T - \varphi)]^2 \left[\frac{27}{4} + c_- + \omega \tan(\omega T - \varphi) (6 + \tan(\omega T - \varphi)) \right]_{T_c - \frac{j_1}{F}}. \quad (\text{A54})$$

In the resonant case, we can expand as before about $T = T_c$:

$$\mathcal{E}_1(T_c) \approx \frac{\Upsilon^3 e^{-\frac{9j_1}{2F}} \left(\frac{\mathcal{A}_1 F}{2} + \frac{3}{2} \mathcal{A}_2 + \frac{1}{4F} \mathcal{A}_3 + \frac{81(4c_- + 27)j_1^2}{32F^3} + \frac{9j_1(3(4c_- + 45)j_1 \tau(j_1) + 4c_- - 4\omega^2 + 27)}{8F^2} \right)}{r_1^3(j_1 + \Upsilon)^3}, \quad (\text{A55})$$

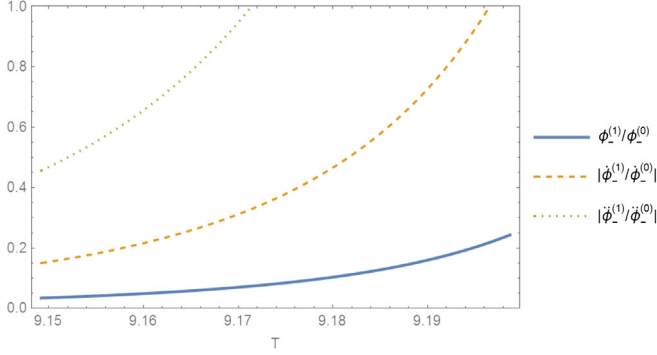


FIG. 15. Uncertainty in the Taylor expansion coefficients as a function of matching time T for the same parameters as in Fig. 1 for which $T_c = 9.248$ (the rightmost T is about $T_c - 1/F$ and the leftmost T is about $T_c - 2/F$). Note that as expected, the higher derivatives become nonperturbative faster as T approaches T_c , which is consistent with the notion that truncated Taylor expansions are better approximations over a longer time period as T_c is approached. This shows that we want to match the Taylor expansion coefficients to the zeroth order perturbative solution at an earlier time as much as possible.

$$\begin{aligned} \mathcal{A}_1(j_1) &\equiv \tau^2(j_1)(2 + 9j_1^2\tau^2(j_1)) + \frac{7j_1^2}{(j_1 + \Upsilon)^4} \\ &\quad + \frac{2 + 4j_1\tau(j_1)(5 + 11j_1\tau(j_1))}{(j_1 + \Upsilon)^2}, \end{aligned} \quad (\text{A56})$$

$$\begin{aligned} \mathcal{A}_2(j_1) &\equiv \tau(j_1)(4 + 3j_1\tau(j_1)(4 + 9j_1\tau(j_1))) \\ &\quad + \frac{j_1(10 + 43j_1\tau(j_1))}{(j_1 + \Upsilon)^2}, \end{aligned} \quad (\text{A57})$$

$$\begin{aligned} \mathcal{A}_3(j_1) &\equiv 27(1 + 7j_1\tau(j_1)) + 4c_- + 18j_1^2\tau^2(j_1)(27 + c_-) \\ &\quad + 12j_1\tau(j_1)(c_- - \omega^2) + \frac{3j_1^2(63 + 2c_-)}{(j_1 + \Upsilon)^2}, \end{aligned} \quad (\text{A58})$$

$$\tau(j_1) \equiv \frac{\sqrt{1 - \frac{\omega^2(j_1 + \Upsilon)^2}{F^2}}}{j_1 + \Upsilon} \approx \frac{1}{j_1 + \Upsilon}, \quad (\text{A59})$$

where one should keep in mind that Υ and r_1 are of order unity in the resonant scenarios where the expansion involving Υ about the zero crossing of $\cos(\omega T - \varphi)$ has been made. Since we are evaluating at $T_c - j_1/F$, which is farther away from the zero crossing of $\cos(\omega T - \varphi)$, this expression is only about 25% accurate. Typically, the $\mathcal{A}_1 F/2$ term dominates and this large coefficient pushes the error toward larger than unity at T_c . Therefore j_1 needs to be made as large as possible to induce the $(j_1 + \Upsilon)^{-3}$ in Eq. (A55) to reduce \mathcal{E}_1 . This is a motivation for having a quadratic Taylor expansion compared to a linear Taylor

expansion since generically a Taylor expansion has a larger degree of accuracy for higher order polynomials.¹⁵

Let us discuss the competing error \mathcal{E}_2 incurred from Taylor expanding the exact solution to quadratic order (which is always possible for any analytic solution in a sufficiently small neighborhood):

$$\mathcal{E}_2(T) = \left| \frac{1}{6} \max_{u \in [T_c - 1/F, T_c]} \partial_T^3 \phi_-(u) \left(T - T_c + \frac{j_1}{F} \right)^3 \right|. \quad (\text{A60})$$

According to the equation of motion for ϕ_- [Eq. (18)]:

$$\begin{aligned} \partial_T^3 \phi_-(u) &= -[-3(3\dot{\phi}_-(u) + c_- \phi_- + (\phi_+ \phi_- - F^2)\phi_+) \\ &\quad + c_- \dot{\phi}_-(u) + (2\phi_+(u)\phi_-(u) - F^2)\dot{\phi}_+(u) \\ &\quad + \phi_+^2(u)\dot{\phi}_-(u)]. \end{aligned} \quad (\text{A61})$$

Let us first see why it is a bit delicate to estimate the rhs. We know that the largest contribution to the rhs of Eq. (A61) are from the potential terms near its maximum since $F^2 \dot{\phi}_+ \gtrsim F^4$:

$$\partial_T^3 \phi_-(u) \sim -[(2\phi_+(u)\phi_-(u) - F^2)\dot{\phi}_+(u) + \phi_+^2(u)\dot{\phi}_-(u)]. \quad (\text{A62})$$

There is a partial cancellation in this expression since at least at $T_c - j_1/F$, we have by construction

$$\phi_+ \phi_- \sim F^2 \rightarrow \dot{\phi}_+ \phi_- \sim -\dot{\phi}_- \phi_+, \quad (\text{A63})$$

making

$$\partial_u^3 \phi_-(u) \approx -[(\phi_+(u)\phi_-(u) - F^2)\dot{\phi}_+(u)]. \quad (\text{A64})$$

This cancellation fails more and more as $\phi_+ \phi_-$ becomes smaller and smaller compared to F^2 as u approaches T_c . This means we expect $\partial_u^3 \phi_-(u)$ to be maximized near T_c . On the other hand, since $(2\phi_+(u)\phi_-(u) - F^2)\dot{\phi}_+(u) < 0$ near $T_c - j_1/F$ (since that is where $\phi_+ \phi_- \sim F^2$), whereas $\phi_+^2(u)\dot{\phi}_-(u) > 0$ in this region, there is a cancellation which could increase near T_c , making the exact location of the maximum of $\partial_u^3 \phi_-$ uncertain. Nonetheless, as long as T_c does not exactly represent the zero of $\partial_u^3 \phi_-(u)$, we expect from these arguments that

¹⁵One might ask, why not then go to even higher orders in Taylor expansion? That is because of Fig. 15, which tells us that the higher order polynomial coefficients are not approximated well for a given expansion point $T = T_c - j_1/F$. To rigorously optimize, one would have to minimize the error in the (n, j_1) plane where n is the degree of polynomial with which one is expanding. However, we will be content with setting $n = 2$ and maximizing j_1 to approximately minimize the error.

$$|\partial_u^3 \phi_-(T_c)| \sim O\left(\max_{u \in [T_c - \frac{1}{F}, T_c]} \partial_T^3 \phi_-(u)\right), \quad (\text{A65})$$

which is what we will evaluate now.

Since the rhs of Eq. (A62) only involves first derivatives and lower, we can use the assumed solution to evaluate these derivatives:

$$\begin{aligned} \phi_-(T) &\approx \phi_-^{(0)}\left(T_c - \frac{j_1}{F}\right) + \dot{\phi}_-^{(0)}\left(T_c - \frac{j_1}{F}\right)\left(T - T_c + \frac{j_1}{F}\right) \\ &\quad + \frac{1}{2}\ddot{\phi}_-^{(0)}\left(T_c - \frac{j_1}{F}\right)\left(T - T_c + \frac{j_1}{F}\right)^2, \end{aligned} \quad (\text{A66})$$

which when evaluated at T_c is

$$\begin{aligned} \phi_-(T_c) &\approx \phi_-^{(0)}\left(T_c - \frac{j_1}{F}\right) + \dot{\phi}_-^{(0)}\left(T_c - \frac{j_1}{F}\right)\left(\frac{j_1}{F}\right) \\ &\quad + \frac{1}{2}\ddot{\phi}_-^{(0)}\left(T_c - \frac{j_1}{F}\right)\left(\frac{j_1}{F}\right)^2. \end{aligned} \quad (\text{A67})$$

The derivative can also be evaluated at T_c :

$$\dot{\phi}_-(T_c) \approx \dot{\phi}_-^{(0)}\left(T_c - \frac{j_1}{F}\right) + \frac{1}{2}\ddot{\phi}_-^{(0)}\left(T_c - \frac{j_1}{F}\right)\left(\frac{j_1}{F}\right). \quad (\text{A68})$$

After using Eq. (A44), the largest number in $\partial_T^3 \phi_-$ is F . Hence, we expand in powers of F to obtain

$$\partial_T^3 \phi_-(T_c) \approx \frac{4r_1(3\Upsilon - 2)F^4}{\Upsilon(\Upsilon + 2)^3} + \frac{18r_1(\Upsilon - 2)F^3}{(\Upsilon + 2)^3}, \quad (\text{A69})$$

where r_1 is defined in Eq. (A44) and Υ is defined as

$$\Upsilon \equiv (T_z - T_c)F \sim O(1), \quad (\text{A70})$$

where T_z is given by Eq. (71). Note the mass matrix becomes strongly off diagonal at T_z : i.e.,

$$\frac{F^2}{\phi_+(0)e^{-\frac{3}{2}T_z} \sec(\varphi)} \approx O(F). \quad (\text{A71})$$

Because $(\Upsilon + 2)^3$ can easily be of order F (because of the cubic power) and because 18 can be of order F , these two terms can compete. Also, $3\Upsilon - 2$ can easily be negative. Hence we arrive at the Taylor expansion error estimate

$$\mathcal{E}_2(T_c) = \left| \frac{1}{6} \left(\frac{4r_1(3\Upsilon - 2)F}{\Upsilon(\Upsilon + 2)^3} + \frac{18r_1(\Upsilon - 2)}{(\Upsilon + 2)^3} \right) j_1^3 \right| \quad (\text{A72})$$

at T_c . The equivalent fractional error of Taylor expansion is

$$\left| \frac{\mathcal{E}_2(T_c)}{\phi_-(T_c)} \right| \approx \left| \frac{r_1}{r} \left(\frac{(2\Upsilon - \frac{4}{3})}{\Upsilon(\Upsilon + 2)^3} + \frac{3(\Upsilon - 2)}{(\Upsilon + 2)^3 F} \right) j_1^3 \right|, \quad (\text{A73})$$

where

$$\frac{r_1}{r} = \frac{\phi_+^{(0)}(T_c)}{\phi_+(T_c)} \approx 1, \quad (\text{A74})$$

r and r_1 were defined in Eqs. (A2) and (A44). This error pushes the choice of j_1 toward smaller values (i.e., in the opposite direction of the push by \mathcal{E}_1). To evaluate this error, we need a value of Υ (or equivalently T_c) which is calculated with j_1 fixed. Hence, Υ itself is a function of j_1 .

Ideally, we want to compute

$$\frac{d}{dj_1} [\mathcal{E}_1(T_c(j_1)) + \mathcal{E}_2(T_c(j_1))] = 0 \quad (\text{A75})$$

to minimize the errors. Because Υ itself depends on j_1 , the derivative is tedious to obtain.

The combined error (in absolute values added instead of quadrature) is plotted in Fig. 16.¹⁶ We see that the minimum error occurs when the Taylor expansion point of Eq. (A29) is $T \approx T_c - 2/F$. The expected error for the value of the function is at most around 35%. However, to get the plots [or equivalently, to use Eqs. (A55) and (A72)], we need to compute Υ for a given model, i.e., $T_c = T_z - \Upsilon F^{-1}$ using Eqs. (A1), (A29), and the analogous equation for ϕ_+ approximation:

$$\begin{aligned} \phi_+(T) &\approx \phi_+^{(0)}\left(T_c - \frac{j_1}{F}\right) + \dot{\phi}_+^{(0)}\left(T_c - \frac{j_1}{F}\right)\left(T - T_c + \frac{j_1}{F}\right) \\ &\quad + \frac{1}{2}\ddot{\phi}_+^{(0)}\left(T_c - \frac{j_1}{F}\right)\left(T - T_c + \frac{j_1}{F}\right)^2. \end{aligned} \quad (\text{A76})$$

However, in practice this does not need to be done. That is because the minimum error generating j_1 is not sensitive to the exact value of T_c . This is illustrated in Fig. 17 where the errors are evaluated with two different estimates of T_c . The Taylor approximation curve is generated by solving for T_c self-consistently by solving

$$\phi_+^{\text{Taylor}}(T_c)|_{j_1} = \phi_-^{\text{Taylor}}(T_c)|_{j_1} \quad (\text{A77})$$

for $T_c = T_c(j_1)$, which is now a function of j_1 and evaluating $\mathcal{E}_1(j_1, T) + \mathcal{E}_2(j_1, T)$ evaluated at $T = T_c(j_1)$. The ‘‘naive T_c ’’ curve is generated by solving

$$|\phi_-^{(0)}(T_c^{\text{naive}})| = F \quad (\text{A78})$$

and Eq. (A71) is satisfied. Hence, we see $j_1 \approx 2$ gives the minimum error in the parametric case of Fig. 1.

¹⁶Although we could add in quadrature to tighten the error estimates, we here stay conservative both because we do not really know the distribution shape of the errors and because we want to keep the algebra simpler.

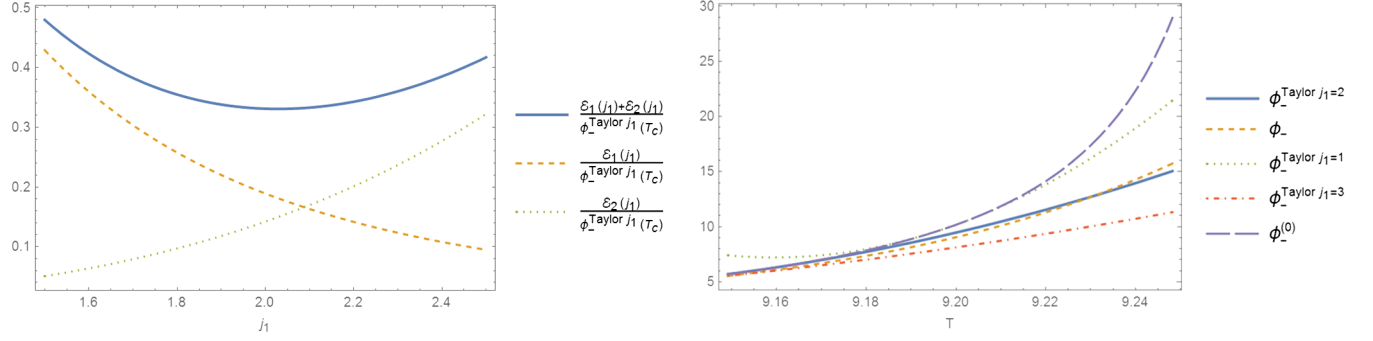


FIG. 16. Left panel: combined error for the case of the fiducial parameters of Fig. 1 (e.g., $T_c = 9.248$). The value of $\Upsilon \approx 0.6$ corresponding to the approximate location of T_c has been fixed by hand and not varied with j_1 . The minimum error for the value of $\phi_-(T_c)$ using Eq. (A29) occurs at around $j_1 = 2$ corresponding to a Taylor expansion at $T = T_c - 2/F$. The denominator $\phi_{\text{Taylor } j_1}(T_c)$ used for this comparison plot has been made using Eq. (A29) instead. Right panel: the right plot shows the approximate $\phi_{\text{Taylor } j_1=2}$ of Eq. (A29) matches the numerical solution ϕ_- very well compared to the approximation obtained with $j_1 = 1$. It is clear that the solution where the Taylor expansion is done about $j_1 = 2$ works much better than the approximation made through expanding about $j_1 = 1$ or $j_1 = 3$ as predicted by the left plot. Also, as expected and noted before, all the Taylor expansion approximations in the $j_1 \in [1, 3]$ are much better than the zeroth λ order solution $\phi_-^{(0)}$.

Let us analyze the sensitivity of j_1 to the parameters more generally. Start by rewriting Eq. (A55) as

$$\mathcal{E}_1(T_c) \approx \frac{\Upsilon^3 e^{-\frac{9j_1}{2F}} R_1}{r_1^3 (j_1 + \Upsilon)^3}, \quad (\text{A79})$$

$$R_1 \equiv \frac{\mathcal{A}_1 F}{2} + \frac{3}{2} \mathcal{A}_2 + \frac{1}{4F} \mathcal{A}_3 + \frac{81(4c_- + 27)j_1^2}{32F^3} + \frac{9j_1(3(4c_- + 45)j_1 \tau(j_1) + 4c_- - 4\omega^2 + 27)}{8F^2}. \quad (\text{A80})$$

The solution to Eq. (A75) is thus

$$\left(\frac{-9}{2F} + \frac{-3(1 + \partial_{j_1} \Upsilon)}{(j_1 + \Upsilon)} + \frac{3\partial_{j_1} \Upsilon}{\Upsilon} + \frac{\partial_{j_1} R_1}{R_1} + \frac{\partial_{j_1} \Upsilon \partial_{\Upsilon} R_1}{R_1} \right) \mathcal{E}_1 + \frac{3}{j_1} \mathcal{E}_2 = 0. \quad (\text{A81})$$

To get an approximation for the solution, we approximate R_1 as a smooth polynomial in j_1 , note $\frac{9}{2F}$ is unimportant, and assume that we are close to the solution of Eq. (A75) such that $|\partial_{j_1} \Upsilon / \Upsilon| \ll 1$:

$$\frac{d}{dj_1} [\mathcal{E}_1(T_c) + \mathcal{E}_2(T_c)] \approx \left(\frac{-3}{(j_1 + \Upsilon)} + \frac{O(1)}{j_1} \right) \mathcal{E}_1 + \frac{3}{j_1} \mathcal{E}_2. \quad (\text{A82})$$

Setting this to zero gives

$$\mathcal{E}_2 = \left(\frac{j_1}{(j_1 + \Upsilon)} - \frac{O(1)}{3} \right) \mathcal{E}_1 \quad (\text{A83})$$

or equivalently

$$\left| \frac{1}{6} \left(\frac{4r_1(3\Upsilon - 2)F}{\Upsilon(\Upsilon + 2)^3} + \frac{18r_1(\Upsilon - 2)}{(\Upsilon + 2)^3} \right) j_1^3 \right| = \left(\frac{j_1}{(j_1 + \Upsilon)} - \frac{O(1)}{3} \right) \frac{\Upsilon^3 e^{-\frac{9j_1}{2F}} R_1}{r_1^3 (j_1 + \Upsilon)^3}. \quad (\text{A84})$$

Hence, for $j_1 \gtrsim 2\Upsilon$ we can approximate

$$j_1 \approx \left(\frac{4\Upsilon^3 R_1}{\left| \frac{4(3\Upsilon - 2)F}{\Upsilon(\Upsilon + 2)^3} + \frac{18(\Upsilon - 2)}{(\Upsilon + 2)^3} \right|} \right)^{1/6}. \quad (\text{A85})$$

Since Υ stays near unity for different c_+ and $R_1 \sim O(F)$, we see that this j_1 varies slowly with different parameters of c_+ owing to the $1/6$ power dependence. Hence, we will use the result of Fig. 17 and use

$$j_1 = 2$$

for the resonant cases. This should be a good approximation to about 30% accuracy since $1/6$ power reduces $O(1)$ uncertainties to about this level. The j_1 variable is the analog of the $(2n)^{1/4}/\sqrt{\alpha}$ in Eq. (75), and $j_1 = 2$ for $c_+ = 2.35$ is consistent with taking $n = 10$. This Appendix has thus provided a consistency check as well as an error estimate of Sec. IV.

2. Solving for T_c

Although the value of j_1 that minimizes the error is not very sensitive to the value of T_c , we see from the second figure of Fig. 17 that $\phi_+(T_c)$ is sensitive to T_c . We defined T_c to be the solution of Eq. (A1), which is approximately

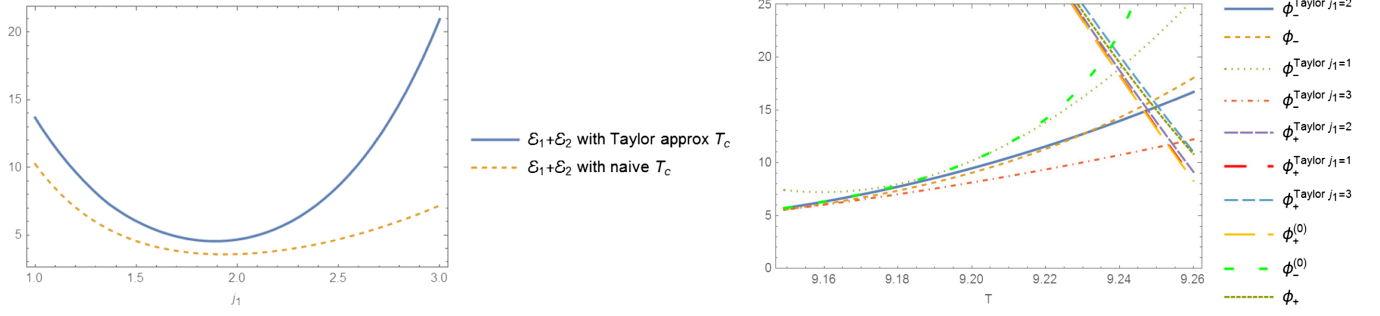


FIG. 17. Here, we again consider the parametric point of Fig. 1. Errors with less accurate T_c (the dashed curve) gives about the same j_1 location of the minimum error as the errors evaluated with the more accurate T_c (the solid curve). The exact definition of the more accurate versus less accurate value of T_c is explained in the text. This insensitivity is expected to occur because of the steepness of the slope of ϕ_{+} in the resonant case as seen the second figure, where we put on top of Fig. 16 various ϕ_{+} approximations. Note unlike in the case of $\phi_{-}^{(0)}$, the leading perturbative $\phi_{+}^{(0)}$ solution accurately describes the numerical solution at $T_c \approx 9.248$.

$$\begin{aligned} & \phi_{+}^{(0)} \left(T_c - \frac{j_1}{F} \right) + \dot{\phi}_{+}^{(0)} \left(T_c - \frac{j_1}{F} \right) \left(\frac{j_1}{F} \right) + \frac{1}{2} \ddot{\phi}_{+}^{(0)} \left(T_c - \frac{j_1}{F} \right) \left(\frac{j_1}{F} \right)^2 \\ & = \phi_{-}^{(0)} \left(T_c - \frac{j_1}{F} \right) + \dot{\phi}_{-}^{(0)} \left(T_c - \frac{j_1}{F} \right) \left(\frac{j_1}{F} \right) + \frac{1}{2} \ddot{\phi}_{-}^{(0)} \left(T_c - \frac{j_1}{F} \right) \left(\frac{j_1}{F} \right)^2. \end{aligned} \quad (\text{A86})$$

This equation and Eq. (A75) together determine j_1 and Υ [where Υ is a parametrization of T_c through Eq. (A70)].

Use resonant condition

$$\cos \left(\omega \left(T_c - \frac{j_1}{F} \right) - \varphi \right) \approx \omega \frac{j_1 + \Upsilon}{F} \quad (\text{A87})$$

to turn the trigonometric functions in this expression into polynomials:

$$\begin{aligned} 0 = & \frac{\phi_{+}(0) \omega \sec(\varphi) e^{\frac{3(-FT_z + j_1 + \Upsilon)}{F}} (8F^2 \Upsilon + j_1 (-12F \Upsilon - j_1 (4\omega^2 - 9)(j_1 + \Upsilon)))}{8F^3} \\ & - \frac{F \cos(\varphi) (8F^2 (3j_1^2 + 3j_1 \Upsilon + \Upsilon^2) + 12F j_1 (j_1 + \Upsilon) (2j_1 + \Upsilon) + 9j_1^2 (j_1 + \Upsilon)^2)}{8\phi_{+}(0) \omega (j_1 + \Upsilon)^3}. \end{aligned} \quad (\text{A88})$$

Although this equation can be linearized successively to obtain an accurate solution, the algebra becomes significantly simpler with only about an $O(3\Upsilon/(FT_z))$ loss of precision if we drop the Υ dependence on arising from the exponent

$$e^{\frac{3(-FT_z + j_1 + \Upsilon)}{F}} = \exp \left(-3T_z + \frac{3j_1}{F} + 3\Upsilon F^{-1} \right) \quad (\text{A89})$$

$$\approx \exp \left(-3T_z + \frac{3j_1}{F} \right). \quad (\text{A90})$$

Use successive linearization (effective Newton's method) to obtain a solution to the simplified nonlinear equation:

$$T_c = T_z - \Upsilon F^{-1}, \quad (\text{A91})$$

$$\Upsilon \approx \Upsilon_1 + \Upsilon_2, \quad (\text{A92})$$

$$\Upsilon_1 \equiv - \frac{j_1 \left(3 \frac{F^4}{\phi_{+}(0)^2} e^{3T_z} (8F^2 + 8F j_1 + 3j_1^2) \cos^2(\varphi) + j_1^4 \omega^2 (4\omega^2 - 9) e^{\frac{3j_1}{F}} \right)}{j_1^2 \omega^2 e^{\frac{3j_1}{F}} (-8F^2 + 12F j_1 + j_1^2 (4\omega^2 - 9)) - 3 \frac{F^4}{\phi_{+}(0)^2} e^{3T_z} (16F^2 + 12F j_1 + 3j_1^2) \cos^2(\varphi)}, \quad (\text{A93})$$

where the definition of the rest of the Υ_X objects are given in Eqs. (A7)–(A22). These expressions indicate that $\Upsilon \sim O(1)$ since for example in the Υ_1 contribution we have contributions such as

$$3 \frac{F^4}{\phi_+(0)^2} e^{3T_z} (8F^2 + 8Fj_1 + 3j_1^2) \cos^2(\varphi) \sim \frac{F^4}{F^4} O(F^2) \quad (\text{A94})$$

in the numerator¹⁷ with an $O(F^2)$ in the denominator. Also, note that even though Υ looks like it is sensitive to j_1 , one can check that there are cancellations when the j_1 derivative of Υ is computed. This cancellation occurs because if the j_1 is chosen in the region where the error $\mathcal{E}_1 + \mathcal{E}_2$ of Eq. (A29) is minimized, the sensitivity on j_1 by construction is minimized.

For example, consider

$$\frac{\partial \Upsilon}{\partial j_1} \sim \frac{\partial \Upsilon_1}{\partial j_1} = \frac{\partial}{\partial j_1} \left(\frac{\mathcal{N}_{\Upsilon_1}}{\mathcal{D}_{\Upsilon_2}} \right), \quad (\text{A95})$$

where \mathcal{N}_{Υ_1} is the numerator and \mathcal{D}_{Υ_1} is the denominator of Eq. (A93). The derivative receives contributions from the numerator and denominator (after combining over a common denominator)

$$\left(\frac{\partial \mathcal{N}_{\Upsilon_1}}{\partial j_1} \right) \mathcal{D}_{\Upsilon_2} = K \left(\frac{6F^4}{\phi_+^2(0) e^{-3T_z} \sec^2 \varphi} + e^{\frac{3j_1}{F}} j_1^2 \omega^2 + \dots \right), \quad (\text{A96})$$

$$-\mathcal{N}_{\Upsilon_1} \left(\frac{\partial \mathcal{D}_{\Upsilon_2}}{\partial j_1} \right) = K (-2e^{\frac{3j_1}{F}} j_1^2 \omega^2 + \dots), \quad (\text{A97})$$

where K is a common factor and we have displayed the leading terms.¹⁸ To see the cancellation between these two terms, Eq. (A96) can be rewritten using Eq. (A70):

$$\begin{aligned} K \left(\frac{6F^4}{\phi_+^2(0) e^{-3T_z} \sec^2 \varphi} + e^{\frac{3j_1}{F}} j_1^2 \omega^2 + \dots \right) \\ = K \left(\frac{6F^4}{\phi_+^2(0) e^{-3(T_z - \Upsilon/F)} e^{-3\Upsilon/F} \sec^2 \varphi} + e^{\frac{3j_1}{F}} j_1^2 \omega^2 + \dots \right) \end{aligned} \quad (\text{A98})$$

$$= K \left(\left[\frac{\Upsilon^2 6}{e^{-3\Upsilon/F}} e^{-\frac{3j_1}{F}} + j_1^2 \right] e^{\frac{3j_1}{F}} \omega^2 + \dots \right). \quad (\text{A99})$$

Comparing with Eq. (A97), we see that the cancellation occurs because

$$\left| \left(\frac{\Upsilon^2 6}{e^{-3\Upsilon/F}} e^{-\frac{3j_1}{F}} + j_1^2 \right) - 2j_1^2 \right| \ll 2j_1^2. \quad (\text{A100})$$

One of the merits of this exercise is to see that this cancellation is independent of c_+ in the resonant region considered here. This also allows one to see Υ has to be in the approximate region of the zero of the left-hand side of Eq. (A100).

In the case of $c_+ = 2.35$ considered in the plots such as 1, Υ_1 dominates over Υ_2 by about a factor of 5. However, since the entire point of this messy exercise was to obtain a good numerical estimate of T_c , we keep Υ_2 . In this parametric point example, we find Eq. (A92) evaluates to

$$\Upsilon \approx 0.64 \quad (\text{A101})$$

with $T_z = 9.278$, while the numerical solution for this case is

$$\Upsilon^{\text{numerical}} \approx 0.61, \quad (\text{A102})$$

attesting to a good approximation (about 5% error). Note this also allows us to compute for example

$$\phi_+(T_c) \approx \phi_+(0) \exp \left(\frac{-3}{2} \left[T_z - \frac{\Upsilon}{F} \right] \right) \sec(\varphi) \omega \Upsilon / F \quad (\text{A103})$$

$$\approx 15.294, \quad (\text{A104})$$

giving

$$r_1 \approx 0.76 \quad (\text{A105})$$

[defined in Eq. (A44)] very close to the numerical value of $r_1^{\text{numerical}} = 0.78$. In evaluating this, we made use of Eqs. (71) and (32) as well.

The error in the more general case can be estimated as follows. To account for the $u = 35\%$ type of error $\Delta\phi_-$ in the $\phi_-(T_c)$ field value, note

$$\Delta T_c \approx \frac{\Delta\phi_-}{\partial_T \phi_+(T_c) - \partial_T \phi_-(T_c)} \quad (\text{A106})$$

$$\approx \frac{uF}{\partial_T \phi_+(T_c)} \quad (\text{A107})$$

$$\sim \frac{u}{F}, \quad (\text{A108})$$

which means that the error in ϕ_- shifts Υ by u . This is why T_c has to be very accurately determined to obtain $\Delta\phi_-$.

¹⁷Recall that $\phi_+(0) e^{-3T_z/2} \sim O(F^2)$ in the resonant scenarios.

¹⁸Leading terms at least for c_+ near the 2.35 parametric region.

APPENDIX B: SMALL α

For field configuration where $\alpha < \alpha_L$ [where α_L is defined in Eq. (93)] at transition, the resonant conditions in Sec. IV C are not satisfied. In such cases, the mass eigenvalue and the rotated eigenvector gradient effects are less than $O(F)$ post transition. As a result, the axion mass transitions smoothly from c_+ to a massless state. In these cases, the separation between the transition T_c and the zero crossing T_z is usually $O(1)$. However, by evaluating Eq. (60) at T_c , one finds that the leading order correction $\phi_-^{(1)} \sim 2\alpha^2 F$. Hence, we see that the perturbative solution is still valid for $\alpha < \alpha_L$ and the cumbersome nonperturbative computation is no longer necessary for computing the value of the fields at T_c . However, to compute the spectrum, $-V_1$ still needs to be computed, and this requires an accurate computation of T_c using the nonperturbative computation that we have presented in Sec. IV. Using this $-V_1$ and a slowly time-dependent mass squared function m_B^2 , the final mode amplitude can be computed. The absence of resonance and a weak V_1 dip less than $O(F)$ results in a power spectrum with the long wavelength region plateauing after the first bump without any further noticeable bumps similar to an overdamped scenario.

APPENDIX C: ADIABATIC APPROXIMATION FOR AN OSCILLATING TIME-SPACE POTENTIAL

Consider the following second order ODE with an oscillating time space potential:

$$\ddot{y} + A\beta(t) \cos(ft)y = 0,$$

where $\beta(t)$ is a slow-varying envelope function with amplitude A , while the harmonic oscillations are rapidly varying (large frequency f). The solution $y(t)$ of the aforementioned ODE can be approximated by separating into the IR and UV components. As long as this hierarchy can be maintained we can approximate y as

$$y = y_s + y_f, \quad (\text{C1})$$

whereby y_s represents the slow-varying (IR) adiabatic behavior superimposed with a fast high-frequency (UV) noise y_f . Next, we substitute this into our original equation to get

$$\ddot{y}_s + \ddot{y}_f + A\beta(t) \cos(ft)(y_s + y_f) = 0.$$

We now apply the initial conditions. Assuming that the incoming function is $y = y_0$ at some $t = t_0$ and has no UV behavior, the slow-varying component y_s will match appropriately with the y_0 . The fast-varying y_f will then be matched with 0 or be negligible. Accordingly, over a small timescale Δt , the UV component will be initially sourced by the incoming IR component

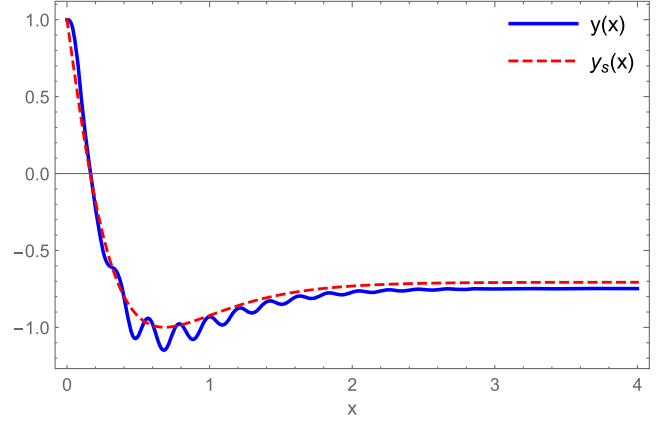


FIG. 18. Comparison of exact and adiabatic solution for the equation $\ddot{y} + 3\dot{y} + 200 \sin(30x)e^{-3x}y = 0$, $y(0) = 1$, $\dot{y}(0) = 0$. Using the adiabatic or IR approximation, we solved the reduced equation $\ddot{y} + 3\dot{y} + (200/30)^2 e^{-3x}y/2 = 0$, $y(0) = 1$, $\dot{y}(0) = -200/30$. Note that the initial conditions are modified.

$$\ddot{y}_f + A\beta(t) \cos(ft)y_s \sim 0$$

and by assuming a slow-varying envelope function $\beta(t)$ we obtain up to a leading order

$$y_f \sim \frac{A}{\Omega^2} \beta(t) \cos(ft)y_s.$$

Note that $|y_f/y_s| \sim O(A/f^2)$ and sets the scale of the UV component compared to IR. Next, we substitute the UV solution into our original differential equation and integrate out the UV scale over one time period,

$$\ddot{y}_s + \frac{A^2}{2f^2} \beta^2(t)y_s \sim 0. \quad (\text{C2})$$

The above differential equation governs the dynamics of the IR component subject to the initial conditions $y_s(t_0) = y(t_0)$ and $\dot{y}_s(t_0) = \dot{y}(t_0) - \dot{y}_f(t_0)$. By defining $\delta = A/f^2$, we note that if $\delta \ll 1$, then the above UV and IR treatment is also valid up to $O(\delta)$. Figure 18 gives plots of $y(x)$ and $y_s(x)$ obtained by solving the exact ODE $\ddot{y} + 3\dot{y} + 200 \sin(30x)e^{-3x}y = 0$, $y(0) = 1$, $\dot{y}(0) = 0$, and its adiabatically reduced form respectively.

APPENDIX D: FLAT DEVIATION ξ

The quantity $\xi = \phi_+ \phi_- - F^2$ defines a deviation from the flat direction. This is a crucial measure as it controls the strongly coupled dynamics of the two fields. To obtain a differential equation for ξ we start with the background field equation (18). We multiply the two equations by ϕ_- and ϕ_+ respectively and add them together to obtain

$$-2\dot{\phi}_+\dot{\phi}_- + \partial_T^2(\phi_+\phi_-) + 3\partial_T(\phi_+\phi_-) + (c_+ + c_- + \phi_-^2 + \phi_+^2)\phi_+\phi_- - F^2(\phi_-^2 + \phi_+^2) = 0,$$

which yields an effective equation for the flat deviation

$$\ddot{\xi} + 3\dot{\xi} + (\tilde{M}_{11}^2 + \tilde{M}_{22}^2)\xi = -(c_+ + c_-)F^2 + 2\dot{\phi}_+\dot{\phi}_-, \quad (\text{D1})$$

where \tilde{M}_{ij}^2 are the elements of the \tilde{M}^2 matrix. This is an interesting equation in that apart from the kinetic mixing terms on the rhs, the equation for ξ has been made to “look” linear, although it certainly is not because of $\tilde{M}_{11}^2 + \tilde{M}_{22}^2$. Consider an expansion about a neighborhood of T_m defined to be the zero of $\dot{\phi}_+$:

$$\dot{\phi}_+(T_m) = 0. \quad (\text{D2})$$

In that neighborhood, the solution must behave as

$$\phi_+(T) = \phi_+(T_m) + \frac{1}{2}\ddot{\phi}_+(T_m)(T - T_m)^2 + \dots \quad (\text{D3})$$

Since T_m comes $O(1/F)$ time after T_c while ϕ_- has been increasing beyond F while ϕ_+ has been decreasing toward

$\phi_+(T_m)$, we can approximate that ϕ_- has a Taylor expansion in time:

$$\phi_-(T) = \phi_-(T_m) + \dot{\phi}_-(T_m)(T - T_m) + \frac{1}{2}\ddot{\phi}_-(T_m)(T - T_m)^2 + \dots \quad (\text{D4})$$

We then find

$$\dot{\phi}_+(T) = \ddot{\phi}_+(T_m)(T - T_m) + \frac{1}{2}\dddot{\phi}_+(T_m)(T - T_m)^2 + \dots, \quad (\text{D5})$$

$$\dot{\phi}_-(T) = \dot{\phi}_-(T_m) + \ddot{\phi}_-(T_m)(T - T_m) + \frac{1}{2}\dddot{\phi}_-(T_m)(T - T_m)^2 + \dots, \quad (\text{D6})$$

yielding

$$\dot{\phi}_+\dot{\phi}_- = \ddot{\phi}_+(T_m)\dot{\phi}_-(T_m)(T - T_m) + O[(T - T_m)^2]. \quad (\text{D7})$$

We also know

$$\tilde{M}_{11}^2 + \tilde{M}_{22}^2 = c_+ + c_- + [\phi_-(T_m) + \dot{\phi}_-(T_m)(T - T_m) + \dots]^2 + \left[\phi_+(T_m) + \frac{1}{2}\ddot{\phi}_+(T_m)(T - T_m)^2 + \dots\right]^2 \quad (\text{D8})$$

$$= c_+ + c_- + \phi_-^2(T_m) + \phi_+^2(T_m) + 2\phi_-(T_m)\dot{\phi}_-(T_m)(T - T_m) + O[(T - T_m)^2]. \quad (\text{D9})$$

Keeping to zeroth order in $T - T_m$, we put into Eq. (D1) the zeroth order terms in Eqs. (D7) and (D9). The resulting equation (D1) has a solution in the vicinity of T_m ,

$$\xi = -Ae^{-\frac{3}{2}(T-T_m)} \cos(\Omega(T_m)(T - T_m)) - \frac{(c_+ + c_-)F^2}{\Omega(T_m)^2} + O((T - T_m)^3\ddot{\phi}_+(T_m)\dot{\phi}_-(T_m)), \quad (\text{D10})$$

$$\Omega(T_m) \equiv \sqrt{\tilde{M}_{11}^2(T_m) + \tilde{M}_{22}^2(T_m) - \frac{9}{4}}. \quad (\text{D11})$$

For the remainder of our discussion, we will consider the following approximate expression for the flat deviation with a constant amplitude A and a slow-varying time-dependent frequency

$$\xi = -Ae^{-\frac{3}{2}(T-T_m)} \cos\left(\int_{T_m}^T \Omega(t)dt\right) - \frac{(c_+ + c_-)F^2}{\Omega(T)^2}. \quad (\text{D12})$$

Flat deviations of $O(F^2)$ occur close to a zero crossing of ϕ_+ characterized by a strong nonlinear interaction between the two background fields. After transition, when

the background fields are settling to their minima, the frequency of flat deviation is $\sim O(F)$. As the fields initially start out along the flat direction, $\xi \approx 2\dot{\phi}_+\dot{\phi}_-/\phi_+^2 \sim O(\dot{\phi}_-/\phi_+) < 1$ is negligible since $\phi_+ \gg \phi_-$. When the fields reach close to the transition, the $2\dot{\phi}_+\dot{\phi}_-$ term causes the fields to deviate away from the flat direction. Later when the fields have settled to their minima, the flat deviation tends to

$$-\frac{(c_+ + c_-)F^2}{\tilde{M}_{11}^2 + \tilde{M}_{22}^2} \approx -\sqrt{c_+c_-}. \quad (\text{D13})$$

The kind of dynamic behavior described above can lead to resonance which is characterized by a significant flat deviation $\gtrsim O(0.1F^2)$, as shown in Fig. 19.

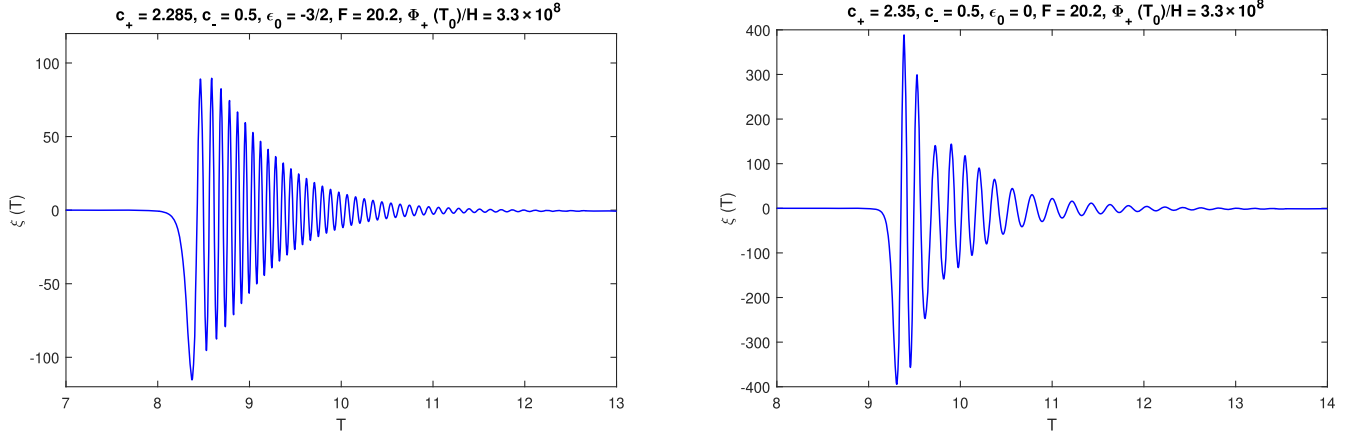


FIG. 19. Comparison of numerical solutions to flat deviation $\xi(T)$ after transition for $c_+ = 2.285$, $\epsilon_0 = -3/2$ (left panel) and $c_+ = 2.35$, $\epsilon_0 = 0$ (right panel) highlighting the resonant cases. All other parameters were set at their fiducial values P_A of Fig. 5.

APPENDIX E: UV AND IR DECOMPOSITION OF THE BACKGROUND FIELDS

Post transition, the background fields are strongly coupled through the interaction term $\xi\phi_{\pm}$ as shown in the equations

$$\ddot{\phi}_+ + 3\dot{\phi}_+ + c_+\phi_+ + \xi\phi_- = 0, \quad (\text{E1})$$

$$\ddot{\phi}_- + 3\dot{\phi}_- + c_-\phi_- + \xi\phi_+ = 0, \quad (\text{E2})$$

where ξ is an oscillating function given in Eq. (D12). The dynamics of the coupled system post transition can be understood in terms of a UV and IR decomposition detailed in Appendix C. If the frequency of the oscillating function ξ is much larger than the root of its amplitude, the system exhibits a hierarchy between the UV and IR states. We may then integrate out the UV degree of freedom and retain the IR components to describe the adiabatic behavior of the coupled system. In principle we can write

$$\phi_{\pm} \approx \phi_{\pm s} + \phi_{\pm f}, \quad (\text{E3})$$

where the subscripts s , f represent the slow (IR) and fast (UV) components of the fields.

From Appendix C and assuming $A/\Omega_s^2 \ll 1$ (which we will justify below), we can write down an approximate solution for the UV component of the ϕ_{\pm} fields as

$$\begin{aligned} \phi_{+f} &\approx -\frac{A}{\Omega^2} e^{-\frac{3}{2}(T-T')} \sin(f(T))\phi_{-s}, \\ \phi_{-f} &\approx -\frac{A}{\Omega^2} e^{-\frac{3}{2}(T-T')} \sin(f(T))\phi_{+s}, \end{aligned} \quad (\text{E4})$$

where we have used Eq. (D12) in place of ξ [with a time-dependent frequency term $f(T) = \int_T^T \Omega(t) dt$] and switched the cosine function in Eq. (D12) to a sine for convenience. In terms of the UV and IR components we can write the flat deviation as

$$\xi = \phi_+\phi_- - F^2 \quad (\text{E5})$$

$$\approx \phi_{+s}\phi_{-s} + \phi_{+f}\phi_{-s} + \phi_{+s}\phi_{-f} + \phi_{+f}\phi_{-f} - F^2. \quad (\text{E6})$$

Meanwhile from Eq. (E4) we infer that

$$\xi \approx -Ae^{-\frac{3}{2}(T-T')} \sin(f(T)) \approx \phi_{+f}\phi_{-s} + \phi_{+s}\phi_{-f}, \quad (\text{E7})$$

subject to the approximation $\Omega^2 \approx \phi_{+s}^2 + \phi_{-s}^2 \equiv \Omega_s^2$. Thus, we will approximately take the frequency squared of the ξ function as the sum of the squares of the IR components of the background fields. Since the UV components are smaller in amplitude compared to IR, we obtain an approximate relationship between the IR components of the background fields,

$$\phi_{+s}\phi_{-s} \approx F^2 - O(\phi_{+f}\phi_{-f}). \quad (\text{E8})$$

This is an important result which indicates that if the background fields can be factorized into UV and IR components, then the IR components continue to follow the flat direction.

Post transition, $|\phi_-|$ begins to increase due to a positive velocity of $O(F^2)$ and becomes dominant compared to a decreasing $|\phi_+|$. During this time, the UV integrated equation of motion for the IR component of the dominant ϕ_- field is given below,

$$\ddot{\phi}_{-s} + 3\dot{\phi}_{-s} + c_-\phi_{-s} + \frac{A^2}{2\Omega_s^2} e^{-3(T-T_2)} \phi_{-s} + \sqrt{c_+c_-} \phi_{+s} \approx 0, \quad (\text{E9})$$

while the smaller ϕ_{+s} field is obtained through the flat direction condition $\phi_{+s}\phi_{-s} \approx F^2$. Note that $\Omega_s^2 \approx \phi_{+s}^2 + \phi_{-s}^2$ is a function of the background fields highlighting the nonlinearity of the above equation. However, to obtain an analytic solution we will consider an average value for the

parameter Ω_s over a half-oscillation of ϕ_{-s} (since ϕ_{-s} increases up to a maximum and then falls back toward F) such that a general solution to the above damped oscillator equation for a constant average $\bar{\Omega}$ is given as (during the time when the term $\sqrt{c_-c_+}\phi_{+s}$ is not appreciable)

$$\phi_{-s} = e^{-\frac{3}{2}(T-T_2)} \left(c_1 J_{n_1} \left(\frac{A\sqrt{2}}{3\bar{\Omega}} e^{-\frac{3}{2}(T-T_2)} \right) + c_2 J_{-n_1} \left(\frac{A\sqrt{2}}{3\bar{\Omega}} e^{-\frac{3}{2}(T-T_2)} \right) \right), \quad (\text{E10})$$

where

$$n_1 = \sqrt{1 - 4c_-/9}, \quad (\text{E11})$$

$$c_{1,2} = \frac{\mp \pi}{2 \sin(\pi n_1)} \left(\phi_{-s}(T_2) \frac{A\sqrt{2}}{3\bar{\Omega}} J'_{\mp n_1} \left(\frac{A\sqrt{2}}{3\bar{\Omega}} \right) + (\phi_{-s}(T_2) + 2\dot{\phi}_{-s}(T_2)/3) J_{\mp n_1} \left(\frac{A\sqrt{2}}{3\bar{\Omega}} \right) \right) \quad (\text{E12})$$

for

$$\phi_{-s}(T_2) \approx \phi_{-}(T_2), \quad (\text{E13})$$

$$\dot{\phi}_{-s}(T_2) \approx \dot{\phi}_{-}(T_2) - \frac{\xi \phi_{+}}{\phi_{-}} \Big|_{T_2}, \quad (\text{E14})$$

where $\phi_{-}(T)$ properties near T_2 can be obtained from Eq. (163). Meanwhile, the ϕ_{+s} field is given by the flat direction

$$\phi_{+s} \approx \frac{F^2}{\phi_{-s}}. \quad (\text{E15})$$

Since Ω is a time-dependent function of the background fields, we apply a seminumeric approach to estimate an average value of Ω between T_2 and the time T_* when $\phi_{-s}(T_*) \approx 4/3\phi_{-\min}$ for $c_+ > c_-$. This choice of T_* allows us to consider both the situations where the two background fields may either cross each other again after T_c or not. The procedure involves matching the analytical solution in Eq. (E10) to the numerical results for the fit parameter $\bar{\Omega}$. Through this procedure we obtain an empirical fit expression for $\bar{\Omega}$ as a function of α and F :

$$\bar{\Omega} \approx 2.05F + \frac{0.1327F + 0.0454F^2}{1 + \exp(7.86(\alpha - \alpha_0))}, \quad (\text{E16})$$

where

$$\alpha_0 \equiv 0.7442 - 0.0008F. \quad (\text{E17})$$

When $\sqrt{2}A/(3\bar{\Omega})e^{-3/2(T-T_2)} \gg |3/4 - 4c_-/9|$, the above solution has an oscillating behavior with a maximum frequency f_{IR} ,

$$f_{\text{IR}} \approx \frac{\sqrt{2}A}{3\bar{\Omega}}. \quad (\text{E18})$$

Within our parametric region of interest, the amplitude satisfies $A < F^2$ from Eq. (173) imposed by $\alpha \lesssim \alpha_U$. Since the transition occurs close to F , the two fields oscillate over the equilibrium scale F such that $\Omega_s \approx \sqrt{\phi_{+s}^2 + \phi_{-s}^2} \geq \sqrt{2}F$ with an average value of approximately $O(2F)$ at T_2 . Therefore, we see the self-consistency of the assumption that $A/\Omega_s^2 \ll 1$ for $T \geq T_2$. Between T_c and T_2 , the system of background fields can be given by the cubic-polynomial solution. Also, the IR fields can oscillate momentarily with a frequency $f_{\text{IR}} \sim O(0.1F)$, while the UV scales oscillate with frequency $\Omega_s \sim O(F)$. Therefore, the hierarchy between the two scales is clearly established.

In summary, prior to transition the fields are best described via primary frequency $\omega = \sqrt{c_+ - 9/4}$. After

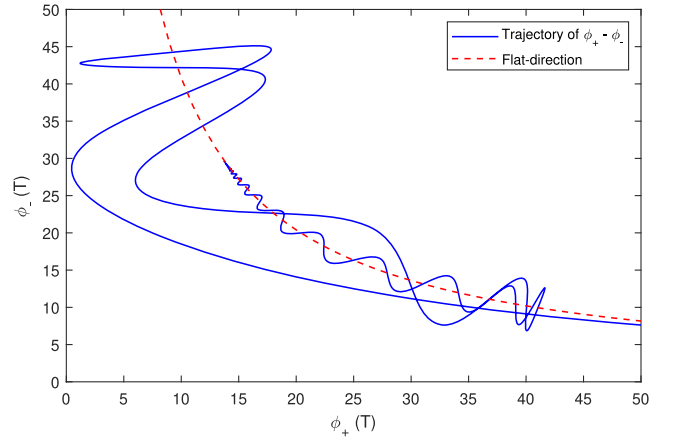
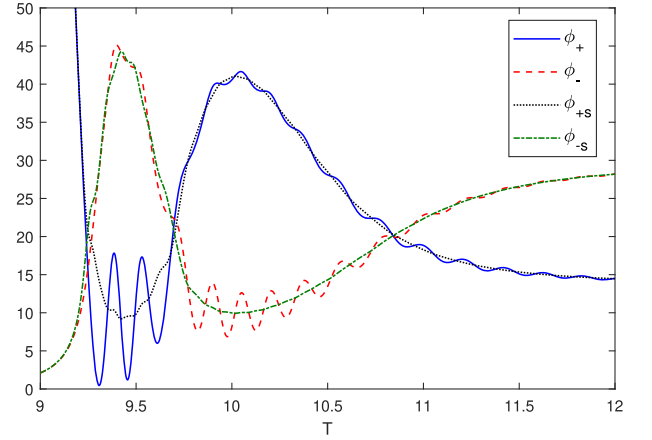


FIG. 20. Plots showing UV and IR components of the background fields ϕ_{\pm} for $c_+ = 2.35$ where the curves for ϕ_{\pm} have been computed numerically by solving Eqs. (17) and (18). The IR components $\phi_{\pm s}$ have been computed by subtracting $\phi_{\pm f}$ of Eq. (E4) from the numerically computed ϕ_{\pm} . On the right, the trajectory of the background fields clearly highlights the deviations away from the flat direction. All the parameters have been set to the P_A set used in Fig. 5.

transition, we can separate the fields into UV and IR components as long as $A/\Omega_s^2 \ll 1$. As $T \rightarrow T_\infty$, the UV component decays away and the IR components settle to the minima. Figure 20 highlights the above conclusions by showing UV and IR components of the background fields ϕ_\pm for $c_+ = 2.35$ with all the other parameters set to the P_A set used in Fig. 5.

APPENDIX F: LIGHTEST EIGENVECTOR

We will now study the lightest mass eigenvector e_1 corresponding to the lightest mass eigenvalue and derive an analytical expression for $(\partial_T e_1)^2$. We begin by defining the lightest mass eigenvector,

$$e_1 = \begin{bmatrix} e_{11} \\ e_{21} \end{bmatrix}, \quad (\text{F1})$$

where the column matrix elements are

$$\begin{aligned} e_{11} &= \frac{e}{\sqrt{e^2 + 1}} \approx \frac{-\phi_+}{\sqrt{\phi_+^2 + \phi_-^2}}, \\ e_{21} &= \frac{1}{\sqrt{e^2 + 1}} \approx \frac{\phi_-}{\sqrt{\phi_+^2 + \phi_-^2}}, \end{aligned} \quad (\text{F2})$$

with the definition

$$e = \frac{1}{2F^2} \left(\tilde{M}_{11}^2 - \tilde{M}_{22}^2 - \sqrt{(\tilde{M}_{22}^2 - \tilde{M}_{11}^2)^2 + 4F^4} \right).$$

We would like to evaluate the derivative squared term $(\partial_T e_1)^2 = (\partial_T e_{11})^2 + (\partial_T e_{21})^2$. Using the definitions from above, we note that $\partial_T e_{11} = (\partial_T e)/(e^2 + 1)^{3/2}$ and $\partial_T e_{21} = \partial_T e(-e/(e^2 + 1)^{3/2})$ so that $\dot{e}_1 \cdot \dot{e}_1 = \dot{e}^2/(e^2 + 1)^2$. By defining $g = \tilde{M}_{11}^2 - \tilde{M}_{22}^2$ we expand $\dot{e}_1 \cdot \dot{e}_1$,

$$\dot{e}_1 \cdot \dot{e}_1 = \dot{g}^2 \left(\frac{e^2}{(e^2 + 1)^2 g^2 + 4F^4} \right), \quad (\text{F3})$$

with

$$\dot{g} = 2\dot{\phi}_- \phi_- - 2\dot{\phi}_+ \phi_+. \quad (\text{F4})$$

Thus, the $\dot{e}_1 \cdot \dot{e}_1$ peak amplitude is related to the relative velocity of the two fields as they cross each other. The peak is maximized if the two fields approach from opposite directions, thus maximizing the relative velocity. Upon substituting the analytical form of \dot{g} into Eq. (F3) and solving we obtain that the first maxima close to T_c occurs when the $|\phi_+|$ field is approximately F . The maximum amplitude is given as

$$(\dot{e}_1 \cdot \dot{e}_1)_{\max} \approx \dot{g}^2 \left(\frac{e^2}{(e^2 + 1)^2 g^2 + 4F^4} \right) \Big|_{\phi_+ \rightarrow F}.$$

As $|\phi_+| \rightarrow F$, we have $-F^2 \leq g < 0$ so that we can expand in terms of $(g + F^2)/F^2 \ll 1$, which simplifies $(\dot{e}_1 \cdot \dot{e}_1)_{\max}$,

$$\begin{aligned} (\dot{e}_1 \cdot \dot{e}_1)_{\max} &\approx \left(\frac{\dot{g}}{5F^2} \right)^2 \left(1 + \frac{4}{5} \left(\frac{g + F^2}{F^2} \right) + \frac{2}{25} \left(\frac{g + F^2}{F^2} \right)^2 \right. \\ &\quad \left. - \frac{28}{125} \left(\frac{g + F^2}{F^2} \right)^3 \right) \Big|_{\phi_+ \rightarrow F}, \end{aligned} \quad (\text{F5})$$

which has a limiting case

$$\lim_{\alpha \gg 1} (\dot{e}_1 \cdot \dot{e}_1)_{\max} \rightarrow \frac{4}{25} F^2 \alpha^2. \quad (\text{F6})$$

Using the above analytical expressions, we present a second order polynomial fit in terms of parameter α for the Eq. (F5) in the range [0.25, 1.5]:

$$\begin{aligned} (\dot{e}_1 \cdot \dot{e}_1)_{\max} &\approx F^2 (-0.0030 + 0.2156\alpha + 0.1779\alpha^2), \\ \alpha &\in [0.25, 1.5]. \end{aligned} \quad (\text{F7})$$

As the ϕ_+ field rapidly rolls down from the Plank scale, the first peak $(\dot{e}_1 \cdot \dot{e}_1)$ peak occurs slightly before transition and is characterized by the dominant $\omega = \sqrt{c_+ - 9/4}$ frequency. After transition, the ϕ_\pm fields can be divided into the UV and IR components. When the jump ETSP in Eq. (E9) is significant at T_2 , it leads to an $O(0.1F)$ frequency oscillations of the IR fields (see Appendix E) such that the fields cross again after transition (also characterized by the zeros of $g \approx \phi_-^2 - \phi_+^2$). Quantitatively, this is equivalent to $\phi_{-s} \rightarrow F$ since $\phi_{+s} \approx F^2/\phi_{-s}$. Thus, we can obtain the approximate location of the second crossing of the background fields by solving Eq. (E10) for the time T_3 when $\phi_{-s}(T_3) = F$.

Since additional crossings require a significant jump ETSP, we begin with the Eq. (E10) for the ϕ_{-s} background field and evaluate an approximate condition for the background fields to cross after transition. As we are interested in cases where the crossings are caused by the jump ETSP, we will neglect the c_- term in Eq. (E9). Hence, we consider the following equation:

$$\ddot{\phi}_{-s} + 3\dot{\phi}_{-s} + \frac{A^2}{2\Omega^2} e^{-3(T-T_2)} \phi_{-s} \approx 0, \quad (\text{F8})$$

which has the general solution

$$\begin{aligned} \phi_{-s}(T \geq T_2) &\approx e^{-\frac{3}{2}(T-T_2)} [c'_1 J_1(m e^{-\frac{3}{2}(T-T_2)}) \\ &\quad + c'_2 Y_1(m e^{-\frac{3}{2}(T-T_2)})], \end{aligned} \quad (\text{F9})$$

where the primed coefficients $c'_{1,2}$ are obtained similar to the $c_{1,2}$ below Eq. (E10) and $m = \sqrt{2A}/(3\bar{\Omega})$ is a function of α .

As $T \rightarrow T_\infty$, we look for the minimum value of m such that $\phi_{-s}(T > T_2) = F$. Hence, we equate

$$\lim_{T \rightarrow T_\infty} \phi_{-s}(T \geq T_2) \approx \phi_{-s}(T_2) J_1'(m) + \frac{(\phi_{-s}(T_2) + 2\dot{\phi}_{-s}(T_2)/3)}{m} J_1(m) = F. \quad (\text{F10})$$

Since $\dot{\phi}_{-s}(T_2) \sim O(.5F^2) \gg \phi_{-s}(T_2) \sim O(F)$, we reduce the above expression to

$$\frac{3}{F} \approx \frac{J_1(m)}{m}. \quad (\text{F11})$$

Equation (F11) gives us an approximate minimum value of m such that the two background fields cross each other after T_c . For $c_- \ll 1$ and $F \gg 1$, we find that the minimum value of m saturates to about

$$m = z_1 \approx 3.8, \quad (\text{F12})$$

where $J_1(z_1) = 0$. The term A in Eq. (F11) can be evaluated using the nonperturbative cubic-polynomial expansion for the background fields from Eqs. (67) and (68) around T_c . The minimum value of α that satisfies the conditional equality in Eq. (F11) is defined as α_2 . It corresponds to a parametric cutoff such that for $\alpha \gtrsim \alpha_2$, the background fields cross each other again after T_c . For $F = 20.2$ (corresponding to the fiducial parameter set P_A), we obtain $\alpha_2 \approx 0.87$. Similarly, for a much larger value of $F = 100$, we obtain $\alpha_2 \approx 0.6$, highlighting that α_2 reduces with F . If the resonance amplitude A is large enough, the background fields can cross each other more than once after T_c . This corresponds to the situation where

$$m \gtrsim z_2, \quad (\text{F13})$$

where z_2 corresponds to the second zero of $J_1(z)$. Further, we remind the reader that each crossing of the background fields corresponds to a $(\dot{e}_1)^2$ peak which is modeled as a $-V_i$ dip within our numerical mass model in Eq. (101). Since we limit ourselves to just two dips in this paper, we will consider only those cases where $\alpha \lesssim \alpha_3$.

For $\alpha \gtrsim \alpha_2$ cases, the $-V_3$ dip within our mass model can be evaluated using Eq. (F3) wherein the peak amplitude of the $\dot{e}_1 \cdot \dot{e}_1$ function around T_3 is evaluated by substituting $\phi_{\pm s}$ into $g \approx \phi_-^2 - \phi_+^2$ using the solution provided in Eqs. (E10) and (E15). Meanwhile, the maximum amplitude of these peaks located close to the zeros of g requires an evaluation of \dot{g} as observed in Eq. (F3). In terms of the IR and UV components, we rewrite \dot{g} as

$$\dot{g} \approx \dot{g}_s + \dot{g}_{sf} + \dot{g}_{fs} + \dot{g}_f, \quad (\text{F14})$$

where we identify $\dot{g}_s \approx 2(\phi_{-s}\dot{\phi}_{-s} - \phi_{+s}\dot{\phi}_{+s})$, $\dot{g}_f \approx 2(\phi_{-f}\dot{\phi}_{-f} - \phi_{+f}\dot{\phi}_{+f})$, $\dot{g}_{fs} \approx 2(\phi_{-f}\dot{\phi}_{-s} - \phi_{+f}\dot{\phi}_{+s})$, and $\dot{g}_{sf} \approx 2(\phi_{-s}\dot{\phi}_{-f} - \phi_{+s}\dot{\phi}_{+f})$. Using Eqs. (E4), one can show that the mixed terms \dot{g}_{fs} and \dot{g}_{sf} cancel out due to an accidental symmetry $\phi_\pm \rightarrow -\phi_\pm$ that exists in the potential governing ϕ_\pm , while the amplitude of the first derivative of the UV component is given as

$$\dot{g}_f|_{T \sim T_3} \approx \partial_T(\phi_{-f}^2 - \phi_{+f}^2)|_{T \sim T_3} \approx \left(\frac{A^2 e^{-3(T_3 - T_c)}}{\Omega_s^3} \right) g_s + \left(\frac{A e^{-3/2(T_3 - T_c)}}{\Omega_s^2} \right)^2 \dot{g}_s. \quad (\text{F15})$$

Up to a linear order in the Taylor expansion, we can approximate g_s in the vicinity of T_3 as

$$g_s(T) \approx \dot{g}_s(T_3)(T - T_3). \quad (\text{F16})$$

Therefore, including the additional contributions from the UV term g_f , we can approximate the $(\dot{e}_1^2)_{T \sim T_3}$ peak in the vicinity of T_3 using

$$\dot{g}(T \sim T_3) \approx \dot{g}_s(T_3) \left(1 + \frac{A^2 e^{-3(T_3 - T_c)}}{\Omega_s^4} (1 + \Omega_s(T - T_3)) \right) \quad (\text{F17})$$

within Eq. (F3). Through fitting, we find that up to a 20% error, the above evaluation procedure can be approximated by the following simplified expression:

$$(\dot{e}_1^2)_{T=T_j} \approx \begin{cases} (\dot{e}_1^2)_{\max} e^{-3(T_j - T_c)}, & \frac{A e^{-3/2(T_j - T_c)}}{2F^2} > 0.15, \\ (\dot{e}_1^2)_{\max} \left(\frac{\dot{g}_s(T_j)}{\dot{g}_s(T_c)} \right)^2, & \frac{A e^{-3/2(T_j - T_c)}}{2F^2} < 0.15, \end{cases} \quad (\text{F18})$$

where T_j refers to the time when the two background fields cross each other again after T_c and $\dot{g}_s(T_c)$ are evaluated from the cubic-polynomial solution for the background fields in Eqs. (67) and (68). These peaks are lower in magnitude due to the Hubble friction, as shown in Fig. 21.

Next we note that Eq. (F5) can be qualitatively understood by the following factorization:

$$\dot{e}_1 \cdot \dot{e}_1 \sim \sum_{nm} d_{nm}(\phi_+, \phi_-) \frac{\dot{\phi}_n \dot{\phi}_m}{F^2}, \quad (\text{F19})$$

where the coefficients d_{nm} are dimensionless and order $O(1)$. The width Δ of a $\dot{e}_1 \cdot \dot{e}_1$ peak is characterized by

$$\Delta \propto \frac{\Delta \phi_{\max}}{\dot{\phi}_{\max}}, \quad (\text{F20})$$

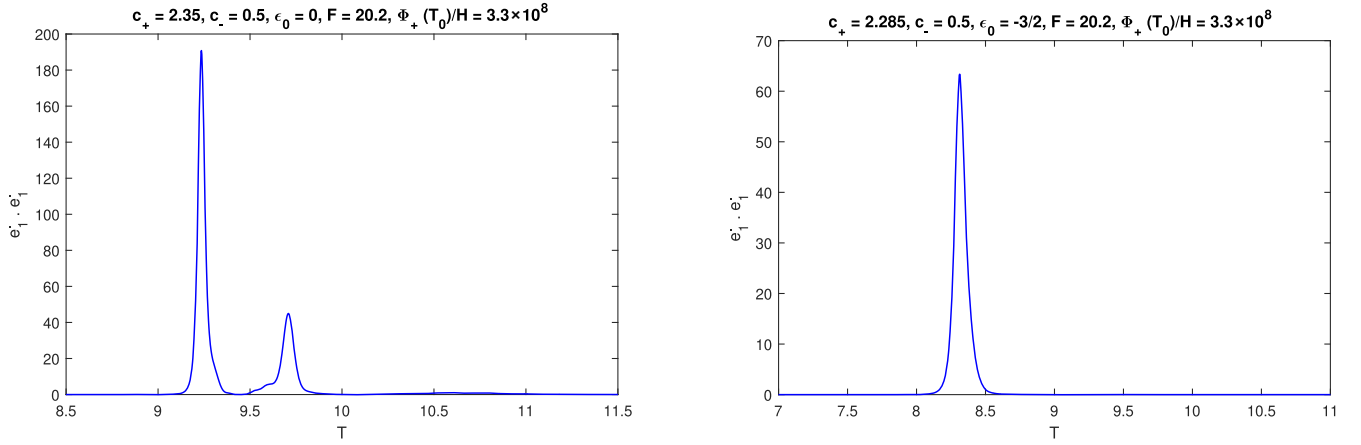


FIG. 21. Plots depicting peaks of $\dot{e}_1 \cdot \dot{e}_1$ [Eq. (F3)] for $c_+ = 2.35$, $\epsilon_0 = 0$ (left panel) and $c_+ = 2.285$, $\epsilon_0 = -3/2$ (right panel). All the parameters have been set to the P_A set used in Fig. 5.

where ϕ_{\max} is the field at the maximum of $\dot{e}_1 \cdot \dot{e}_1$ which gives us

$$\frac{\Delta\phi_{\max}}{\phi_{\max}} \sim \frac{\Delta\phi_{\max} \sqrt{\text{larger eigenvalue } d_{nm}(\phi_+, \phi_-)}}{\sqrt{F^2 \dot{e}_1 \cdot \dot{e}_1}}. \quad (\text{F21})$$

We shall therefore consider the following repatriation for the width Δ :

$$\Delta \approx \frac{r_{\Delta}}{\sqrt{\dot{e}_1 \cdot \dot{e}_1}}, \quad (\text{F22})$$

where r_{Δ} takes the following form:

$$r_{\Delta} \approx \frac{\Delta\phi_{\max} \sqrt{\text{larger eigenvalue } d_{nm}(\phi_+, \phi_-)}}{F}. \quad (\text{F23})$$

Therefore, r_{Δ} has parametric dependence on $\Delta\phi_{\max}$ and $\sqrt{\text{larger eigenvalue } d_{nm}(\phi_+, \phi_-)}$. As α increases, $\Delta\phi_{\max}$ must also increase due to increasing resonance amplitude. On the other hand, the corresponding value of ϕ_- at the location of the peak reduces monotonically with an increasing α , which results in a smaller $\sqrt{\text{larger eigenvalue } d_{nm}(\phi_+, \phi_-)}$. Within the parametric region ($0.25 \lesssim \alpha \lesssim 1$), the two competing behaviors are equally important and tend to cancel each other out such

that within the region of our interest we can approximate $r_{\Delta} \approx 0.72$ so that the width of the $\dot{e}_1 \cdot \dot{e}_1$ peaks are approximately given as $\Delta \approx 0.72/\sqrt{\dot{e}_1 \cdot \dot{e}_1}$ within 10% accuracy. Using Eq. (F7) for the $(\dot{e}_1 \cdot \dot{e}_1)_{\max}$ into Eq. (F22), we obtain the following linear expression in α for the width of the first $(\dot{e}_1 \cdot \dot{e}_1)$ dip:

$$\Delta_{(\dot{e}_1 \cdot \dot{e}_1)_{\max}} \approx \frac{(2.93 - 1.86\alpha)}{F}. \quad (\text{F24})$$

In general, the width of these Gaussian-like peaks can also be evaluated by taking the ratio of the total area under the peak to its maximum amplitude.

APPENDIX G: LIGHTER MASS EIGENVALUE m_1^2

In this section, we will study the variation of lightest mass eigenvalue over time. The lightest eigenvalue of the mass matrix \tilde{M}^2 is given by the expression

$$m_1^2 = \frac{\tilde{M}_{11}^2 + \tilde{M}_{22}^2}{2} \left(1 - \sqrt{1 + 4 \frac{F^4 - \tilde{M}_{11}^2 \tilde{M}_{22}^2}{(\tilde{M}_{22}^2 + \tilde{M}_{11}^2)^2}} \right). \quad (\text{G1})$$

In terms of $\Omega^2 = \tilde{M}_{11}^2 + \tilde{M}_{22}^2$ and $\xi = \phi_+ \phi_- - F^2$ we rewrite Eq. (G1) as

$$m_1^2 = \frac{\Omega^2}{2} \left(1 - \sqrt{1 - 4 \left(\frac{\xi}{\Omega^2} \right)^2 - 8 \frac{F^2}{\Omega^2} \left(\frac{\xi}{\Omega^2} \right) - 4 \frac{c_+ \phi_+^2 + c_- \phi_-^2 + c_- c_+}{\Omega^4}} \right).$$

During the early phase when $|\phi_+| \gg F$ and any transient oscillations $\phi_-^{\text{transient}}$ of ϕ_- are negligible i.e., $\phi_-^{\text{transient}} \ll \phi_-^{(0)}$, m_1^2 reduces to

$$m_1^2 \sim \frac{1}{2} \left(\tilde{M}_{11}^2 + \tilde{M}_{22}^2 - (\tilde{M}_{22}^2 - \tilde{M}_{11}^2) - \frac{2F^4}{\tilde{M}_{22}^2 - \tilde{M}_{11}^2} \right),$$

$$\sim c_+ + O\left(F^2 \frac{\phi_-^{\text{transient}}}{\phi_+}\right). \quad (\text{G2})$$

As the fields then approach transition, the zero order approximate perturbative solution $\phi_{\pm}^{(0)}$ is no longer valid. The lighter mass eigenvalue transitions from c_+ to a negative dip. Post this dip, m_1^2 oscillates due to the resonance before settling down to zero. As explained in Appendix E, the background fields post $-V_1$ dip can be factorized in terms of the UV and IR components. Using these components we can write Ω^2 as

$$\Omega^2 \approx \phi_+^2 + \phi_-^2$$

$$\approx \phi_{+s}^2 + \phi_{-s}^2 + \phi_{+f}^2 + \phi_{-f}^2 + 2\phi_{+s}\phi_{+f} + 2\phi_{-s}\phi_{-f}$$

$$\approx \Omega_s^2 + \frac{4F^2}{\Omega_s^2} \xi + O(\Omega_f^2) \quad (\text{G3})$$

such that we can factor out the resonant UV oscillations over the slow-varying Ω_s^2 background.

Next we substitute the above factorization for Ω^2 into Eq. (G2) and expand m_1^2 in powers of $\delta = \xi/\Omega_s^2$,

$$m_1^2 \approx \frac{c_- \phi_-^2 + c_+ \phi_+^2}{\Omega_s^2} + 2F^2 \left[\delta + \left(\frac{\Omega_s^2}{2F^2} - \frac{2F^2}{\Omega_s^2} \right) \delta^2 \right. \\ \left. + \frac{1}{2} \left(\frac{\Omega_s}{F} - \frac{4F^3}{\Omega_s^3} \right)^2 \delta^4 + O(\delta^6) \right].$$

Within the parametric region of interest where $|\delta| \ll 1$, we drop all terms of $O(\delta^3)$ and higher such that

$$m_1^2(T) \approx 2F^2 \left[\delta + \left(\frac{\Omega_s^2}{2F^2} - \frac{2F^2}{\Omega_s^2} \right) \delta^2 \right] + \frac{c_- \phi_-^2 + c_+ \phi_+^2}{\Omega_s^2}. \quad (\text{G4})$$

The above expression highlights that the mass eigenvalue thus oscillates in tandem with the flat-deviation oscillations before settling down to zero. The expansion leading to Eq. (G4) is appropriate as long as the term $\xi/(\phi_{-s}^2 + \phi_{+s}^2) \lesssim O(0.2)$. From Eq. (173) we infer that $|\xi| \lesssim F^2$ for $\alpha \leq 1$, meanwhile $\phi_-(T_2) \approx 2F$ and hence the expansion term $\xi/(\phi_{-s}^2 + \phi_{+s}^2)$ tends to ~ 0.2 as $\alpha \rightarrow 1 \equiv \alpha_U$. To the contrary, if the two fields tend to $O(1)$ momentarily, the above expansion breaks down. However, the lighter mass eigenvalue in those conditions tends to $-F^2$. This situation arises when the trajectory of the two fields tends to be chaotic and unstable, which is outside the scope of our parametric region.

APPENDIX H: BUILDING THE NUMERICAL MODEL

In Appendix G we obtained an approximate expression for the lighter mass eigenvalue in the limit $\xi/\Omega_s^2 \ll 1$. Next we substitute for the flat deviation ξ from Eq. (D12) into Eq. (G4),

$$m_1^2(T) \approx 2F^2 \left[\frac{\xi}{\Omega_s^2} + \left(\frac{\Omega_s^2}{2F^2} - \frac{2F^2}{\Omega_s^2} \right) \left(\frac{\xi}{\Omega_s^2} \right)^2 \right] + m_B^2(T)$$

$$\forall \frac{\xi}{\Omega_s^2} \ll 1, \quad (\text{H1})$$

where the slow-varying background term $-(c_+ + c_-)F^2/\Omega_s^2$ of ξ from Eq. (D12) has been absorbed within $m_B^2(T)$ such that

$$m_B^2(T) \approx \frac{c_- \phi_{-s}^2 + c_+ \phi_{+s}^2}{\phi_{-s}^2 + \phi_{+s}^2} - \frac{2F^4(c_+ + c_-)}{(\phi_{-s}^2 + \phi_{+s}^2)^2}, \quad (\text{H2})$$

where $\phi_{\pm s}$ are the IR components of the ϕ_{\pm} fields as given in Appendix E. We identify $m_B^2(T)$ as a low-frequency axion mass of order $O(c_-)$ that eventually tends to zero when the background fields settle to their respective minima. In this context, the effective axion mass post transition comes from physics at two different frequency/energy scales. In order to obtain an analytically solvable model, it is convenient to integrate out the high-frequency terms and obtain an effective low-frequency model in terms of the IR components. We begin by redefining ξ after the first dip as follows:

$$\xi \approx A e^{-\frac{3}{2}(T-T')} \sin \left(\int_{T'}^T \Omega_s(t) dt \right), \quad (\text{H3})$$

where $T' \approx T_c + O(1/F)$ is the approximate time when the flat deviation ξ first crosses zero after the initial $O(-F^2)$ dip. Thus, up to a quadratic expansion in ξ/Ω_s^2 , m_1^2 in Eq. (H1) has the following harmonic expansion:

$$m_1^2 \sim O(\sin(f)) + O(\sin^2(f)) \quad (\text{H4})$$

$$\sim O(\sin(f)) + O(1 - \cos(2f)), \quad (\text{H5})$$

where $f = \int_{T'}^T \Omega_s(t) dt$. Applying the adiabatic approximation method elucidated in Appendix C we integrate out the UV degree of freedom in m_1^2 to yield

$$m_1^2 \approx \left(\frac{2F^2}{\Omega_s^2} \right)^2 \frac{1}{2\Omega_s^2} A^2 e^{-3(T-T')} \\ + \frac{1}{\Omega_s^2} \left(1 - \frac{4F^4}{\Omega_s^4} \right) \frac{A^2}{2} e^{-3(T-T')} + m_B^2(T) \quad \forall \alpha \lesssim 1, \quad (\text{H6})$$

where the first term in the above expression comes from the IR reduction of the term linear in ξ in Eq. (H1), while the second term is a positive offset due to the $O(\sin^2(f))$ term from the ξ^2 quadratic term in Eq. (H1). Moreover, while the first term in Eq. (H6) results in a modification of the initial conditions at T' , the second term does not. An important consequence of the IR reduction in Eq. (H6) is that the contribution from the linear term cancels out. This cancellation of the first order UV contribution is similar to the one we observed and explained in Appendix F. Thus, the adiabatic reduction approximates the oscillating time-space potential in m_1^2 to a nonoscillating exponentially decaying positive time-space potential,

$$m_1^2 \approx e^{-3(T-T')} \beta^2 \frac{A^2}{2} + m_B^2(T) \quad \forall \alpha \lesssim 1, \quad (\text{H7})$$

where the prefactor

$$\beta^2 \approx \frac{1}{\Omega_s^2}. \quad (\text{H8})$$

Since Ω_s^2 is a time-varying function, we evaluate an average value for β^2 within a half oscillation of the background fields using $e^{-3(T-T')}$ as the weighing function.¹⁹ Using the analytic solutions for the background fields in Appendix E, we obtain the following approximate empirical fit expression for average $\langle \beta^2 \rangle$:

$$\langle \beta^2 \rangle \approx F^{-2} \left(0.139 + \frac{.14}{1.08 + \exp(11(\alpha - 0.72))} \right). \quad (\text{H9})$$

Note that the above estimation is approximate and hence one of the sources of uncertainty for all superhorizon modes at T_2 . With this approximation, the system is now analytically solvable where the reduced low-frequency mass model has a jump ETSP V_2 defined as

$$e^{-3(T-T')} \frac{V_2}{2} \equiv e^{-3(T-T')} \langle \beta^2 \rangle \frac{A^2}{2} \quad (\text{H10})$$

at $T = T' \approx T_2$. Within the framework of this adiabatic reduction, the y_1 axion mode function is expressed in terms of its slow (IR) and fast (UV) components,

$$y_1 = y_{1s} + y_{1f} \quad (\text{H11})$$

where we will neglect the y_{1f} component since $\xi/\Omega_s^2 \ll 1$ (within the scope of the adiabatic reduction). The effective mass squared ($m_1^2 - \dot{e}_1 \cdot \dot{e}_1$) for the y_{1s} -mode function is now generalized in terms of a low-frequency mass model m^2

¹⁹Note that this averaging of β^2 is different from the procedure we carried out in Appendix E since there we were concerned with a nonlinear differential equation of the background fields.

with a reduced mass eigenvalue in Eq. (H7) and the $-\dot{e}_1 \cdot \dot{e}_1$ dips (explained in Appendix F) modeled as negative square wells/dips.

The first dip at the transition T_c is obtained through a superposition of the first $\dot{e}_1 \cdot \dot{e}_1$ dip and a corresponding dip due to the evolution of the mass eigenvalue from c_+ to an oscillating function (due to a strong resonance between the ϕ_{\pm} fields). This explains the first V_1 dip of our model given in Eqs. (101) and (129). After this first negative dip of $O(F^2)$, the effective mass squared is governed by the exponentially decaying positive function $e^{-3(T-T_2)} V_2/2$ of $O(F^2/20)$. Once the V_2 mass squared function decays away, the parameter V_B of $O(c_-)$ evaluated as an average of the $m_B^2(T)$ defines the asymptotic behavior of the y_{1s} -mode amplitude. The dynamics of the m_B^2 function and its effect on the mode amplitude is covered in Appendix I.

APPENDIX I: EFFECTIVE MASS SQUARED FUNCTION m_B^2

The effective axion mass after IR averaged $m_{y_1}^2$ makes a positive jump transition at time T_2 (see Fig. 4) is derived from physics at two different frequency/energy scales. These are specified by underdamped $O(F)$ oscillation of the lightest mass eigenvalue and slowly varying part of the lightest mass squared eigenvalue function m_B^2 given by Eq. (H2). In this Appendix, we will discuss the function m_B^2 in detail and evaluate its effect on the y_1 -mode amplitude. From Eq. (H2) we note that dynamics of m_B^2 is characterized by the motion of IR components of the fields ϕ_{\pm} along the flat direction toward the minimum of the potential. Along this direction, the fields can move toward the minimum either from above ($\phi_{-s} > \phi_{-\min}$) or below ($\phi_{-s} < \phi_{-\min}$), as shown in Fig. 23. When the fields have settled to their respective minimum, m_B^2 goes to zero. Interestingly then, if the ϕ_- field settles from above the minimum then the condition $m_B^2 > 0$ is satisfied, while if it moves from below, then $m_B^2 < 0$ subject to a few conditions.

We shall now study this behavior starting from the expression for m_B^2 of Eq. (H2), which can be rearranged to get

$$m_B^2 \approx \frac{(\sqrt{c_-} \phi_{-s}^2 + \sqrt{c_+} \phi_{+s}^2)^2 - F^4 (\sqrt{c_+} + \sqrt{c_-})^2}{(\phi_{-s}^2 + \phi_{+s}^2)^2}. \quad (\text{I1})$$

Next we parametrize

$$\phi_{-s}(T) = n(T) \phi_{-\min}, \quad (\text{I2})$$

where $n(T) > 1$ for ϕ_- moving from above and $n(T) < 1$ when ϕ_- moves from below. In terms of the function $n(T)$, Eq. (I1) becomes

$$m_B^2 \propto \left(\sqrt{c_+/c_-} n^2 + n^{-2} \right)^2 - \left(\sqrt{c_+/c_-} + 1 \right)^2. \quad (\text{I3})$$

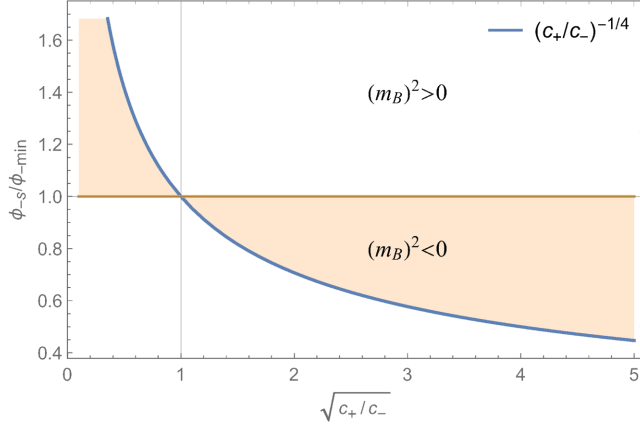


FIG. 22. Plot highlighting regions in $\{\sqrt{c_+/c_-}, \phi_{-s}/\phi_{-\min}\}$ parametric space where $m_B^2 > 0$ or $m_B^2 < 0$ corresponding to the expression in Eq. (14).

Hence, we find the following conditional expression for the m_B^2 sign for $c_+ > 9/4 \geq c_-$:

$$\text{sgn}(m_B^2) = \begin{cases} -1 & \text{if } (\frac{c_-}{c_+})^{1/4} < \frac{\phi_{-s}}{\phi_{-\min}} < 1, \\ 1 & \text{otherwise,} \end{cases} \quad (14)$$

as mapped in Fig. 22.

Therefore, dependent on the trajectory of ϕ_{-s} , a prolonged exponential decay or amplification of the super-horizon axion modes behaves as

$$y_1 \propto \exp \left[\int dT \left(\frac{-3}{2} + \frac{3}{2} \sqrt{1 - \frac{4}{9} m_B^2} \right) \right] \\ \approx \exp \left[-\frac{1}{3} \int dT m_B^2 \right], \quad (15)$$

where the integral in the exponent is cut off when m_B^2 decays faster than $1/T$. The lower limit of this integral corresponds to when the exponentially decaying term proportional to V_2 in Eq. (101) can be neglected.

In situations where $c_- \ll 9/4 < c_+$, the magnitude of the gradient of the potential is much smaller when $\phi_{-s} > \phi_{-\min}$ than when $\phi_{-s} < \phi_{-\min}$. Therefore, the fields evolve slowly [$O(1)$ timescale in T -dependent evolution] in the former scenario and fall toward the minimum rapidly in the latter (see Fig. 23). Accordingly, the axion background mass is significant in the latter case only when the fields are close to the minimum.²⁰

When the jump ETSP is significant at T_2 , it leads to an $O(0.1F)$ frequency oscillation of the IR fields (see Appendix E). These oscillations cause the fields to cross each other at least twice after the transition. To see this, first

²⁰If $c_- > 9/4$, then there is no appreciable m_B^2 since the mass squared function time dependence due to the fast rolling fields rapidly diminishes the magnitude of this function.

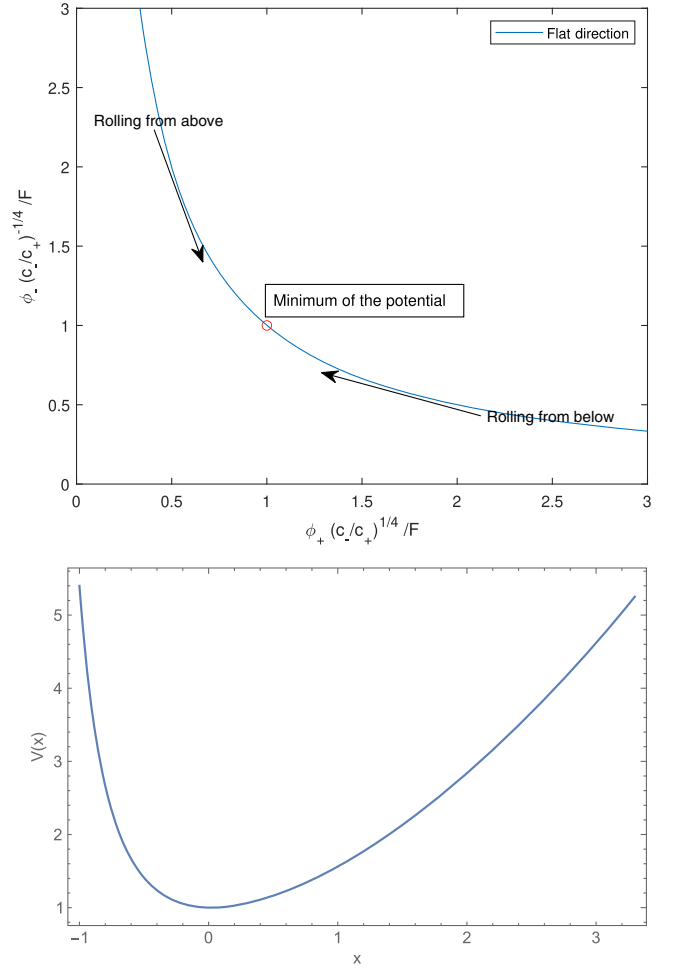


FIG. 23. In the first plot we show the two directions from which the fields can settle to the minimum of the potential while moving along the flat direction. In the second plot, the normalized potential $V(\phi_{\pm})$ is parametrized along the flat direction via parameter x for some fiducial c_{\pm} such that $c_- \ll 9/4 < c_+$. The minimum of the potential occurs at $x = 0$, where $x > 0$ corresponds to movement of the fields from above. We note that the potential has a large gradient when moving from below and falls to the minimum rapidly.

note that the resonant conditions force ϕ_{+s} to cross ϕ_{-s} (first crossing) to make $\phi_{+s} > \phi_{-s}$. Next, the asymptotic values of these fields are $\phi_{\pm\min}$, where $\phi_{-\min} > \phi_{+\min}$ for $c_+ > c_-$, and this fact requires a second crossing. These crossings give rise to second and third $\dot{e}_1 \cdot \dot{e}_1$ peaks (the first one being at T_c). Since the crossings occur at approximately F [due to the initial conditions making $\phi_{\pm s}(T_c) \sim O(F)$], we know $\phi_{-s} < \phi_{-\min} \sim (c_+/c_-)^{1/4} F > F$ at the second crossing. For $\alpha < 1$, the interaction energy now decays away due to the Hubble friction while $\phi_{-s} < \phi_{-\min}$ before ϕ_{-s} crosses $\phi_{-\min}$ again. Without the interactions mediated by the flat deviation ξ , the ϕ_{-s} settles toward the minimum from below ($\phi_{-s} < \phi_{-\min}$) and m_B^2 can become significant.

The parametric boundary of when the IR components of the ϕ_{\pm} fields cross each other at least once after T_2 is set by the following condition provided in Appendix F

$$\frac{3}{\bar{F}} \approx \frac{J_1(\sqrt{2A}/(3\bar{\Omega}))}{\sqrt{2A}/(3\bar{\Omega})}.$$

The above provides an approximate minimum value of $\sqrt{2A}/(3\bar{\Omega})$ for the background fields to cross again after T_c . Substituting for A using Eq. (173) and $\bar{\Omega}$ using Eq. (E16), we obtain a cutoff (boundary) in terms of α defined to be α_2 . Therefore, we will consider the $\alpha < \alpha_2$ and $\alpha > \alpha_2$ cases separately.

1. $\alpha < \alpha_2$

For the parametric region $\alpha < \alpha_2$, the fields will not cross again for $T > T_2$. To solve for this system, it is convenient to divide the time regions based on whether or not the $\sqrt{c_-c_+}\phi_{+s}$ term is appreciable compared to the $c_-\phi_{-s}$ term in Eq. (E9). We will call the region $[T_2, T_L]$ the period when $\sqrt{c_-c_+}\phi_{+s}$ is negligible and $T > T_L$ the period when $\sqrt{c_-c_+}\phi_{+s}$ is important.

Consider the equation of the ϕ_{-s} field in the region $[T_2, T_L]$:

$$\ddot{\phi}_{-s} + 3\dot{\phi}_{-s} + c_-\phi_{-s} + \frac{A^2}{2\bar{\Omega}^2} e^{-3(T-T_2)}\phi_{-s} \approx 0, \quad (I6)$$

where we can safely neglect the effect from the asymptotic term $\sqrt{c_-c_+}\phi_{+s}$. The solution to the above equation is given in Eq. (E10) in Appendix E, while ϕ_{+s} is given by the flat direction condition in Eq. (E15).

Due to a large positive velocity at T_2 , the ϕ_{-s} reaches a maximum and then moves slowly toward the minimum with an initial exponential decay rate equal to

$$\frac{3}{2} \left(1 - \sqrt{1 - 4c_-/9} \right) \approx \frac{c_-}{3} + \mathcal{O}(c_-^2). \quad (I7)$$

During this period when $\phi_{+s}/\phi_{-s} \ll 1$ we can expand m_B^2 using Eq. (H2):

$$m_B^2 \approx c_- - \frac{2F^4(c_+ + c_-)}{\phi_{-s}^4} + \left(c_+ - c_- + \frac{4F^4(c_+ + c_-)}{\phi_{-s}^4} \right) \left(\frac{\phi_{+s}}{\phi_{-s}} \right)^2 \quad (I8)$$

$$\approx c_- + \delta m_B^2. \quad (I9)$$

Note that as $T \rightarrow T_\infty$, the ratio ϕ_{-s}/ϕ_{+s} gradually decreases. As the two fields then approach closer to their respective minima, the interaction term $\xi\phi_{+s} \sim -\sqrt{c_+c_-}\phi_{+s}$ becomes important starting at time T_L , and the decay rate changes. Therefore, the integral corresponding to the

exponential decay of the superhorizon mode amplitude during the first temporal phase where the ϕ_{-s} field has an exponential decay factor given by Eq. (I7) is

$$\int_{\tilde{T}}^{T_L} m_B^2 dT \approx c_-(T_L - \tilde{T}) + \int_{\tilde{T}}^{T_L} \delta m_B^2 dT, \quad (I10)$$

where

$$\tilde{T} = \max\{T_2, T_V, T_K\} \quad (I11)$$

and T_K is the time when the K mode becomes superhorizon i.e., $Ka(T_K) = 3/2$. Thus, modes that exit the horizon before transition ($T_K < T_2$) have a K -independent decay factor. The time T_V is when the V_2 jump ETSP has decayed and becomes negligible compared to $m_B^2(T)$.

Next, we consider the time period $T \in [T_L, T_\infty]$, where the $\sqrt{c_+c_-}\phi_{+s}$ term is non-negligible compared to $c_-\phi_{-s}$. By comparing the two terms and using the flat direction $\phi_{+s} \approx F^2/\phi_{-s}$, we make an approximate choice of T_L as when

$$\phi_{-s}(T_L) \approx \frac{4}{3}\phi_{-\min} \quad (I12)$$

such that

$$\sqrt{c_+c_-}\phi_{+s}(T_L) \approx 0.5c_-\phi_{-s}(T_L), \quad (I13)$$

where additionally we note that at T_∞

$$\sqrt{c_+c_-}\phi_{+s}(T_\infty) = c_-\phi_{-s}(T_\infty). \quad (I14)$$

To derive the field equations, we consider the field displacements $\delta\phi_{\pm}$ as

$$\delta\phi_{\pm s} = \phi_{\pm s} - \phi_{\pm \min}, \quad (I15)$$

which implies

$$\delta\phi_{-s}(T_L) \approx \frac{\phi_{-\min}}{3}, \quad (I16)$$

in which case the terms quadratic in $\delta\phi_{\pm s}$ can be neglected compared to $\phi_{\pm \min}$ with the minima of the fields located at

$$\phi_{\pm \min} \approx \sqrt{-c_{\mp} + F^2 \sqrt{\frac{c_{\mp}}{c_{\pm}}}}. \quad (I17)$$

Expand the expressions $c_{\pm}\phi_{\pm s} + \xi\phi_{\mp s}$ in equations of motion (17) and (18) in terms of $\delta\phi_{\pm s}$ to yield

$$\begin{aligned}
c_+ \phi_{+s} + \xi \phi_{-s} &\approx (c_+ + \phi_{-\min}^2) \delta \phi_{+s} \\
&\quad + (2\phi_{+\min} \phi_{-\min} - F^2) \delta \phi_{-s}, \\
c_- \phi_{-s} + \xi \phi_{+s} &\approx (c_- + \phi_{+\min}^2) \delta \phi_{-s} \\
&\quad + (2\phi_{+\min} \phi_{-\min} - F^2) \delta \phi_{+s},
\end{aligned}$$

where all terms quadratic in $\delta \phi_{\pm s}$ within $[T_L, T_\infty]$ have been neglected. Hence, the effective mass matrix in Eqs. (17) and (18) has the following $T \rightarrow T_\infty$ asymptotic form:

$$\lim_{T \rightarrow T_\infty} \tilde{M}^2 \rightarrow \begin{bmatrix} c_+ + \phi_{-\min}^2 & 2\phi_{+\min} \phi_{-\min} - F^2 \\ 2\phi_{+\min} \phi_{-\min} - F^2 & c_- + \phi_{+\min}^2 \end{bmatrix} \quad (\text{I18})$$

with the smallest eigenvalue

$$\lambda_{\min} = \frac{4c_- c_+}{c_- + c_+} + O\left(\frac{1}{F^2}\right). \quad (\text{I19})$$

The field motion is overdamped if $\lambda_{\min} < 9/4$, which provides an upper bound on c_- ,

$$c_- < \frac{9}{16} \left(1 - \frac{9}{16c_+}\right)^{-1}. \quad (\text{I20})$$

We will assume that the c_- lies within this bound because that ensures that there will be no second crossing of ϕ_{\pm} for $T > T_L$. In terms of the smallest eigenvalue, the $\delta \phi_{\pm}$ field displacements along the approximate flat direction ($\xi \approx -\sqrt{c_- c_+}$) can be expressed in the following general asymptotic form:

$$\delta \phi_{\pm s} \approx C_{\pm} e^{-\Lambda T}, \quad (\text{I21})$$

where

$$\Lambda \approx \frac{3}{2} - \sqrt{9/4 - \lambda_{\min}} \quad (\text{I22})$$

and the constants C_+ and C_- have opposite signs such that the fields follow the flat direction. Using Eq. (E10), we can solve Eq. (I16) to obtain

$$T_L \approx T_2 - \frac{2/3}{(1-n_1)} \ln \left(\frac{2^{2-n_1} \Gamma(1-n_1) \phi_{-\min}}{3c_2} \left(\frac{A\sqrt{2}}{3\Omega} \right)^{n_1} \right) \quad (\text{I23})$$

and C_- of Eq. (I21). In the limit $c_- \ll 1$, T_L in Eq. (I23) reduces to

$$T_L \approx T_2 - \left(\frac{3}{c_-} \right) \ln \left(\frac{2 \sin(\pi n_1) 2^{2-n_1} \Gamma(1-n_1) \phi_{-\min} x^{n_1}}{\pi(3\phi_{-s}(T_2)x \partial_x J_{n_1}(x) + (3\phi_{-s}(T_2) + 2\dot{\phi}_{-s}(T_2))J_{n_1}(x))} \right)_{x=\frac{A\sqrt{2}}{3\Omega}}. \quad (\text{I24})$$

In situations where $\frac{A\sqrt{2}}{3\Omega} \ll 1$,

$$T_L \approx T_2 - \left(\frac{3}{c_-} \right) \ln \left(\frac{4\phi_{-\min} n_1}{3\phi_{-s}(T_2) + \dot{\phi}_{-s}(T_2)} \right), \quad (\text{I25})$$

and thus is independent of resonance term A . Combining with Eq. (I15), the ϕ_{-s} field solution is given as

$$\phi_{-s}(T) \approx \phi_{-\min} \left(1 + \frac{1}{3} e^{-\Lambda(T-T_L)} \right), \quad T_L \leq T < T_\infty, \quad (\text{I26})$$

which together with Eq. (E15) can be used to compute the second term of Eq. (I10):

$$\int_{\tilde{T}}^{T_L} \delta m_B^2 dT \approx -\frac{243}{1024} - \frac{73629c_-}{131072c_+} + \left(\frac{243 - 72c_+ + 81c_-/c_+ + 8c_-(2c_+ - 27)}{4/3} \right) \frac{F^4}{\dot{\phi}_{-s}^4(T_2)} e^{\frac{4c_-}{3}(\tilde{T}-T_2)} + O(c_-^2). \quad (\text{I27})$$

Next, we extend Eq. (I10) integral to T_∞ :

$$\int_{\tilde{T}}^{T_\infty} m_B^2 dT \approx c_-(T_L - \tilde{T}) + \int_{\tilde{T}}^{T_L} \delta m_B^2 dT + \int_{T_L}^{T_\infty} m_B^2 dT. \quad (\text{I28})$$

In terms of the ϕ_{-s} field equations derived above, the last term is

$$\int_{T_L}^{T_\infty} \delta m_B^2 dT \approx \frac{7}{12} + \frac{(45 - 14c_+)c_-}{54c_+} + O(c_-^2), \quad (\text{I29})$$

and substituting these, Eq. (I28) becomes

$$\int_{\tilde{T}}^{T_\infty} m_B^2 dT \approx \frac{1063}{3072} + \frac{106793c_-}{393216c_+} + c_-(T_L - \tilde{T}) + \left(\frac{243 - 72c_+ + 81c_-/c_+ + 8c_-(2c_+ - 27)}{4/3} \right) \frac{F^4}{\phi_{-s}^4(T_2)} e^{\frac{4c_-}{3}(\tilde{T} - T_2)}, \quad (\text{I30})$$

where \tilde{T} is defined in Eq. (I11). In Fig. 24, we give sample plots of $\phi_{\pm s}$ and m_B^2 for $\alpha \sim 0.51$, where the curves have been computed numerically by solving Eqs. (17) and (18).

The above expression in Eq. (I30) is utilized in Sec. VII to give an approximate decay of the superhorizon mode amplitude for cases where $\alpha < \alpha_2$. Alternatively, we define a constant mass-model parameter V_B in Eq. (101) as an average value for the time-varying m_B^2 function. Since $m_B^2 \sim O(c_-)$ is much larger during the first time period $T \in [T_2, T_L]$ than the second period $T \in [T_L, T_\infty]$ and also since $T_L - T_2 \gg T_\infty - T_L$, we can approximate the $m_B^2(T)$ function by a mode-independent constant parameter V_B during the entire time interval from $T \in [T_2, T_L]$ as follows,

$$V_B \approx \frac{1}{(T_L - T_2)} \int_{T_2}^{T_\infty} m_B^2 dT \quad (\text{I31})$$

$$\approx c_- + \frac{1}{(T_L - T_2)} \left(\frac{1063}{3072} + \frac{106793c_-}{393216c_+} \right). \quad (\text{I32})$$

Therefore, during the time interval from T_2 to T_L , the y_1 -mode equation has the following form for single dip cases:

$$y_1'' + 3y_1' + \left(K^2 e^{-2T} + V_B + \frac{V_2}{2} e^{-3(T-T_2)} \right) y_1 \approx 0, \quad (\text{I33})$$

with the general solution given in Eqs. (124) and (125) of Sec. VB.

2. $\alpha > \alpha_2$

For fields with $\alpha > \alpha_2$, the m_B^2 function during the first temporal region is $O(c_-)$ and mostly insignificant due to the oscillating IR fields. Within the second region, the IR fields are overdamped and are moving asymptotically toward their respective minima. Using the solution derived in the previous subsection, the ϕ_{-s} field can be expressed as

$$\phi_{-s}(T) \approx \phi_{-\min} \left(1 - \frac{1}{3} e^{-\Lambda(T-T_L)} \right) \quad T_L \leq T < T_\infty, \quad (\text{I34})$$

where the negative $1/3$ factor indicates that the ϕ_{-s} field is settling from below as explained previously. Hence, the m_B^2 function is positive and can lead to mode amplification. In terms of

$$n(T) = \left(1 - \frac{1}{3} e^{-\Lambda(T-T_L)} \right), \quad (\text{I35})$$

the m_B^2 function can be expressed as

$$m_B^2(T) \approx \frac{c_- c_+ (c_+ n^4 - c_-) (-1 + n^4)}{(c_+ n^4 + c_-)^2}, \quad (\text{I36})$$

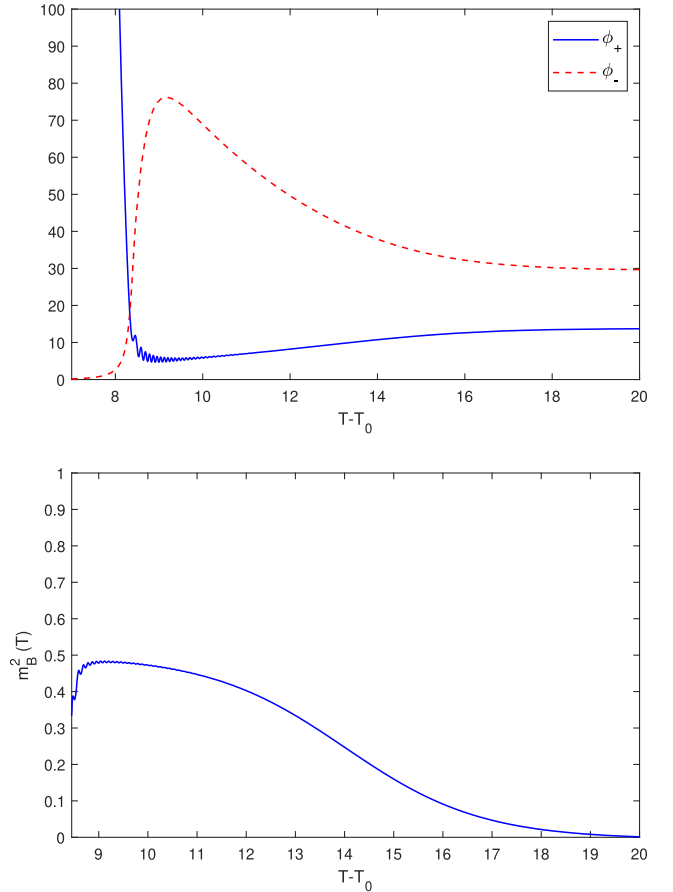


FIG. 24. Plots of $\phi_{\pm s}$ and m_B^2 for $\alpha \sim 0.51$ where the curves have been computed numerically by solving Eqs. (17) and (18). Notice the slow roll of the fields past the ϕ_{-s} maximum. This slow roll results in an effective decay of the mode amplitude through the $O(c_-)$ axion mass squared function m_B^2 , as explained in the text. In this instance, the approximate mode amplitude decay through the $\exp[-\frac{1}{3} \int m_B^2 dT]$ factor is $1/2$.

which can be used to evaluate the m_B^2 integral from T_L to T_∞ . Note that the integral is independent of the location of T_L . Similar to Eq. (I31), we average out the m_B^2 integral during the second temporal region within a time interval from $T_4 \approx T_3 + O(1/F)$ to $2/\Lambda$, where T_3 is defined within the model equation (101) and is the time when the background fields cross each other again after T_c since $\alpha > \alpha_2$. Meanwhile, $\frac{2}{\Lambda}$ is an approximate time at which the m_B^2 integral is naturally cut off where Λ is the smallest eigenvalue of the asymptotic \tilde{M}^2 effective mass squared matrix.

APPENDIX J: DECOUPLING OF HEAVY MODES

In this section, we will estimate the effect of heavy mode mixing and show that the scalar modes $y_{1,2}$ are effectively decoupled at transition within the parametric region $\alpha \lesssim 1$ such that the heavier mode y_2 can be completely neglected within a 20% error margin. We begin with the $y_{1,2}$ mode mixing equations from Eqs. (36) and (37) with the mode-mixing term S_{ns} in the rhs defined in Eq. (39),

$$\ddot{y}_1 + \gamma_1^2 y_1 = S_{12} y_2, \quad (\text{J1})$$

$$\ddot{y}_2 + \gamma_2^2 y_2 = S_{21} y_1, \quad (\text{J2})$$

with

$$S_{ns}(T) = -e_n \cdot \ddot{e}_s - 2e_n \cdot \dot{e}_s \partial_T \quad (\text{J3})$$

and

$$\gamma_i^2 = m_i^2 - \dot{e}_i \cdot \dot{e}_i + k^2/a^2, \quad (\text{J4})$$

where we define γ_n^2 as the effective frequency squared. Note the Hubble friction term has been removed by rescaling the mode functions.

Let us assume that the eigenvector gradient term $\dot{e}_1 \cdot \dot{e}_1$ peaks at a time T_* when the background fields tend to cross each other such that the kinetic energy corresponding to the relative velocity of the two fields is maximized and the eigenvector gradient $\dot{e}_{1,2}$ is larger than $O(F)$. Thus, the mode-mixing operator S_{ns} is significant in a small neighborhood $O(1/F)$ around T_* . We begin with the normalized eigenstates and rewrite the gradient terms in S_{ns} through an approximate Lorentzian function $L_{ns}(T - T_*)$ with a peak at T_* such that

$$e_n \cdot \partial_T e_s \approx L_{ns}(T - T_*), \quad (\text{J5})$$

$$e_n \cdot \partial_T^2 e_s \approx \partial_T L_{ns}(T - T_*). \quad (\text{J6})$$

Note that the $e_n \cdot \dot{e}_s$ term is symmetric around T_* , while $e_n \cdot \ddot{e}_s$ is antisymmetric. The second term $-3\dot{e}_s \cdot e_n$ in S_{ns} is due to Hubble friction and can be removed by scaling the mode functions without affecting our discussion.

During the early phase when $|\phi_+| \gg |\phi_-|$, the heavier mode y_2 is forced driven by the lighter mode y_1 . This is similar to the perturbed solution for the ϕ_\pm background fields where the ϕ_- field is effectively forced driven by ϕ_+ . Accordingly, the y_2 mode has the following solution:

$$y_2 \approx \frac{S_{21} y_1}{\gamma_2^2}, \quad (\text{J7})$$

where $y_{1,2}$ satisfies the condition

$$\left| \frac{y_2}{y_1} \right| \ll 1. \quad (\text{J8})$$

Meanwhile, the right-hand side term $S_{12} y_2$ in the y_1 -mode equation is negligible and thus

$$\mathcal{O}_1 y_1 \approx 0. \quad (\text{J9})$$

Therefore, the lighter mode is decoupled from the heavier during the early phase since $\gamma_2^2 \sim O(\phi_+^2) \gg O(F^2)$.

Later at $T \approx T_*$ the eigenvector gradient terms in S_{ns} become significant $O(F^2)$. At the same time, the effective frequency squared $\gamma_{1,2}^2$ approach a local minima at $T \approx T_*$. Consequently, the y_2 amplitude reaches a local maximum close to T_* such that the heavy mode-mixing effect due to the term $S_{12} y_2$ on the rhs of Eq. (36) cannot be neglected. Post T_* , the heavier mode y_2 behaves like an underdamped harmonic oscillator and undergoes rapid oscillations with a large frequency $\sqrt{\gamma_2^2}$ due to the heavier mass eigenvalue.

To evaluate the heavy mode-mixing effect, we will approximate the function $L_{ns}(T - T_*)$ as a rectangular ETSP²¹ of amplitude E and width $\Delta T \approx 1/E$, where $E \sim O(F)$:

$$|e_n \cdot \partial_T e_s| \approx \begin{cases} E & T_1 < T < T_2, \\ 0 & \text{otherwise.} \end{cases} \quad (\text{J10})$$

Using this approximation, the $e_n \cdot \dot{e}_s$ term peaks at the boundaries $T_{1,2}$ and remains 0 within the interval $[T_1, T_2]$.

1. y_1 solution

The general solution for the lighter mode y_1 from Eq. (J1) can be expressed as

$$y_1 = \left(c_1 - \int f_2 \frac{S_{12} y_2}{W} dT \right) f_1(T) + \left(c_2 + \int f_1 \frac{S_{12} y_2}{W} dT \right) f_2(T), \quad (\text{J11})$$

²¹The following assumption can be verified using the analytical form of the background fields from Sec. IV B.

where $f_{1,2}(T)$ are the linearly independent functions that solve the homogeneous equation $\ddot{y}_1 + \gamma_1^2 y_1 = 0$. The coefficients $c_{1,2}$ are obtained from the initial conditions at $T = T_1$ and the integral terms correspond to the inhomogeneous part on the rhs of Eq. (J1). W is the associated Wronskian of $f_{1,2}$. Within the interval $[T_1, T_2]$, $0 < \dot{e}_1 \cdot \dot{e}_1 \sim O(F^2)$, while $m_1^2 < 0$ due to the deviation of the background fields away from the flat direction. Therefore, the effective lighter frequency squared $\gamma_1^2 = m_1^2 - \dot{e}_1 \cdot \dot{e}_1 + k^2/a(T_*)^2 < 0$ for $k^2/a(T_*)^2 \ll m_1^2 - \dot{e}_1 \cdot \dot{e}_1$. Therefore, the lighter mode y_1 has the homogeneous solution

$$y_1^h(T) \approx y_1(T_1) \cosh \left[\sqrt{9/4 - \gamma_1^2} (T - T_1) \right], \quad (\text{J12})$$

where

$$f_1(T) = e^{\sqrt{-\gamma_1^2} T}, \quad f_2(T) = e^{-\sqrt{-\gamma_1^2} T}, \quad (\text{J13})$$

and $\partial_T y_1(T_1)/y_1(T_1) \ll \sqrt{9/4 - \gamma_1^2} \sim O(F)$ so that $c_{1,2} \approx y_1(T_1)/2$. Note that a positive value of the $\int dT f_2 S_{12} y_2/W$ integral accounts for a decrease in the power of the lighter mode [dominated by the f_1 mode if $k^2/a(T_*)^2 \ll m_1^2 - \dot{e}_1 \cdot \dot{e}_1$ such that $\gamma_1^2 < 0$] due to the heavy mode coupling. As we will show later, the integral term is indeed positive such that a finite fraction of the power is removed by the heavier mode.

2. y_2 solution

To solve for the heavier mode y_2 within the interval $[T_1, T_2]$, we rewrite Eq. (J2) as

$$\ddot{y}_2 + \gamma_2^2 y_2 = -2L_{21}(T_*) \partial_T y_1. \quad (\text{J14})$$

Assuming decoupling of the modes²², we will substitute y_1 with y_1^h . The y_2 is then given by

$$y_2 \approx \frac{-2L_{21}(T_*)y_1(T_1)}{\gamma_2^2 + (9/4 - \gamma_1^2)} \sqrt{9/4 - \gamma_1^2} \sinh \left[\sqrt{9/4 - \gamma_1^2} (T - T_1) \right] + \frac{-\partial_T L_{21}(T_1)y_1(T_1)}{\gamma_2^2(T_1)} \cos [\gamma_2(T - T_1)], \quad (\text{J15})$$

where the first term is via the forced component on the rhs, while the second term is the homogeneous component that oscillates with frequency γ_2 with initial conditions set at T_1 . Using the above solution for y_2 , the rhs term $S_{12}y_2 = -2L_{12}(T_*)\partial_T y_2$ is evaluated as

$$S_{12}y_2 \approx -2 \left(\frac{-2L_{12}(T_*)L_{21}(T_*)y_1(T_1)}{\gamma_2^2 - \gamma_1^2} (-\gamma_1^2) \cosh \left[\sqrt{-\gamma_1^2} (T - T_1) \right] - \frac{-L_{12}(T_*)\partial_T L_{21}(T_1)y_1(T_1)}{\gamma_2(T_1)} \sin [\gamma_2(T - T_1)] \right). \quad (\text{J16})$$

Using the equations for the background fields in Sec. IV B, $L_{12}(T_*)L_{21}(T_*) \approx -E^2$ and $L_{12}(T_*)\partial_T L_{21} \approx -nE^3$ for $n \approx 4/3$. Hence we have

$$S_{12}y_2 \approx 4y_1(T_1)E^2 \left(\frac{\gamma_1^2}{\gamma_2^2 - \gamma_1^2} \cosh \left[\sqrt{-\gamma_1^2} (T - T_1) \right] + \frac{nE/2}{\gamma_2(T_1)} \sin [\gamma_2(T - T_1)] \right). \quad (\text{J17})$$

3. Heavy mixing coefficient χ_{HM}

We are now in a position to complete the y_1 solution in Eq. (J11) by solving the integral terms. Since the homogeneous function f_1 dominates over f_2 we will only solve $\int dT f_2 S_{12} y_2/W$ within the interval $[T_1, T_2]$ when the S_{ns} operator is significant. Using the Wronskian $W = -2\sqrt{-\gamma_1^2}$,

$$\int f_2 \frac{S_{12}y_2}{W} dT = 4y_1(T_1) \frac{\gamma_1^2 E^2}{\gamma_2^2 - \gamma_1^2} \int_{T_1}^{T_2} e^{-\sqrt{-\gamma_1^2} T} \frac{\cosh [\sqrt{-\gamma_1^2} (T - T_1)]}{-2\sqrt{-\gamma_1^2}} dT + 4y_1(T_1) \frac{nE^3/2}{\gamma_2(T_1)} \int_{T_1}^{T_2} \frac{e^{-\sqrt{-\gamma_1^2} T}}{-2\sqrt{-\gamma_1^2}} \sin [\gamma_2(T - T_1)] dT \quad (\text{J18})$$

$$\approx 4y_1(T_1) \frac{\gamma_1^2 E^2}{\gamma_2^2 - \gamma_1^2} \left(\frac{1 + 2\sqrt{-\gamma_1^2} \Delta T - e^{-2\sqrt{-\gamma_1^2} \Delta T}}{-8(-\gamma_1^2)} \right) + 4y_1(T_1) \frac{nE^3/2}{\gamma_2(T_1)} \left(\frac{-\gamma_2 + e^{-\sqrt{-\gamma_1^2} \Delta T} (\sqrt{-\gamma_1^2} \sin [\gamma_2 \Delta T] + \gamma_2 \cos [\gamma_2 \Delta T])}{2\sqrt{-\gamma_1^2} (\gamma_2^2 - \gamma_1^2)} \right). \quad (\text{J19})$$

²²Although this is a cyclic argument, we prove this by self-consistency at the end.

The above can be further simplified as

$$\int f_2 \frac{S_{12}y_2}{W} dT \approx 4y_1(T_1) \frac{E^2}{\gamma_2^2 - \gamma_1^2} \left[\frac{1 + 2\sqrt{-\gamma_1^2 \Delta T}}{8} + \frac{nE/4}{\sqrt{-\gamma_1^2}} (-1 + e^{-\sqrt{-\gamma_1^2 \Delta T}} \cos[\gamma_2 \Delta T]) \right]. \quad (\text{J20})$$

We now define the heavy mixing coefficient χ_{HM} as

$$\chi_{\text{HM}} = \frac{\int f_2 \frac{S_{12}y_2}{W} dT}{c_1}. \quad (\text{J21})$$

Using $c_1 \approx y_1(T_1)/2$ and $E\Delta T \approx 1$, we obtain

$$\chi_{\text{HM}}(l_1^2, l_2^2)|_{T=T_*} \approx \frac{1}{l_2^2 - l_1^2} \left(1 + 2\sqrt{-l_1^2} + \frac{2n}{\sqrt{-l_1^2}} (-1 + e^{-\sqrt{-l_1^2}} \cos[l_2]) \right), \quad (\text{J22})$$

where $l_i^2 = \gamma_i^2/E^2$ for $E^2 = \max(\dot{e}_1^2)$ and we approximate $n \approx 4/3$. Since m_i^2 and E^2 are $O(F^2)$, the parameters l_i^2 are almost F independent for $F \gg 1$.

From Eq. (J11), we infer that the two modes shall remain decoupled as long as $\max(\chi_{\text{HM}}) \ll 1$, where we define $\max(\chi_{\text{HM}})$ as a local maxima in the vicinity of T_* within a neighborhood of $O(1/F)$. Note that a positive value of χ_{HM} accounts for a decrease in the power of the lighter mode due to the heavy mode coupling. The mixing between the two modes thus results in a significant proportion of power transfer from the lighter mode to the heavier and as a result the isocurvature power spectrum reduces. Figure 25 gives an analytical plot of χ_{HM} evaluated at $T_* \approx T_c$ in the limit $k^2/a(T_*)^2 \rightarrow 0$ using Eq. (J22) plotted with respect to the

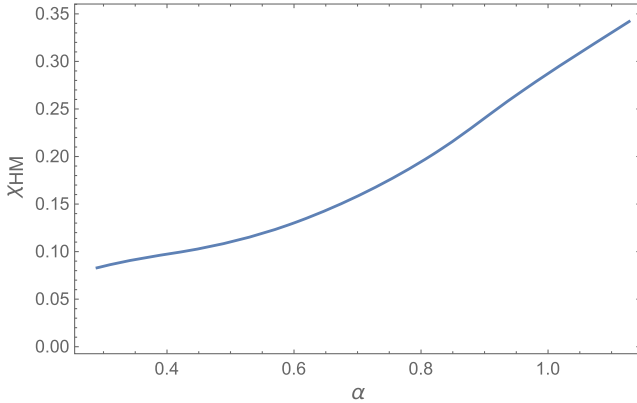


FIG. 25. Analytical plot of the fractional reduction in the amplitude of the lighter mode y_1 due to heavy mode mixing evaluated at $T_* \approx T_c$ using Eq. (J22) in the limit $k^2/a(T_*)^2 \rightarrow 0$ plotted with respect to the parameter α defined in Eq. (74). Numerical results suggest that the estimation given in Eq. (J22) is an approximate upper bound, as explained in the text.

parameter α defined in Eq. (74). By considering a reasonable decoupling between the two modes for $\chi_{\text{HM}} \lesssim 0.2$, we obtain an upper bound of $\alpha_U \sim 1$ for fields crossing each other close to T_* . If we consider $F \gg 1$ cases, then the upper bound α_U is almost F independent. For $\alpha > \alpha_2$, every subsequent crossing of the two background fields post transition will give rise to similar $\dot{e}_1 \cdot \dot{e}_1$ peaks. The effective heavy mixing is then a sum of the contributions from each of these peaks. Since the peaks are exponentially suppressed by Hubble friction, their contribution is significantly low. However, for large F , the subsequent peaks can get closer to each other and hence the net heavy mixing contribution can become significant.

From Eq. (J22), we infer that as k increases from zero, l_1^2 begins to reduce in magnitude such that χ_{HM} initially reduces until $k/a(T_*) \sim \sqrt{-m_1^2}$. Thereafter, χ_{HM} turns imaginary and begins to increase in magnitude. The above analytical estimate is primarily valid as long as χ_{HM} remains much less than unity since in order to estimate χ_{HM} we have approximated $S_{21}y_1$ as $S_{21}y_1^h$ by substituting with the homogeneous y_1^h solution. As $|y_1| \leq |y_1^h|$, one expects that the χ_{HM} evaluated using the exact y_1 solution should be lower than the above estimate as long as Eq. (J22) is valid. If k eventually becomes large enough that the $k^2/a(T_*)^2$ term dominates over the remaining mass squared terms, we obtain $\gamma_1^2 = \gamma_2^2$ at T_* and the modes are strongly coupled such that $|y_2| \rightarrow |y_1|$. Similar strong coupling is possible if $E \gg m_2^2 \sim F^2 \sqrt{c_+/c_-}$. However, in such cases, the corresponding value of $\Delta T \ll 1/F$. Since the coupled system of $y_{1,2}$ has only one dominant time scale of $O(1/F)$, the two modes momentarily tend to $|y_2| \sim |y_1|$ at T_* before y_1 returns back to the attractor solution y_1^h . Hence, whenever $E \gg m_2^2$, the coupling between the two modes can be neglected.

- [1] J. E. Kim and G. Carosi, Axions and the strong CP problem, *Rev. Mod. Phys.* **82**, 557 (2010).
- [2] L. Di Luzio, M. Giannotti, E. Nardi, and L. Visinelli, The landscape of QCD axion models, *Phys. Rep.* **870**, 1 (2020).
- [3] R. D. Peccei, Why PQ?, *AIP Conf. Proc.* **1274**, 7 (2010).
- [4] R. D. Peccei, The strong CP problem and axions, *Lect. Notes Phys.* **741**, 3 (2008).
- [5] P. Agrawal, J. Fan, M. Reece, and L.-T. Wang, Experimental targets for photon couplings of the QCD axion, *J. High Energy Phys.* **02** (2018) 006.
- [6] M. Kawasaki and K. Nakayama, Axions: Theory and cosmological role, *Annu. Rev. Nucl. Part. Sci.* **63**, 69 (2013).
- [7] E. W. Kolb and M. S. Turner, The early Universe, *Front. Phys.* **69**, 1 (1990).
- [8] D. J. E. Marsh, Axion cosmology, *Phys. Rep.* **643**, 1 (2016).
- [9] P. Sikivie, Axion cosmology, *Lect. Notes Phys.* **741**, 19 (2008).
- [10] J. Preskill, M. B. Wise, and F. Wilczek, Cosmology of the invisible axion, *Phys. Lett.* **120B**, 127 (1983).
- [11] L. F. Abbott and P. Sikivie, A cosmological bound on the invisible axion, *Phys. Lett.* **120B**, 133 (1983).
- [12] M. Dine and W. Fischler, The not so harmless axion, *Phys. Lett.* **120B**, 137 (1983).
- [13] Z. G. Berezhiani, A. S. Sakharov, and M. Y. Khlopov, Primordial background of cosmological axions, *Sov. J. Nucl. Phys.* **55**, 1063 (1992).
- [14] A. S. Sakharov and M. Y. Khlopov, The nonhomogeneity problem for the primordial axion field, *Phys. At. Nucl.* **57**, 485 (1994).
- [15] M. Y. Khlopov, A. S. Sakharov, and D. D. Sokoloff, The nonlinear modulation of the density distribution in standard axionic CDM and its cosmological impact, *Nucl. Phys. B, Proc. Suppl.* **72**, 105 (1999).
- [16] R. Bahre, B. Dobrich, J. Dreyling-Eschweiler, S. Ghazaryan, R. Hodajerdi, D. Horns *et al.*, Any light particle search II—Technical design report, *J. Instrum.* **8**, T09001 (2013).
- [17] CAST Collaboration, New cast limit on the axion-photon interaction, *Nat. Phys.* **13**, 584 (2017).
- [18] J. L. Ouellet, C. P. Salemi, J. W. Foster, R. Henning, Z. Bogorad, J. M. Conrad *et al.*, First Results from ABRA-CADABRA-10 cm: A Search for Sub- μeV Axion Dark Matter, *Phys. Rev. Lett.* **122**, 121802 (2019).
- [19] T. Braine, R. Cervantes, N. Crisosto, N. Du, S. Kimes, L. Rosenberg *et al.* (ADMX Collaboration), Extended Search for the Invisible Axion with the Axion Dark Matter Experiment, *Phys. Rev. Lett.* **124**, 101303 (2020).
- [20] A. V. Gramolin, D. Aybas, D. Johnson, J. Adam, and A. O. Sushkov, Search for axion-like dark matter with ferromagnets, *Nat. Phys.* **17**, 79 (2021).
- [21] O. Kwon, D. Lee, W. Chung, D. Ahn, H. Byun, F. Caspers *et al.*, First Results from an Axion Haloscope at CAPP around $10.7 \mu\text{eV}$, *Phys. Rev. Lett.* **126**, 191802 (2021).
- [22] B. Brubaker, L. Zhong, Y. Gurevich, S. Cahn, S. Lamoreaux, M. Simanovskaia *et al.*, First Results from a Microwave Cavity Axion Search at $24 \mu\text{eV}$, *Phys. Rev. Lett.* **118**, 061302 (2017).
- [23] B. T. McAllister, G. Flower, J. Kruger, E. N. Ivanov, M. Goryachev, J. Bourhill, and M. E. Tobar, The ORGAN experiment: An axion haloscope above 15 GHz, *Phys. Dark Universe* **18**, 67 (2017).
- [24] D. Alesini, D. Babusci, D. D. Gioacchino, C. Gatti, G. Lamanna, and C. Ligi, The Klash Proposal, 2017, [arXiv:1707.06010](https://arxiv.org/abs/1707.06010).
- [25] D. Alesini, C. Braggio, G. Carugno, N. Crescini, D. D'Agostino, D. Di Gioacchino *et al.*, Search for invisible axion dark matter of mass $m_a = 43 \mu\text{eV}$ with the QUAX- $\alpha\gamma$ experiment, *Phys. Rev. D* **103**, 102004 (2021).
- [26] A. A. Geraci, H. Fosbinder-Elkins, C. Lohmeyer, J. Dargert and M. Cunningham *et al.*, Progress on the ARIADNE axion experiment, in *Microwave Cavities and Detectors for Axion Research*, edited by G. Carosi, G. Rybka, and K. van Bibber, Springer Proceedings in Physics, Vol. 211 (Springer, Cham, Switzerland, 2017), pp. 151–161, [arXiv:1710.05413](https://arxiv.org/abs/1710.05413).
- [27] D. Budker, P. W. Graham, M. Ledbetter, S. Rajendran, and A. O. Sushkov, Proposal for a Cosmic Axion Spin Precession Experiment (CASPER), *Phys. Rev. X* **4**, 021030 (2014).
- [28] P. Brun, A. Caldwell, L. Chevalier, G. Dvali, P. Freire, E. Garutti *et al.* (MADMAX Collaboration), A new experimental approach to probe QCD axion dark matter in the mass range above $40 \mu\text{eV}$, *Eur. Phys. J. C* **79**, 186 (2019).
- [29] E. Armengaud, F. T. Avignone, M. Betz, P. Brax, P. Brun, G. Cantatore *et al.*, Conceptual design of the International Axion Observatory (IAXO), *J. Instrum.* **9**, T05002 (2014).
- [30] E. Armengaud, D. Attié, S. Basso, P. Brun, N. Bykovskiy, J. Carmona *et al.*, Physics potential of the International Axion Observatory (IAXO), *J. Cosmol. Astropart. Phys.* **06** (2019) 047.
- [31] A. Ringwald, Exploring the role of axions and other WISPs in the dark Universe, *Phys. Dark Universe* **1**, 116 (2012).
- [32] J. Redondo and A. Ringwald, Light shining through walls, *Contemp. Phys.* **52**, 211 (2011).
- [33] A. Ringwald, Searching for axions and ALPs from string theory, *J. Phys. Conf. Ser.* **485**, 012013 (2014).
- [34] Y. V. Stadnik and V. V. Flambaum, New generation low-energy probes for ultralight axion and scalar dark matter, *Mod. Phys. Lett. A* **32**, 1740004 (2017).
- [35] G. Carosi, A. Friedland, M. Giannotti, M. J. Pivovarov, J. Ruz, and J. K. Vogel, Probing the axion-photon coupling: Phenomenological and experimental perspectives, A Snowmass white paper, 2013, [arXiv:1309.7035](https://arxiv.org/abs/1309.7035).
- [36] P. W. Graham and S. Rajendran, New observables for direct detection of axion dark matter, *Phys. Rev. D* **88**, 035023 (2013).
- [37] P. Agrawal, M. Bauer, J. Beacham, A. Berlin, A. Boyarsky, S. Cebrian *et al.*, Feebly-interacting particles: FIPs 2020 workshop report, *Eur. Phys. J. C* **81**, 1015 (2021).
- [38] I. G. Irastorza and J. Redondo, New experimental approaches in the search for axion-like particles, *Prog. Part. Nucl. Phys.* **102**, 89 (2018).
- [39] S. Kasuya and M. Kawasaki, Axion isocurvature fluctuations with extremely blue spectrum, *Phys. Rev. D* **80**, 2 (2009).
- [40] S. Kasuya, M. Kawasaki, and T. Yanagida, Domain wall problem of axion and isocurvature fluctuations in chaotic inflation models, *Phys. Lett. B* **415**, 117 (1997).
- [41] M. Kawasaki, N. Sugiyama, and T. Yanagida, Isocurvature and adiabatic fluctuations of axion in chaotic inflation

- models and large scale structure, *Phys. Rev. D* **54**, 2442 (1996).
- [42] K. Nakayama and M. Takimoto, Higgs inflation and suppression of axion isocurvature perturbation, *Phys. Lett. B* **748**, 108 (2015).
- [43] K. Harigaya, M. Ibe, M. Kawasaki, and T. T. Yanagida, Dynamics of Peccei-Quinn breaking field after inflation and axion isocurvature perturbations, *J. Cosmol. Astropart. Phys.* **11** (2015) 003.
- [44] K. Kadota, J.-O. Gong, K. Ichiki, and T. Matsubara, CMB probes on the correlated axion isocurvature perturbation, *J. Cosmol. Astropart. Phys.* **03** (2015) 026.
- [45] N. Kitajima and F. Takahashi, Resonant conversions of QCD axions into hidden axions and suppressed isocurvature perturbations, *J. Cosmol. Astropart. Phys.* **01** (2015) 032.
- [46] M. Kawasaki, N. Kitajima, and F. Takahashi, Relaxing isocurvature bounds on string axion dark matter, *Phys. Lett. B* **737**, 178 (2014).
- [47] T. Higaki, K. S. Jeong, and F. Takahashi, Solving the tension between high-scale inflation and axion isocurvature perturbations, *Phys. Lett. B* **734**, 21 (2014).
- [48] K. S. Jeong and F. Takahashi, Suppressing isocurvature perturbations of QCD axion dark matter, *Phys. Lett. B* **727**, 448 (2013).
- [49] T. Kobayashi, R. Kurematsu, and F. Takahashi, Isocurvature constraints and anharmonic effects on QCD axion dark matter, *J. Cosmol. Astropart. Phys.* **09** (2013) 032.
- [50] J. Hamann, S. Hannestad, G. G. Raffelt, and Y. Y. Y. Wong, Isocurvature forecast in the anthropic axion window, *J. Cosmol. Astropart. Phys.* **06** (2009) 022.
- [51] M. P. Hertzberg, M. Tegmark, and F. Wilczek, Axion cosmology and the energy scale of inflation, *Phys. Rev. D* **78**, 083507 (2008).
- [52] M. Beltran, J. Garcia-Bellido, and J. Lesgourgues, Isocurvature bounds on axions revisited, *Phys. Rev. D* **75**, 103507 (2007).
- [53] P. Fox, A. Pierce, and S. Thomas, Probing a QCD string axion with precision cosmological measurements, [arXiv: hep-th/0409059](https://arxiv.org/abs/hep-th/0409059).
- [54] M. Estevez and O. Santillán, About the isocurvature tension between axion and high scale inflationary models, *Eur. Phys. J. C* **76**, 398 (2016).
- [55] J. Kearney, N. Orlofsky, and A. Pierce, High-scale axions without isocurvature from inflationary dynamics, *Phys. Rev. D* **93**, 095026 (2016).
- [56] Y. Nomura, S. Rajendran, and F. Sanches, Axion Isocurvature and Magnetic Monopoles, *Phys. Rev. Lett.* **116**, 141803 (2016).
- [57] K. Kadota, T. Kobayashi, and H. Otsuka, Axion inflation with cross-correlated axion isocurvature perturbations, *J. Cosmol. Astropart. Phys.* **01** (2016) 044.
- [58] C. Hikage, M. Kawasaki, T. Sekiguchi, and T. Takahashi, CMB constraint on non-Gaussianity in isocurvature perturbations, *J. Cosmol. Astropart. Phys.* **07** (2013) 007.
- [59] D. Langlois, Isocurvature cosmological perturbations and the CMB, *C.R. Phys.* **4**, 953 (2003).
- [60] S. Mollerach, On the primordial origin of isocurvature perturbations, *Phys. Lett. B* **242**, 158 (1990).
- [61] M. Axenides, R. Brandenberger, and M. Turner, Development of axion perturbations in an axion dominated Universe, *Phys. Lett.* **126B**, 178 (1983).
- [62] B. Jo, H. Kim, H. D. Kim, and C. S. Shin, Exploring the Universe with dark light scalars, *Phys. Rev. D* **103**, 083528 (2021).
- [63] S. Iso, K. Kawana, and K. Shimada, Axion-CMB scenario in a supercooled universe, *Phys. Rev. D* **104**, 063525 (2021).
- [64] K. J. Bae, J. Kost, and C. S. Shin, Deformation of axion potentials: Implications for spontaneous baryogenesis, dark matter, and isocurvature perturbations, *Phys. Rev. D* **99**, 043502 (2019).
- [65] L. Visinelli, Light axion-like dark matter must be present during inflation, *Phys. Rev. D* **96**, 023013 (2017).
- [66] Y. Takeuchi and S. Chongchitnan, Constraining isocurvature perturbations with the 21 cm emission from minihaloes, *Mon. Not. R. Astron. Soc.* **439**, 1125 (2014).
- [67] M. Bucher, K. Moodley, and N. Turok, Constraining Isocurvature Perturbations with CMB Polarization, *Phys. Rev. Lett.* **87**, 191301 (2001).
- [68] D. Grin, O. Dore, and M. Kamionkowski, Compensated isocurvature perturbations and the cosmic microwave background, *Phys. Rev. D* **84**, 123003 (2011).
- [69] J. B. Munoz, D. Grin, L. Dai, M. Kamionkowski, and E. D. Kovetz, Search for compensated isocurvature perturbations with Planck power spectra, *Phys. Rev. D* **93**, 043008 (2016).
- [70] C. Gordon and J. R. Pritchard, Forecasted 21 cm constraints on compensated isocurvature perturbations, *Phys. Rev. D* **80**, 063535 (2009).
- [71] C. He, D. Grin, and W. Hu, Compensated isocurvature perturbations in the curvaton model, *Phys. Rev. D* **92**, 063018 (2015).
- [72] E. Dimastrogiovanni, M. Fasiello, and M. Kamionkowski, Imprints of massive primordial fields on large-scale structure, *J. Cosmol. Astropart. Phys.* **02** (2016) 017.
- [73] A. Linde and V. Mukhanov, Non-Gaussian isocurvature perturbations from inflation, *Phys. Rev. D* **56**, R535 (1997).
- [74] D. J. H. Chung, Large blue isocurvature spectral index signals time-dependent mass, *Phys. Rev. D* **94**, 043524 (2016).
- [75] D. J. H. Chung and A. Upadhye, Bump in the blue axion isocurvature spectrum, *Phys. Rev. D* **95**, 023503 (2017).
- [76] Y. Akrami *et al.* (Planck Collaboration), Planck 2018 results. X. Constraints on inflation, *Astron. Astrophys.* **641**, A10 (2020).
- [77] D. J. H. Chung and A. Upadhye, Search for strongly blue axion isocurvature, *Phys. Rev. D* **98**, 023525 (2018).
- [78] V. Novicenko, J. Ruseckas, and E. Anisimovas, Quantum dynamics in potentials with fast spatial oscillations, *Phys. Rev. A* **99**, 043608 (2019).
- [79] D. J. H. Chung and H. Yoo, Elementary theorems regarding blue isocurvature perturbations, *Phys. Rev. D* **91**, 083530 (2015).
- [80] D. J. H. Chung and S. Tadepalli, Underdamped axionic blue isocurvature perturbation parameterizations.
- [81] K. Inomata, M. Kawasaki, K. Mukaida, T. T. Yanagida, and T. D. Lee, NANOGrav Results and LIGO-Virgo Primordial Black Holes in Axionlike Curvaton Models, *Phys. Rev. Lett.* **126**, 131301 (2021).

- [82] K. Ando, K. Inomata, M. Kawasaki, K. Mukaida, and T. T. Yanagida, Primordial black holes for the LIGO events in the axionlike curvaton model, *Phys. Rev. D* **97**, 123512 (2018).
- [83] M. Kawasaki, N. Kitajima, and T. T. Yanagida, Primordial black hole formation from an axionlike curvaton model, *Phys. Rev. D* **87**, 063519 (2013).
- [84] E. Bugaev and P. Klimai, Cosmological constraints on the curvaton web parameters, *Phys. Rev. D* **88**, 023521 (2013).
- [85] E. V. Bugaev and P. A. Klimai, Primordial black hole constraints for curvaton models with predicted large non-Gaussianity, *Int. J. Mod. Phys. D* **22**, 1350034 (2013).
- [86] S. Young and C. T. Byrnes, Primordial black holes in non-Gaussian regimes, *J. Cosmol. Astropart. Phys.* **08** (2013) 052.
- [87] K. Ando, M. Kawasaki, and H. Nakatsuka, Formation of primordial black holes in an axionlike curvaton model, *Phys. Rev. D* **98**, 083508 (2018).
- [88] C. Chen and Y.-F. Cai, Primordial black holes from sound speed resonance in the inflaton-curvaton mixed scenario, *J. Cosmol. Astropart. Phys.* **10** (2019) 068.
- [89] S. Passaglia and M. Sasaki, Primordial black holes from CDM isocurvature, *Phys. Rev. D* **105**, 103530 (2022).
- [90] M. Kawasaki and H. Nakatsuka, Gravitational waves from type II axion-like curvaton model and its implication for NANOGrav result, *J. Cosmol. Astropart. Phys.* **05** (2021) 023.
- [91] M. Kawasaki, K. Nakayama, T. Sekiguchi, T. Suyama, and F. Takahashi, A general analysis of non-Gaussianity from isocurvature perturbations, *J. Cosmol. Astropart. Phys.* **01** (2009) 042.
- [92] K. Inomata and T. Nakama, Gravitational waves induced by scalar perturbations as probes of the small-scale primordial spectrum, *Phys. Rev. D* **99**, 043511 (2019).
- [93] D. Langlois and A. Lepidi, General treatment of isocurvature perturbations and non-Gaussianities, *J. Cosmol. Astropart. Phys.* **01** (2011) 008.
- [94] M. Beltran, Isocurvature, non-Gaussianity, and the curvaton model, *Phys. Rev. D* **78**, 023530 (2008).